

DISS. ETH NO. 27508

# **Nanoscale Scanning Diamond Magnetometry of Antiferromagnets**

A thesis submitted to attain the degree of  
DOCTOR OF SCIENCE of ETH ZURICH  
(Dr. sc. ETH Zurich)

presented by

**Martin Sebastian Wörnle**

M.Sc. in Physics, Universität Regensburg

born on 10.03.1991

citizen of Germany

accepted on the recommendation of  
Prof. Dr. Pietro Gambardella, examiner  
Prof. Dr. Christian L. Degen, examiner  
Prof. Dr. Nicola Spaldin, co-examiner  
Dr. Denys Makarov, co-examiner

2021



*"Interesting but useless?!"*

Louis Néel





# *Abstract*

Antiferromagnetic materials are receiving widespread attention because they promise to enable smaller, faster, and more resilient data processing units compared to state-of-the-art ferromagnets. The possibility to control the orientation of the magnetic domains in antiferromagnets by either electrical or optical means is revolutionizing the field of magnetism and opening a wealth of applications in spintronics. Outstanding open questions bear on both fundamental problems (switching mechanism) as well as on applied aspects (amplitude of the readout signal). One of the great unknowns in the field of antiferromagnetism is the structure of domain walls, which is key to both of these aspects. In particular, chiral walls are required for current-controlled magnetisation switching. The limited knowledge about antiferromagnetic domain walls as well as the switching mechanism is mainly due to the difficulty of imaging antiferromagnets.

The main focus of this thesis is to address the aforementioned problems by imaging antiferromagnets using nanoscale scanning diamond magnetometry. We will elaborate throughout this thesis on the question what information about the spin structure can be inferred when measuring the magnetic stray field on the surface of an antiferromagnet. Related to that, we discuss current-induced effects in antiferromagnets and to what extent those can be detected using nanoscale diamond magnetometry.

We first calibrate our technique by determining the internal structure of a domain wall in a ferrimagnetic insulator  $\text{Tm}_3\text{Fe}_5\text{O}_{12}$  and estimate its magnetisation. Ferrimagnets, being in a broader sense between ferro- and antiferromagnets, are detectable by common magnetic probes, which we use to confirm our methodology. We reveal that the domain walls in  $\text{Tm}_3\text{Fe}_5\text{O}_{12}$  have a left Néel character indicating the presence of interfacial Dzyaloshinskii-Moriya interaction. These results open the possibility to stabilize chiral spin textures in centrosymmetric magnetic insulators important for spintronic applications.

We then extend these insights and methods to the archetypical antiferromagnet  $\text{Cr}_2\text{O}_3$ . Here we present, to the best of our knowledge, the first experimental observation of a domain wall in a pure, intrinsic antiferromagnet. We reveal that the intrinsic domain wall structure is Bloch-like and can become Néel-like if sufficient in-plane magnetic anisotropy is present. Our experimental observation is significant because theory does not predict any preference for Bloch or Néel domain wall structure.

Finally, we combine nanoscale scanning diamond magnetometry with electrical pulsing and resistance measurements to shed light on the switching mechanism and readout signal in the metallic antiferromagnet  $\text{CuMnAs}$ . We find that, besides the known reorientation of the Néel vector, the domain pattern fragments upon injection of current pulses. This provides an explanation for the recently-observed unipolar high-resistive switching signals in  $\text{CuMnAs}$ , and their relaxation and demonstrate a novel memristive effect. Besides these observations, we show that nanoscale scanning diamond magnetometry can be successfully applied to map the domain structure of in-plane antiferromagnets.

Our results point out directions for future research in the field of antiferromagnetic spintronics and provide new methodology and concepts relevant for the quantum sensing and imaging communities.



## Zusammenfassung

Verglichen mit den modernsten, auf Ferromagneten basierenden Datenspeichern, versprechen antiferromagnetische Materialien kleinere, schnellere und robustere Datenspeicher zu ermöglichen. Die Perspektive, die Orientierung magnetischer Domänen in Antiferromagneten mit elektrischen oder optischen Mitteln zu kontrollieren, revolutioniert das Forschungsfeld des Magnetismus und bietet eine Fülle an Anwendungen im Bereich Spintronik. Allerdings sind noch Fragen bezüglich fundamentaler Aspekte (Umschaltwechsel), sowie im Praxisbezug (Amplitude des Auslesesignals) zu klären. Eine der grossen Unbekannten im Fachgebiet des Antiferromagnetismus ist die Struktur der Domänenwand. Sie stellt einen wichtigen Faktor zur Lösung der beiden genannten Problemen dar. Beispielsweise sind chirale Wände unabdingbar für das stromkontrollierte Umschalten der Magnetisierung. Das bisher begrenzte Wissen über antiferromagnetische Domänenwände, sowie des Umschaltwechsels, sind überwiegend der Schwierigkeit geschuldet, Antiferromagneten abzubilden.

Der Fokus dieser Arbeit liegt darauf, die zuvor genannten Probleme durch das Abbilden von Antiferromagneten mittels der Nanorasterdiamantmagnetometrie anzugehen. Im weiteren Verlauf wird herausgearbeitet, welche Rückschlüsse durch die Messung des magnetischen Streufelds auf der Oberfläche eines Antiferromagneten über die Spinstruktur gezogen werden können. In diesem Zusammenhang diskutieren wir strominduzierte Effekte in Antiferromagneten und in welchem Masse diese durch die Nanorasterdiamantmagnetometrie erfasst werden können. Zuerst erfolgt eine Kalibrierung der Messtechnik, indem die innere Struktur einer Domänenwand in einem ferrimagnetischen Isolator  $\text{Tm}_3\text{Fe}_5\text{O}_{12}$  bestimmt und dessen Magnetisierung abgeschätzt wird. Ferrimagneten befinden sich in ihrer magnetischen Ordnung in einem breiteren Kontext gesehen zwischen Ferro- und Antiferromagneten. Sie sind daher mit herkömmlichen magnetischen Proben detektierbar, welche wir als Bestätigung unserer Methodik verwenden. Dabei zeigen wir, dass Domänenwände in  $\text{Tm}_3\text{Fe}_5\text{O}_{12}$  linksdrehend sind. Dies lässt auf das Vorhandensein einer Grenzflächen-Dzyaloshinskii-Moriya-Interaktion schliessen. Diese Ergebnisse eröffnen die Möglichkeit, chirale Spintexturen in zentrosymmetrischen magnetischen Isolatoren zu stabilisieren und sind daher von grosser Bedeutung für Spintronik-Anwendungen.

Anschliessend werden die Erkenntnisse und Methoden auf den archetypischen Antiferromagneten  $\text{Cr}_2\text{O}_3$  ausgeweitet. In dieser Arbeit zeigen wir, nach bestem Wissen, die erste experimentelle Beobachtung der Domänenwandstruktur in einem echten, intrinsischen Antiferromagneten. Wir erkennen, dass die intrinsische Domänenwand eine Bloch-artige Struktur aufweist und bei ausreichend starker in-plane magnetischer Anisotropie einen Néel Charakter annehmen kann. Dies ist dahingehend signifikant, dass die Theorie keine Präferenz für Bloch oder Néel vorhersagt. Abschliessend erfolgt eine Kombination der Nanorasterdiamantmagnetometrie mit elektrischen Pulsen und Widerstandsmessungen, um über den Umschaltwechsel und das Auslesesignal des metallischen Antiferromagneten  $\text{CuMnAs}$  Aufschluss zu geben. Neben der bekannten Umorientierung des Néelvektors, erkennen wir auch eine Fragmentierung des Domänenmusters unter der Induzierung von Strompulsen. Dies liefert eine Erklärung für die kürzlich beobachteten unipolaren

hochresistiven Umschalt-Signale in CuMnAs, sowie deren Relaxation und demonstriert einen neuartigen memristiven Effekt. Neben diesen Beobachtungen zeigen wir, dass die Nanorasterdiamantmagnetometrie erfolgreich auf in-plane Antiferromagneten angewendet werden kann.

Unsere Ergebnisse sind richtungsweisend für zukünftige im Gebiet der antiferromagnetischen Spintronik und liefern neue, für die Bereiche Quantensensorik und Bildgebung relevante Methoden und Konzepte.

# Acknowledgements

I'm equally grateful to *Prof. Pietro Gambardella* and *Prof. Christian L. Degen* who challenged and supported me throughout my doctoral studies. They provided me the necessary environment to discover something new.

I wish to thank Prof. Nicola Spaldin and Dr. Denys Makarov for being on the committee and the Swiss Competence Centre for Materials Science and Technology (CCMX) for supporting this work.

I thank *Pol Welter* for supporting me in performing and analysing the measurements. Without your expertise, the construction, assembling, and maintaining of the diamond magnetometer would have been much more painful. I'm grateful for all the support you gave me in conducting and analysing the experiments.

Special thanks goes to *Marcela Giraldo*, *Thomas Lottermoser* and *Prof. Manfred Fiebig* from the Multiferroics group at ETH Zurich for the pleasant and fruitful collaboration we had. I also thank Prof. Nicola Spaldin for gathering the expertise on that specific project and useful discussions.

I appreciate the interesting collaboration with *Zedeně Kašpar*, *Kamil Olejník* and *Prof. Tomas Jungwirth* from the Institute of Physics ASCR in Prague.

I thank all members of the Magnetism and Interface Physics group as well as the Spin Physics group for their aid, especially *Federico Binda*, *Christoph Murer*, *Kristian Cujia*, *Marius Palm*, *Jonathan Zopes*, *Phuong Dao*, *Manuel Baumgartner*, *Johannes Mendil*, *Giacomo Sala*, *Benjamin Jacot*, *Stepan Kovarik*, *Viola Krizakova*, *Gunasheel Kawwtilyaa*, *Krishnaswamy*, *Christian Stamm*, *Stefan Ernst*, *Luca Lorenzelli*, *Urs Grob*, *Konstantin Herb*, *Martin Héritier*, *Marc-Dominik Krass*, *Christa Leumann*, *Patrick Scheidegger*, *Takuya Segawa*, *Jan Rhensius*, *Tom Seifert*, *Charles-Henri Lambert*, *Can Onur Avcı*, *Saiül Vélez Centoral*, *Kevin Chang* and *Sebastian Stepanow*. I'm grateful to you for all the good discussions, sports events, and leisure activities we had together. Special thanks goes to our dear assistant *Rina Fichtl*. It was a pleasure to have someone outside of our subject area to talk and enjoying a cup of coffee.

Finally, I want to express my gratitude to my family who supported me and never stopped believing in me. I thank my oldest brother *Christoph* for facilitating my start into university life. I'm indebted to *Magdalena Schmied* for supporting me all these years during my studies and even before. You have been a source of strength in challenging times and never stopped having confidence in me.

In memory of Albert Schmied.



# Contents

<b>Abstract</b>	<b>v</b>
<b>Acknowledgements</b>	<b>ix</b>
<b>Abbreviations</b>	<b>xvi</b>
<b>1 Introduction</b>	<b>1</b>
<b>2 Magnetism and spintronics</b>	<b>7</b>
2.1 Magnetic interactions . . . . .	7
2.1.1 Zeeman energy . . . . .	7
2.1.2 Demagnetisation energy . . . . .	8
2.1.3 Magnetocrystalline anisotropy energy . . . . .	8
2.1.4 Exchange interaction . . . . .	8
2.1.5 Dzyaloshinskii-Moriya interaction . . . . .	9
2.2 Antiferromagnetic domains . . . . .	9
2.3 Domain walls . . . . .	11
2.4 Methods to image antiferromagnetic domains and walls . . . . .	13
2.5 Anisotropic magnetoresistance . . . . .	16
2.6 Spin torques . . . . .	16
<b>3 The nitrogen-vacancy centre in diamond – an atomic sized sensor</b>	<b>19</b>
3.1 Electronic structure of the NV centre in diamond . . . . .	19
3.2 Spin states of the nitrogen vacancy centre . . . . .	20
3.3 Optically detected magnetic resonance (ODMR) . . . . .	22
3.4 Pulsed ODMR . . . . .	23
3.5 Sensitivity of continuous wave ODMR and pulsed ODMR . . . . .	24
3.6 Angular dependency of the NV energy levels on the magnetic field . . . . .	28
<b>4 Construction of a nanoscale scanning diamond magnetometer</b>	<b>31</b>
<b>Experimental apparatus</b>	<b>31</b>
4.1 Quantum sensor tips . . . . .	31
4.2 Microscope head . . . . .	33
4.3 Optics module . . . . .	33
4.4 Magneto-optical Kerr microscopy . . . . .	35
4.5 Microwave module and control/readout electronics . . . . .	35
4.6 Magnetic field module . . . . .	36
4.7 Current source and switching matrix . . . . .	36

<b>5</b>	<b>Relations between magnetisation and magnetic field</b>	<b>39</b>
5.1	Magnetisation	39
5.1.1	Magnetostatic potential	39
5.1.2	Basic equations for a two-dimensional thin magnetic film	39
5.1.3	Decay function for ferromagnets	40
5.1.4	Decay function for antiferromagnets	40
5.1.5	Decomposition of the in-plane magnetisation	42
5.2	Reconstruction of the magnetisation	43
5.2.1	Out-of-plane magnetisation	43
5.2.2	In-plane magnetisation	45
	Recipe for reconstructing the in-plane magnetisation for a single domain orientation	45
5.2.3	Extract magnetisation from line scan	46
5.3	Vector magnetic field from an arbitrary projection and distance	47
5.3.1	Reconstruction of the vector magnetic field from an arbitrary projection	47
5.3.2	Calculation of magnetic field for arbitrary distance $z$	48
<b>6</b>	<b>High-speed domain wall racetracks in a magnetic insulator</b>	<b>49</b>
6.1	Introduction	49
6.2	Ferrimagnetic garnet $\text{Tm}_3\text{Fe}_5\text{O}_{12}$ (TmIG)	50
6.3	Domain wall structure and chirality in TmIG and TmIG/Pt	50
6.4	Domain wall dynamics	53
6.5	Saturation magnetisation	54
6.6	Conclusion	57
<b>7</b>	<b>Co-existence of Bloch and Néel walls in a collinear antiferromagnet</b>	<b>59</b>
7.1	Introduction	59
7.2	One-dimensional model of antiferromagnetic domain walls	60
7.3	Materials and methods	60
7.4	Experimental results	62
7.4.1	Domain states	62
7.4.2	Domain-wall cross-section	63
7.4.3	Surface magnetisation	64
7.4.4	Domain wall chirality and width	65
7.5	Discussion	65
7.6	Summary and Outlook	67
<b>8</b>	<b>Current-induced fragmentation of antiferromagnetic domains</b>	<b>69</b>
8.1	Introduction	69
8.2	Imaging an in-plane antiferromagnet with nanoscale scanning diamond magnetometry	70
8.2.1	CuMnAs samples	70
8.2.2	Reconstruction of the domain pattern	71
8.3	Current distribution and switching of CuMnAs microdevices	72
8.4	Current-induced domain fragmentation	74
8.5	Simulation of the fragmented domain state	76
8.6	Correlation between domain fragmentation and resistive readout signal	77
8.7	Domain wall resistance and electrical model	77
8.8	Discussion and outlook	80



<b>9</b>	<b>Conclusions and Outlook</b>	<b>83</b>
9.1	Summary of the main results . . . . .	83
9.2	Outlook . . . . .	85
<b>A</b>	<b>Calibration of the NV sensor</b>	<b>87</b>
A.1	Estimation of the spin vector orientation in the sensor . . . . .	87
A.2	Estimation of the sample-to-sensor distance $z$ . . . . .	87
<b>B</b>	<b>High-speed domain wall racetracks in a magnetic insulator</b>	<b>89</b>
B.1	Nanoscale scanning diamond magnetometry measurement - details . . . . .	89
B.2	Reconstruction of the surface magnetisation . . . . .	89
B.3	Determination of the sample-to-sensor distance $z$ . . . . .	90
B.4	Fits of the domain wall magnetisation profile . . . . .	91
B.5	Reference TmIG film . . . . .	91
<b>C</b>	<b>Co-existence of Bloch and Néel walls in a collinear antiferromagnet</b>	<b>93</b>
C.1	Materials and Methods . . . . .	93
C.1.1	Sample preparation . . . . .	93
C.1.2	Second harmonic generation measurements . . . . .	93
C.1.3	Nanoscale scanning diamond magnetometry measurements - details . . . . .	94
C.2	Data analysis . . . . .	94
C.2.1	Effective surface magnetisation $\sigma_z^0$ . . . . .	94
C.2.2	Reconstruction of the surface magnetisation $\sigma_z$ . . . . .	95
C.2.3	Magnetic field from surface roughness . . . . .	95
C.2.4	Fitting of line scans . . . . .	96
C.2.5	Complementary methods for estimating $\sigma_z^0$ . . . . .	96
C.2.6	Complementary method for estimating $\Delta_{DW}$ and $\chi$ . . . . .	97
C.3	Supplementary Figures . . . . .	97
<b>D</b>	<b>Current-induced fragmentation of antiferromagnetic domains</b>	<b>101</b>
D.1	Samples . . . . .	101
D.2	Nanoscale diamond magnetometry measurement - details . . . . .	101
D.3	Surface magnetisation in CuMnAs . . . . .	102
D.4	Reconstruction of the domain pattern . . . . .	102
D.5	Ferromagnetic defects . . . . .	102
D.6	Measurement of the current density distribution . . . . .	102
D.7	Simulation of fragmentation . . . . .	103
D.7.1	Simulation of the domain pattern using image to image trans- lation . . . . .	103
D.7.2	Generation of the domain pattern and corresponding magnetic stray field . . . . .	104
D.7.3	Introduction of fragmentation and domain wall density . . . . .	105
D.8	Current induced fragmentation on 50 nm thick CuMnAs . . . . .	106
D.9	Coexistence of non-uniform fragmentation and $180^\circ$ Néel vector switch- ing . . . . .	107
D.10	Stray field amplitude from atomic steps . . . . .	108
D.11	Temperature evolution in the cross-device during a typical writing pulse	109
	<b>Bibliography</b>	<b>111</b>





# Abbreviations

Abbreviation	Explanation
A	Analyser
AFM	Antiferromagnet
AMR	Anisotropic magnetoresistance
APD	Avalanche photodiode
AWG	Arbitrary waveform generator
BS	Beam splitter
BPD	Balanced photo-detector
CW	Continuous wave
DAQ	Data acquisition card
DM	Dichroic mirror
DMI	Dzyaloshinskii-Moriya interaction
F	Filter
FIM	Ferrimagnet
FM	Ferromagnet
FWHM	Full width half maximum
EPR	Electron paramagnetic resonance
GM	Galvanometric mirrors
LO	Local oscillator
MeFM	Magnetolectric force microscopy
MFM	Magnetic force microscope
MOKE	Magneto-optical Kerr effect
MRAM	Magnetic random access memory
NA	Numerical aperture
NSOT	Néel-order spin-orbit torque
NSDM	Nanoscale scanning diamond magnetometer
NV	Nitrogen vacancy
ODMR	Optically detected magnetic resonance
P	Polariser
PH	Pin-hole
PID-controller	Proportionalintegralderivative controller
SFM	Scanning Force Microscopy
SHG	Second harmonic generation
SNR	Signal-to-noise ratio
SOT	Spin-orbit torque
SPM	Scanning probe microscope
SP-STM	Spin-polarised scanning tunneling microscopy
STT	Spin-transfer torque
WLS	White light source
WP	Wollaston prism
XMLD-PEEM	X-ray magnetic linear dichroism with photo-emission electron microscopy
ZFS	Zero-field splitting

# Introduction

Antiferromagnetic materials have their magnetic moment direction alternating between individual lattice sites (see Fig. 1.1a). The resulting zero net magnetic moment makes them externally invisible to most common magnetic probes and hard to control, albeit they are internally magnetic [1]. As a consequence, they built a reputation of being *interesting and useless*. Curiously enough, one famous representative of that view was its explorer Louis Néel who won the Nobel prize in physics in 1970 precisely for the discovery concerning antiferromagnetism and ferrimagnetism [1, 2]. Initially antiferromagnetic systems remained, hence, in the shadow of ferromagnetic ones, its famous counterpart (see Fig. 1.1b). Those have been known for thousands of years and were subject of revolutionary technologies from sound recording more than a hundred years ago to modern data storage using spintronics (see Fig. 1.1d) [6].

However recently, antiferromagnetic materials are receiving widespread attention because they promise to enable even smaller, faster, and more resilient data processing units compared to state-of-the-art spintronic devices using ferromagnets. For instance, antiferromagnets (AFM) are insensitive to disturbing magnetic fields which allows for a higher bit density compared to ferromagnets (FM) as the bits are not magnetically affected by the surrounding elements [6]. Nowadays, competitive concepts of data storage devices require the ability to read and write information using microelectronics. In 2016, these prerequisites have been reported on AFMs in the seminal work of P. Wadley *et al.* [7] opening a wealth of applications in spintronics [1, 7]. The field is still at a very early and explorative stage as shown by the fast rate of new discoveries as well as by the appearance of controversial results that have been reported since then [7–15]. Also, the read and writing mechanism has only been tested on planar devices. Integration into a pillar device, as proposed in Fig. 1.1c, similar to resistive random access memories or magnetic random access memories as suggested in Fig. 1.1d), remains elusive so far [3]. Outstanding open questions are the mechanisms and type of reorientation of the magnetic states as well as the amplitude of the magnetoresistive readout signal. Here, the ability to image the magnetic state in AFMs is of fundamental importance to discuss these problems and prerequisite to explore the potential of antiferromagnetic materials for digital and analog memory functionalities, such as binary bits and spiking neural networks. While imaging of the ferromagnetic domains exists for decades antiferromagnetic domain imaging remained elusive until recently [16].

Related to that, one of the great unknowns in the field of antiferromagnetism is the structure of domain walls, which is key from both a fundamental and applied

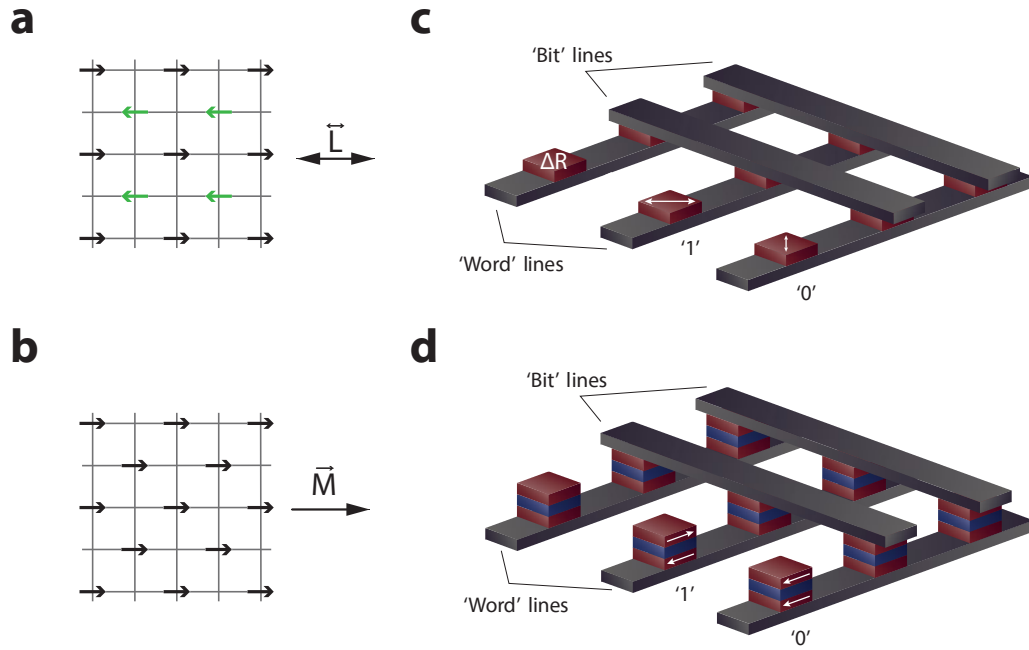


FIGURE 1.1: **Ferromagnetic and antiferromagnetic spintronics.** **a,b** Antiferromagnetic a and ferromagnetic order b. Arrows indicate the magnetic moments on the lattice sites. The antiferromagnetic and ferromagnetic order are typically described by the Néel vector  $\vec{L}$  and magnetisation  $\vec{M}$ , respectively. **c**, Memory concept using antiferromagnetic material (red blocks) to encode information in the orientation of the Néel vector  $\vec{L}$  or by modifying the resistivity  $\Delta R$  of the antiferromagnetic element similar to resistive random access memories [3]. **d**, Magnetic random access memory architectures employing two terminal spin-transfer torque (STT) [4]. These devices are actively developed and in production by leading actors in the semiconductor industry [5]. Adapted from Ref. [4].

perspective. In particular, chiral walls are required for current-controlled magnetisation reorientation [17]. The limited knowledge about antiferromagnetic domain walls mainly is due to the lack of techniques capable of spatially resolving the wall structure [16]. So far, the internal texture of domain walls could be only revealed in a few AFMs including monolayer-thick films [18] and those where the antiferromagnetic order is accompanied by strain [19] or defects [20]. However, there are no studies reporting on the domain wall structure of bulk intrinsic AFMs.

In this thesis, we use nanoscale scanning diamond magnetometry (NSDM) to investigate magnetic stray fields related to the magnetisation of ferro-, antiferro-, and ferrimagnetic materials to discuss the aforementioned problems. NSDM utilises a single lattice defect in a diamond tip, the so-called nitrogen-vacancy (NV) centre, as an atomic-size magnetic field sensor. The tip is scanned using atomic force microscope protocols, see Fig. 1.2. Exploiting quantum metrology, very high sensitivity is achieved. This opens the door to study the many interesting features that emerge from weakly magnetic nanoscale structures [21]. NSDM dates back to 2008 [22–24] and has so far enabled a number of nanoscale magnetic investigations, including the imaging of Bloch and Néel wall in ferromagnets [25], magnetic and superconducting vortices [26, 27], superparamagnetic nanoparticles [28], skyrmions [29, 30],

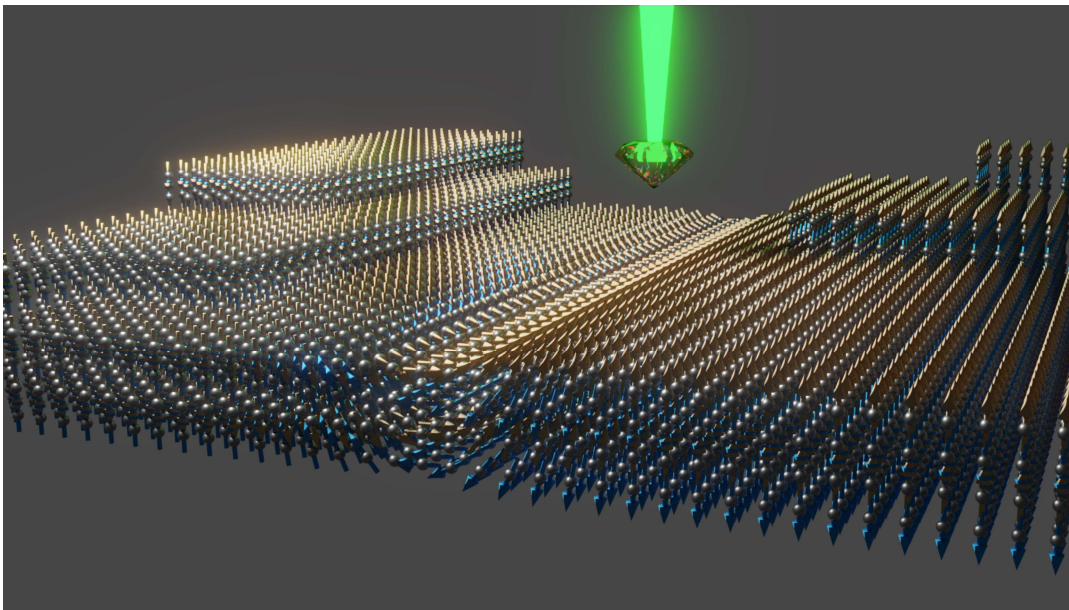


FIGURE 1.2: **Schematic of the nanoscale scanning diamond magnetometer.** A diamond tip containing an NV centre is scanned over an AFM film recording the magnetic stray field using spin dependent luminescence. Here we illustrate a layered AFM order, i.e. the magnetic moments, depicted by brown and blue arrows, point oppositely for all adjacent layer. The AFM reveals a domain wall where the moments rotate by  $180^\circ$ . The magnetometer is also sensitive to roughness (shown as steps) induced stray fields.

spin excitations [31], helimagnetic phase transitions and topological defect dynamics [32], imaging of current flow in metal nanowires and carbon nanotubes [33] and non-collinear antiferromagnetic order [34–38].

In order to address the aforementioned problems, we will elaborate throughout this thesis on the question of what information about the spin structure can be extracted when measuring the magnetic stray field related to it.

We start by analysing the magnetic stray field emanating from a domain wall in a magnetic insulator. The sample consists of 5 nm thick heavy metal stripes on top of a ferrimagnetic oxide. Applying a suitable model, we are able to reconstruct the internal structure of the domain wall and reconstruct the surface magnetisation. Our findings are confirmed by complementary techniques including the analysis of the domain wall dynamics using spatially resolved magneto-optical Kerr effect (MOKE) and SQUID magnetometry.

In the next step, we extend the methods and insight generated in that study to the antiferromagnetic insulator  $\text{Cr}_2\text{O}_3$ . Because  $\text{Cr}_2\text{O}_3$  is a pure and intrinsic  $180^\circ$  AFM, it is an ideal model system for studying domain walls. To resolve the domain wall, we combine high-resolution magnetic imaging (based on NSDM) with quantitative image reconstruction and analysis. We are able to resolve both the domain wall width and chiral angle, as well as the surface magnetisation with high sensitivity. To the best of our knowledge, this is the first experimental observation of the domain wall structure in a pure, intrinsic antiferromagnet.

Finally, we address the aforementioned questions regarding the seminal work by Wadley *et al.* [7]. The subject of that work is the archetypical AFM  $\text{CuMnAs}$ .

We combine for the first time NSDM with electrical pulsing and resistance measurements to shed light on the nature of the excited antiferromagnetic texture after the current injection. By mapping the very weak magnetic stray field emanating from the surface of CuMnAs, we show that the large resistive changes induced by unipolar current pulses are correlated with a nanoscale fragmentation of the antiferromagnetic domains. The fragmentation of the domains in CuMnAs by electrical pulses and their subsequent recovery are distinct effects from the reorientation of the Néel vector in the antiferromagnetic domains observed in previous studies. Our measurements shed light on the microscopic mechanisms leading to the electrical switching of metallic AFMs, demonstrate a novel memristive effect, and point out directions for future research in the field of antiferromagnetic spintronics and NV microscopy.

Our results show the various information which can be extracted by a subtle analysis of the magnetic stray field and demonstrate NSDM as a powerful measurement tool.

The thesis is structured as follows:

- In chapter 2 the basic magnetic interactions and magnetic ground states, such as ferro-, ferri-, and antiferromagnetic are described. We give a small introduction to the concept of domains and domain walls followed by a description of experimental techniques capable of imaging them. Finally, we explain a method to electrically manipulate and detect the orientation of the magnetic state in AFMs.
- Chapter 3 introduces the optical and magnetic properties of the NV centre in diamond. We demonstrate the basic concepts of magnetic field sensing and associated sensitivity which are relevant for this thesis.
- Chapter 4 provides a description of the construction of the experimental apparatus used throughout this thesis.
- In chapter 5 we explain the relation between magnetisation and magnetic field for ferromagnetic and antiferromagnetic materials. We show means to reconstruct the magnetisation from a single projection of the magnetic field map.
- In chapter 6, we determine the domain wall structure in a ferrimagnetic oxide  $\text{Tm}_3\text{Fe}_5\text{O}_{12}$  and estimate its surface magnetisation. We discuss complementary techniques confirming our findings.

This is based on the publication "*High-speed domain wall racetracks in a magnetic insulator*" (Ref. [39]).

- In chapter 7, we report on imaging of the interior structure of antiferromagnetic domain walls. To the best of our knowledge, this is the first experimental observation of the structure of a domain wall in a pure, intrinsic AFM. We use the antiferromagnetic insulator  $\text{Cr}_2\text{O}_3$  for our experimental demonstration.

This chapter is based on the publication "*Coexistence of Bloch and Néel walls in a collinear antiferromagnet*" (Ref. [36]).



- In chapter 8 we combine for the first time NSDM with electrical pulsing and resistance measurements to shed light on the mechanism and type of reorientation of the magnetic state in the metallic AFM CuMnAs.

This chapter is based on the publication "*Current-induced fragmentation of antiferromagnetic domains*" (Ref. [35]).

- In chapter 9 I present the conclusions and results of this thesis and give an outlook.



# Magnetism and spintronics

## Summary

*In this chapter we introduce the basic magnetic interactions between magnetic moments in a solid causing different types of magnetic ground states including ferro-, ferri- and antiferromagnetic states. Minimising the energy of these magnetic systems involves the formation of domains. Domains are connected areas with the magnetic order-parameter pointing in the same direction. In a next step, we describe the boundary region between adjacent domains, namely the domain walls, and compare their properties for ferromagnets and antiferromagnets. We present a selection of methods to image domains and domain walls in antiferromagnets with a couple of exemplary results. In the second part of this chapter we describe means to manipulate the order-parameter in antiferromagnets using spin currents and read their state electrically using the anisotropic magnetoresistance.*

---

## 2.1 Magnetic interactions

### 2.1.1 Zeeman energy

The Zeeman energy  $E_{\text{Zeeman}}$  describes the interaction of a magnetic field  $\vec{B}$  with the magnetic moment  $\vec{m}$ , which reads

$$E_{\text{Zeeman}} = -\vec{m} \cdot \vec{B}. \quad (2.1)$$

Assuming a continuous assembly of magnetic moments, we define the magnetisation as

$$\vec{M} = \frac{1}{V} \sum_{i=1} \vec{m}_i, \quad (2.2)$$

where  $V$  is the volume of the magnetic specimen and the sum runs over all magnetic moments in that volume. The Zeeman energy then reads

$$E_{\text{Zeeman}} = - \int_V \vec{M} \cdot \vec{B}. \quad (2.3)$$

The Zeeman energy favours parallel alignment of the magnetisation with a magnetic field [40].

### 2.1.2 Demagnetisation energy

The demagnetisation energy, also referred to as magnetostatic energy or dipolar energy, is connected to the magnetic field generated by the magnetic specimen itself [40–42]. It follows the relation

$$\nabla \cdot \vec{H}_{\text{dem}} = \nabla \cdot \vec{M}, \quad (2.4)$$

where  $\vec{M}$  is the magnetisation and  $\vec{H}_{\text{dem}}$  the demagnetising field. A discontinuity of the magnetisation, in particular at the boundaries of a magnetic body, gives rise to  $\vec{H}_{\text{dem}}$ . Commonly, the sources and sinks building up at the discontinuities of the magnetisation are modelled as fictitious magnetic charges. Those are comparable to electric charges with the difference that they can not appear isolated but need to be balanced by opposite charges. The field generated by these magnetic charges is directed opposite to the magnetisation and called demagnetising field inside the magnetic specimen and stray field outside of it. According to the Zeeman energy described in Eq. (2.1), the magnetostatic energy is minimised for vanishing  $\vec{H}_{\text{dem}}$  as this is oppositely directed to the magnetisation. The magnetostatic energy depends on the geometrical shape and orientation of the magnet moments of a magnetic body. For instance, assuming a thin film geometry, the demagnetising energy is much larger for the magnetic moments pointing out-of-plane than for an in-plane orientation. In this context, the magnetostatic energy is also understood as shape anisotropy, as the shape of the magnetic body defines the orientation of the magnetic moments to minimise the magnetostatic energy. The formation of magnetic domains with opposite magnetisation also provides means to reduce the magnetostatic energy.

### 2.1.3 Magnetocrystalline anisotropy energy

Similar to the aforementioned shape anisotropy, the magnetocrystalline anisotropy favours the moments to lie along with specific crystallographic directions, the so-called easy axes. The magnetocrystalline anisotropy has its origin in the crystal-field interaction and spin-orbit coupling. The orientation of an easy axes depends on the crystal structure. For instance, hexagonal and tetragonal structures show a uniaxial anisotropy with the magnetocrystalline anisotropy energy given, to lowest order, by

$$E_u = K \sin^2(\theta), \quad (2.5)$$

where  $K$  is the uniaxial anisotropy constant and the angle between the easy axis and the direction of the moments [42]. For extended details on different systems, such as cubic and orthorhombic, as well as expansion to higher order terms, we refer to Ref. [42].

### 2.1.4 Exchange interaction

The exchange interaction is of short-range nature and quantum mechanical in origin. It arises from the Coulomb interaction among electrons and Pauli exclusion principle and is commonly described by the Hamiltonian

$$\mathcal{H}_{\text{ex}} = - \sum_{ij} \mathcal{J}_{ij} \hat{S}_i \cdot \hat{S}_j. \quad (2.6)$$

Here, the dimensionless spin operators are denoted as  $\hat{S}_{i,j}$ . Equation (2.6) is generalised to a sum over all pairs of lattice sites  $(i, j)$ . The exchange constant  $\mathcal{J}_{ij}$  describes the strength of the interaction between the  $i^{\text{th}}$  and the  $j^{\text{th}}$  spin. Including only isotropic nearest neighbour interactions, the exchange constant simplifies to  $\mathcal{J}$ . The sign of the exchange constant  $\mathcal{J}$  defines the magnetic ground state. For instance,  $\mathcal{J} > 0$  ( $\mathcal{J} < 0$ ) favours a parallel (antiparallel) alignment of the spins, corresponding to a ferromagnetic (antiferromagnetic) ground state [41].

### 2.1.5 Dzyaloshinskii-Moriya interaction

The Dzyaloshinskii-Moriya interaction (DMI), induced by a broken inversion symmetry in the magnetic lattice and spin-orbit coupling, describes an antisymmetric coupling between neighbouring spins

$$\mathcal{H}_{\text{DMI}} = -\vec{D} \cdot (\hat{S}_i \times \hat{S}_j), \quad (2.7)$$

where  $\vec{D}$  is the DMI vector and  $\hat{S}_{i,j}$  are spin operators. The interaction is of short-range nature and causes the spins to couple perpendicularly with coupling strength and chirality given by  $\vec{D}$  [41, 43–46]. Originally, the DMI was proposed by Dzyaloshinskii in 1958 to explain the weak ferromagnetism appearing in antiferromagnetic bulk materials such as  $\alpha\text{Fe}_2\text{O}_3$  or  $\text{MnCO}_3$  [43]. Later on, Fert proposed in 1990, that the DMI is also present in thin magnetic films, where the surface or interface breaks the symmetry [46]. The DMI also stabilises the rotation sense of the magnetisation in chiral Néel domain walls as discussed in Section 2.3, for example in  $\text{Tm}_3\text{Fe}_5\text{O}_{12}/\text{Pt}$  [47, 48].

## 2.2 Antiferromagnetic domains

In the previous section, we have introduced various types of interactions between magnetic moments in a solid. We noted that the sign of the exchange constant causes the magnetic moments to align parallel for  $\mathcal{J} > 0$  or antiparallel for  $\mathcal{J} < 0$ , giving rise to two different types of magnetic order, namely ferromagnetic and antiferromagnetic (see Fig. 2.1a,b). The magnetic state is described by an order parameter. For instance, in FMs, the order parameter is the magnetisation  $\vec{M}$ . Generally, a sample must not necessarily exhibit a single magnetic state but can be an assembly of regions with order parameters of different orientations or phases. We refer to those regions as domains [16]. The reason for the formation of domains in FMs and AFMs is quite different. In FMs, the domains form and arrange themselves mainly in order to minimise the dipolar energy and demagnetising field [41]. In AFMs this cannot be the origin because due to its alternating ordering of magnetic moments and resulting zero magnetisation the demagnetising field is vanishingly small (see also Section 2.1.2).

Commonly, AFMs are viewed as two interpenetrating ferromagnetic sublattices with opposite orientations of the magnetic moments, enabling a large number of possible arrangements of the moments [40]. A selection of different antiferromagnetic ordering is shown in Fig. 2.1d,e. The large variety and complicated structure of AFMs requires a tailored definition of the order parameter, the so-called Néel vector [16]. For example,  $\text{CuMnAs}$  is a layered AFM, i.e. the AFM can be decomposed into ferromagnetic layers with opposite moments. A suitable Néel vector is a double-ended arrow as depicted in Fig 2.1b. A less obvious choice and orientation of the order parameter is illustrated in Fig. 2.1d for  $\text{Cr}_2\text{O}_3$ . Here, the Néel vector is defined as

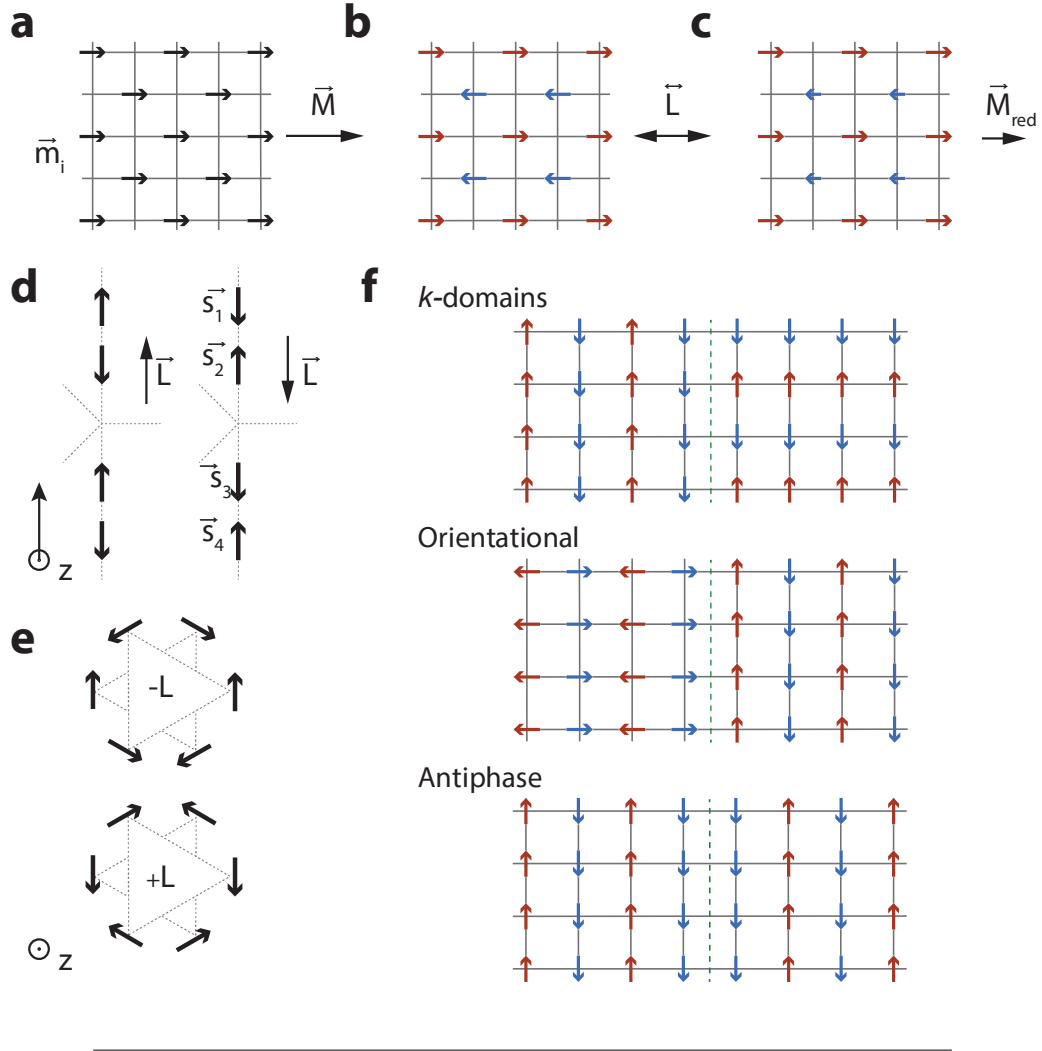


FIGURE 2.1: **Magnetic ground states and order parameter.** **a**, Ferro-, **b**, antiferro-, **c**, ferrimagnetic ground state. Arrows illustrate the magnetic moment  $\vec{m}_i$  on the lattice sites. The order parameter is shown on the right side of each magnetic ground state. FM and FIM generally use the magnetisation  $\vec{M}$  and reduced magnetisation  $\vec{M}_{\text{red}}$  as order parameter. AFMs are characterised by the Néel vector  $\vec{L}$ . **d**, Sketch of the antiferromagnetic order the [001] direction for opposite  $180^\circ$  domains in  $\text{Cr}_2\text{O}_3$ . The order parameter is defined as  $\vec{L} = \vec{s}_1 - \vec{s}_2 + \vec{s}_3 - \vec{s}_4$ . Adapted from Ref. [49]. **e**, Hexagonal manganites with  $B_2$  between adjacent planes along  $z$ . Planes are indicated by triangles with the Mn atoms located at the corners. The Néel vector  $L_\pm$  is shown in the centre. Adapted from Fig. [50]. **f**, Selection of antiferromagnetic domains and domain walls.  $k$ - and *orientational* domains are characterised by a change in the magnetic modulation direction and in the orientation of the antiferromagnetic spin arrangement, respectively. *Antiphase* domains occur due to phase shifts in the antiferromagnetic order. Adapted from Ref. [16].

$\vec{L} = \vec{s}_1 - \vec{s}_2 + \vec{s}_3 - \vec{s}_4$  and points in opposite directions in each domain [49]. Another example, showing the complexity and variety of AFMs, is hexagonal manganites with  $B_2$  coupling between adjacent planes along  $z$  [50]. As illustrated in Fig. 2.1e, the moments of the Mn atoms are oppositely directed between adjacent planes, depicted as triangles, and change by  $180^\circ$  for the Néel vector  $L_\pm$ . Note that in contrast to FMs, where only orientational domains exist, i.e. the domains differ in the orientation of the order parameter, in AFMs also translational domains exist. Those

are referred to as phase domain states [16]. The formation of domains in AFMs is a poorly understood subject. Typically it is associated with crystalline imperfections like twinned crystallographic regions, which break the long-range magnetic ordering [51]. Also magnetoelastic deformations and elastic defects such as disclinations and dislocations promote the formation of domains [52–54]. For a perfect crystal, a multidomain configuration can be favoured by the accompanying increase in entropy and hence reduction in the free energy [51].

The aforementioned description of AFMs employs two ferromagnetic sublattices with equal but oppositely orientated moments. If the magnetic moments of the two sublattices are not equal, we refer to the material as ferrimagnet (FIM), see Fig. 2.1c [40]. Those reveal a reduced magnetisation  $\vec{M}_{\text{red}}$  compared to FMs.

Examples for FM are Fe, Ni and Co, among which we study Co [40]. The second type of magnetic ordering, i.e. AFM, is abundant [6] of which we investigate the exemplary AFM  $\text{Cr}_2\text{O}_3$  and  $\text{CuMnAs}$ . The latter one has attracted considerable interest for the development of antiferromagnetic spintronic devices. An example for a FIM is  $\text{Tm}_3\text{Fe}_5\text{O}_{12}$ , a magnetic insulator, which we study in a later chapter.

## 2.3 Domain walls

This section follows partially the Supplementary Information of Ref. [36].

The regions between domains are called domain walls where the reorientation of the order parameter  $L$  takes place. Similar to domains, a large number of different domain walls exist. In Figure 2.1f, we show a selection of domain walls, including  $k$ -domains, orientational, and antiphase domain walls[16]. FMs reveal exclusively orientational domain walls.

In this section we briefly review the conventional model for static one-dimensional domain walls [55, 56] and extend it to collinear antiferromagnets in order to motivate and explain our experimental observations in Chapter 7. We consider a  $180^\circ$  domain wall, as it occurs in, for example,  $\text{Cr}_2\text{O}_3$ ,  $\alpha\text{-Fe}_2\text{O}_3$ , or  $\text{CuMnAs}$ . The domain wall separates two regions with magnetic order parameters pointing up ( $x < 0$ ) and down ( $x > 0$ ), as shown schematically in Fig. 2.2. The key parameters of such a domain wall are the wall width  $\Delta$  and the twist angle  $\chi$  between the wall magnetisation and the  $x$ -axis. Using this notation, Bloch walls correspond to  $\chi = \pm\pi/2$  and Néel walls to  $\chi = 0$  ( $\pi$ ) for walls with right (left) chirality.  $\Delta$  and  $\chi$  are determined by the interplay between exchange and anisotropy energies, and further modified by the demagnetising field and DMI, if present. Considering only the first two contributions, the local domain wall energy density in the continuum limit reads:

$$e = A \left[ \left( \frac{\partial\theta}{\partial x} \right)^2 + \sin^2\theta \left( \frac{\partial\phi}{\partial x} \right)^2 \right] + K \sin^2\theta, \quad (2.8)$$

where  $A$  is the exchange stiffness,  $K$  is the uniaxial anisotropy constant, and  $(\theta, \phi)$  are the polar coordinates of the order parameter defined relative to the  $z$ -axis shown in Fig. 2.2. The static equilibrium solution that minimises the total wall energy and satisfies the boundary conditions  $\theta(\pm\infty) = (0, \pi)$  is given by,

$$\phi(x) = \chi = \text{const}, \quad (2.9a)$$

$$\theta(x) = \pm 2 \arctan[\exp(x/\Delta)], \quad (2.9b)$$

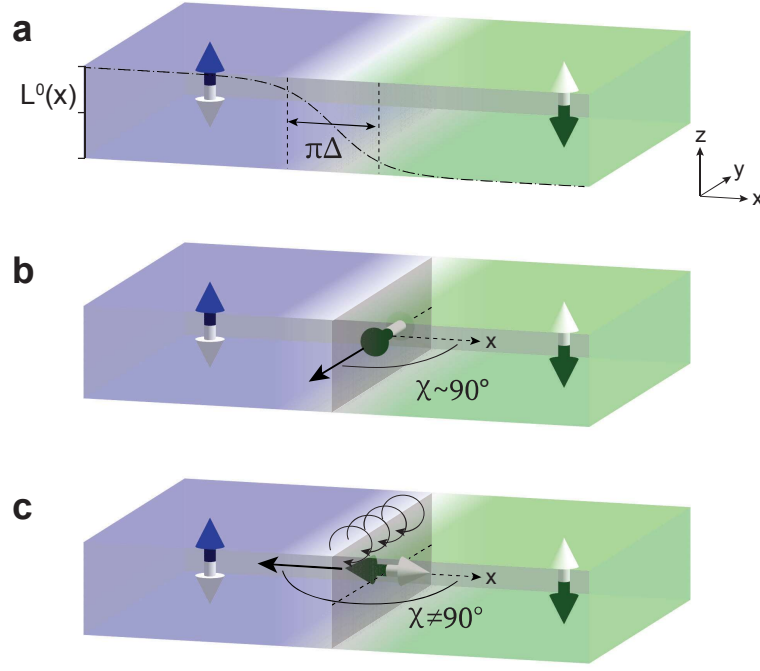


FIGURE 2.2: **One-dimensional model for an antiferromagnetic 180° domain wall.** **a**, Sketch of the domain wall separating regions (purple, green) of opposite order parameters. The dashed-dotted line describes the wall profile as given by Eq. (2.10). **b**, The presence of a residual demagnetising field favors the formation of Bloch walls ( $\chi = \pm\pi/2$ ). **c**, For sufficiently large in-plane anisotropy in a direction orthogonal to the wall, the formation of a Néel wall ( $\chi = 0, \pi$ ) or mixed Néel-Bloch wall is favored. Curled arrows indicate the demagnetising field arising from moments crossing the domain wall perpendicularly. Adapted from Ref. [36].

where  $\Delta = \Delta_0 := \sqrt{A/K}$  is the domain wall width [55, 57, 58]. The Cartesian coordinates of the order parameter can be easily derived from Eq. (2.9).

$$L_x(x) = L^0 \left[ \cosh \left( \frac{x - x_0}{\Delta} \right) \right]^{-1} \cos \chi, \quad (2.10a)$$

$$L_y(x) = L^0 \left[ \cosh \left( \frac{x - x_0}{\Delta} \right) \right]^{-1} \sin \chi, \quad (2.10b)$$

$$L_z(x) = L^0 \tanh \left( \frac{x - x_0}{\Delta} \right), \quad (2.10c)$$

where we assume a domain wall centred at  $x = x_0$ .  $L^0$  is the length of the order parameter, corresponding to the saturation magnetisation  $M_s$  in ferromagnetic systems. The profile of  $L_z(x)$  is shown by a dash-dotted curve in Fig. 2.2a. The total energy per unit area of the wall  $\epsilon_0$  is given by  $\epsilon_0 = 4\sqrt{AK}$ . We stress that, up to this point, the twist angle  $\chi$  is arbitrary and independent of  $x$ . In other words, for an antiferromagnetic system governed solely by exchange and anisotropy energies, Néel and Bloch domain walls (or any combination of the two) are degenerate in energy. To understand the preference for one type of wall over the other, we next consider the effects of a demagnetising field  $\mu_0 M$  and of an in-plane magnetic anisotropy energy



density  $K_{\text{ip}}$ . We note that, although the volume magnetisation  $M$  in an antiferromagnet is zero, a finite demagnetising field still persists when  $\phi \neq \pm\pi/2$  due to the net magnetic moment of the domain wall [57, 59]. Keeping in mind these additional contributions, the domain wall energy per unit area changes to [55]:

$$\epsilon = \epsilon_0 + \mu_0 M^2 \Delta_0 \cos^2 \chi + 2K_{\text{ip}} \Delta_0 \sin^2 (\chi - \psi_{\text{ip}}), \quad (2.11)$$

where the in-plane easy axis is defined by the angle  $\psi_{\text{ip}}$  relative to the  $x$ -axis. According to Eq. (2.11), the residual demagnetising field favors the formation of Bloch walls over Néel walls (Fig. 2.2b). On the other hand, the in-plane anisotropy forces the magnetic moments to cant along the in-plane easy axis, leading to a competition between demagnetising and anisotropy energies. For a sufficiently large in-plane anisotropy  $2K_{\text{ip}} > \mu_0 M^2$  favoring the  $x$ -direction ( $\psi_{\text{ip}} = 0$ ), we thus expect a Néel-type or a mixed Néel/Bloch-type domain wall (Fig. 2.2c). In other words, if there is an in-plane easy axis, the domain wall along this easy axis will be of Bloch type. If the domain wall runs perpendicular to the in-plane easy axis, the wall will be of Néel type. If the domain wall is tilted with respect to the easy axis, it can be of mixed Bloch-Néel type. The presence of a residual demagnetising field and of in-plane anisotropy also leads to a modification of the domain wall width

$$\Delta = \Delta_0 \left[ 1 - \frac{\mu_0 M^2}{4K} \cos^2 \chi - \frac{K_{\text{ip}}}{2K} \sin^2 (\chi - \psi_{\text{ip}}) \right]. \quad (2.12)$$

In particular, Eq. (2.12) predicts that the width of a Néel wall is reduced with respect to a Bloch wall, with a ratio given by

$$\frac{\Delta_{\text{Néel}}}{\Delta_{\text{Bloch}}} = 1 - \frac{\mu_0 M^2}{4K}, \quad (2.13)$$

where  $M$  is approximately given by the magnetisation of the polarised surface layer. Note that the ratio between the width of a Néel and Bloch type domain wall changes, if the system has lateral boundaries, for example, a domain wall in a narrow magnetised stripe [60].

In addition to these interactions, the DMI can further lead to a preference for Néel-type domain walls when the Dzyaloshinskii vector runs parallel to the domain wall direction as shown in Fig. 2.3 [55, 56, 61]. Note that we have omitted the local part of the dipolar interaction, which leads to the higher-order anisotropies as rigorously derived in the monographs of Turov and Akhieser [62, 63]. Usually, this dipolar-induced anisotropy is weaker than the magnetocrystalline one. However, in samples that have weak or no magnetocrystalline anisotropy, this dipolar-induced term will determine the behaviour of the system. The description of antiferromagnetic domain walls remains elusive for the lack of sufficient experimental data. However, recently published work aimed to explain theoretically antiferromagnetic domain wall dynamics [64–66]. A key property for the domain wall motion is the twist angle  $\chi$  which has been so far only touched in special cases [67].

## 2.4 Methods to image antiferromagnetic domains and walls

The aforementioned lack of sufficient experimental data to describe antiferromagnetic domain walls is owed to the fact that AFMs are invisible to most common magnetic probes such as MOKE or magnetic force microscope (MFM), which has been used decades to image FMs [16]. In contrast, the imaging of antiferromagnetic

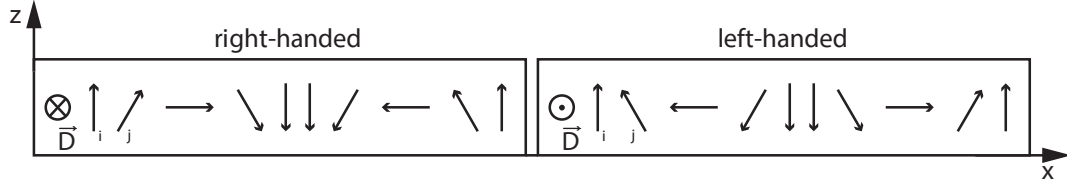


FIGURE 2.3: **DMI leading to a preference of Néel-type domain walls.** (Left)  $\vec{D}$  is pointing inwards along the  $y$ -axis, parallel to the domain wall (see Fig. 2.2). According to Eq. (2.7,  $\mathcal{H}_{\text{DMI}} = -\vec{D} \cdot (\hat{S}_i \times \hat{S}_j)$ ), a right-handed Néel domain wall with twist angle  $\chi = 0$  is stabilised. (Right)  $\vec{D}$  pointing outwards. In this configuration a left-handed Néel domain wall with twist angle  $\chi = \pi$  is energetically preferred over right-handed Néel type.

domains is comparatively new [16].

In this section we list a variety of techniques capable of imaging AFMs or even antiferromagnetic domain walls. We note that some of the techniques are mostly sensitive to domains, for example, second harmonic generation (SHG) and others to domain walls such as NSDM. X-ray magnetic linear dichroism with photo-emission electron microscopy (XMLD-PEEM) is able to resolve both. For the sake of completeness, we point out that AFMs can be also probed using secondary effects, for example by introducing a FM which couples to the antiferromagnetic order via the exchange bias [16, 68]. Note also that a variety of AFMs have a small net magnetisation due to DMI as mentioned in Section 2.1.5, which can be imaged using common magnetic probes. For extended details, we refer to Ref [16]. The following imaging techniques can be classified into optical, scanning probe microscopy and synchrotron X-ray techniques [16].

When referring to optical techniques, we distinguish between linear (frequency conserving) and nonlinear (frequency changing) methods. The former one usually probe the magnetic ordering via the change of the polarisation of the transmitted light. In 1960, purely antiferromagnetic domains have been first observed in NiO using a linear optical technique [69]. The simplest type of nonlinear techniques is called SHG. In contrast to the linear techniques, SHG is rather sensitive to the symmetry of the material than to the magnetisation. SHG was first demonstrated on  $\text{Cr}_2\text{O}_3$  [70] and later used to resolve the antiferromagnetic  $180^\circ$  domain pattern in  $\text{Cr}_2\text{O}_3$  [71] (see Fig. 2.4a) and hexagonal  $\text{YMnO}_3$  [72].

Imaging AFMs using scanning probe microscopy (SPM) includes spin-polarised scanning tunneling microscopy (SP-STM), magnetoelectric force microscopy (MeFM) and NSDM. The former one is capable, with its atomic resolution, of resolving the internal structure of antiferromagnetic domain walls. However, it is limited to samples fulfilling a list of requirements, such as atomically flat surfaces, small domain size, etcetera. In Fig. 2.4b, an antiphase antiferromagnetic domain wall on a monolayer Fe/W is shown, which was measured in the seminal work of Bode *et al.* [73] by SP-STM. Another techniques with less requirements on the surface properties is MeFM which can be applied to magnetoelectric AFM. The MeFM employs a MFM with in-situ modulated electric fields. The coupling between magnetic and electric properties, inherent to the family of magnetoelectric AFMs, induces a magnetisation which is detected by MFM. The MeFM was first demonstrated on hexagonal  $\text{ErMnO}_3$  by Geng *et al.* [75] in 2014. In Figure 2.4c, domains on the archetypal magnetoelectric  $\text{Cr}_2\text{O}_3$  are shown, demonstrating MeFM as a powerful visualisation tool for the

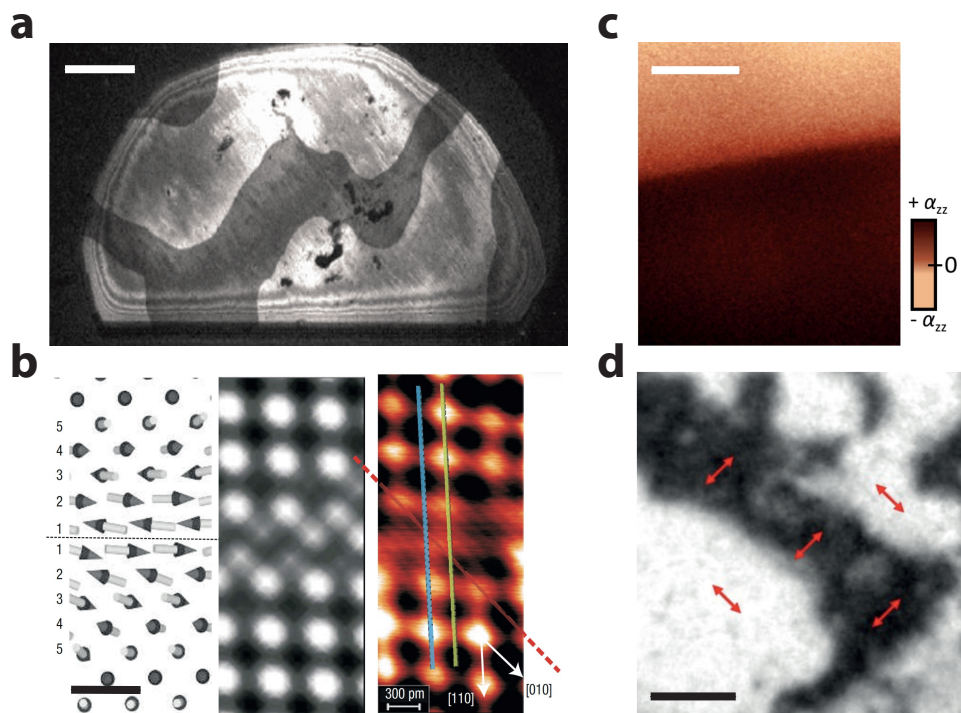


FIGURE 2.4: **Various imaging methods of AFM domains.** **a**, SHG image of the  $180^\circ$  domain pattern in a z-orientated  $\text{Cr}_2\text{O}_3$  sample. Scale bar is 1 mm. Adapted from Ref. [71]. **b**, SP-STM image of an antiphase domain wall on an antiferromagnetic Fe monolayer on W(001). The panels show from left to right the theoretical spin structure, the stimulated and experimental SP-STM image. Scale bar is 600 pm. Adapted from Ref. [73]. **c**, MeFM image showing a domain wall on z-orientated  $\text{Cr}_2\text{O}_3$ . Scale bar is  $25\ \mu\text{m}$ . Adapted from Ref. [74]. **d**, XMLD-PEEM image of the domain pattern on CuMnAs. The double-headed arrows indicate the orientation of the Néel vector. Scale bar is  $1\ \mu\text{m}$ . Adapted from Ref. [13].

family of magnetoelectric AFM [74]. The subject of this thesis is the investigation of the antiferromagnetic properties by sensing the magnetic stray field emanating from an antiferromagnetic specimen using NSDM. The visualisation of antiferromagnetic domains, and more precisely of domain walls, by NSDM has been realised so far on  $\text{Cr}_2\text{O}_3$  [36, 76, 77],  $\text{BiFeO}_3$  [78],  $\text{CuMnAs}$  [35] and  $\text{ErMnO}_3$  [79]. In a later chapter we will discuss the requirements on the magnetic texture in general, to produce detectable magnetic stray fields.

Finally, we address the probing of antiferromagnetic domains and walls with synchrotron X-rays. According to Ref. [16], the studies employing synchrotron X-rays are classified into scattering experiments able to resolve the Néel vector, for instance on  $\text{BiFeO}_3$  [80], coherent X-ray imaging in Bragg condition detecting antiphase domain boundaries [81] and absorption techniques. The latter one, in particular XMLD-PEEM, is relevant for this thesis. The X-ray absorption cross section is, despite the dominating electric dipole terms, also proportional to the average of the square of the local magnetisation  $\langle M^2 \rangle$  and is similar present for ferromagnetic and antiferromagnetic materials. A magnetic contrast is obtained by subtracting the absorption intensity between horizontal and vertical incident polarisation. XMLD-PEEM probes with a spatial resolution down to 20 nm-30 nm, a field of view of

typical 10  $\mu\text{m}$  and is sensitive to the surface magnetic layers, depending on the escape depth of the secondary electron which is typically 6-7 nm [16]. In Figure 2.4d, we show the domain pattern in CuMnAs recorded by XMLD-PEEM.

## 2.5 Anisotropic magnetoresistance

The anisotropic magnetoresistance (AMR) is a magnetotransport effect and describes the dependency of the electrical resistivity on the relative orientation of the current direction and the magnetic moment. Its discovery goes back to 1857 by William Thomson in ferromagnetic metals [82] and is rooted in a spin-dependent scattering cross section of the electrons due to relativistic spin-orbit coupling [83]. The AMR is an even function of the magnetic moment and therefore applies, as stated by Néel, also on AFMs [1]. The AMR can be quantified as

$$R_{xx} = R_0 + \beta_{\text{AMR}} \cos(2\alpha), \quad (2.14)$$

where  $R_0$  is the materials resistance and  $\alpha$  the angle between current direction and the magnetic moment. The constant

$$\beta_{\text{AMR}} = \frac{1}{2} \left[ R_{xx}(\vec{m} \parallel \vec{j}) - R_{xx}(\vec{m} \perp \vec{j}) \right], \quad (2.15)$$

is defined as the change in the longitudinal resistance  $R_{xx}$  for a current flowing parallel or perpendicular to the magnetic moments, respectively [14]. When comparing the AMR among different materials, the figure of merit is given by  $\beta_{\text{AMR}}/R_0$  and is a few percent for ferromagnetic systems, such as Ni, Fe and Co [84]. Antiferromagnetic materials, like CuMnAs, reveal a AMR of 0.1% [8, 13, 85]. In this thesis we exclusively use the transverse geometry, depicted in Fig. 2.5a, to detect the AMR. The transverse AMR is given by [14]

$$R_{xy} = \beta_{\text{AMR}} \sin(2\alpha). \quad (2.16)$$

## 2.6 Spin torques

The term spin torque refers to the effect of a spin density exerting a torque on the local magnetisation, i.e. the transfer of angular momentum from the spin density to the local magnetisation [88]. We group the spin torques according to their origin of the spin density or accumulation into spin-transfer torques (STT) and spin-orbit torques (SOT). The former one was predicted by Slonczewski [89] and Berger [90] in 1996 and describes the transfer of angular momentum of a spin-polarised current of conduction electrons to the local magnetisation. In most advanced ferromagnetic MRAM devices current-induced STT are used for writing. The STT has the form

$$d\vec{m}/dt = \tau_{\text{FL}} \vec{m} \times \vec{p} + \tau_{\text{DL}} \vec{m} \times (\vec{m} \times \vec{p}), \quad (2.17)$$

where  $\vec{m}$  is the magnetic moment of the FM and  $\vec{p}$  the electrically injected carrier spin-polarisation. The first term with amplitude  $\tau_{\text{FL}}$  corresponds to the field-like (FL) torque. The second term with amplitude  $\tau_{\text{DL}}$  is of damping-like (DL) nature, i.e. it either enhances or hinders the precessional motion of the magnetisation [91]. Typically, a fixed ferromagnetic layer is used to spin polarise a charge current before injecting it into a free ferromagnetic layer [4].

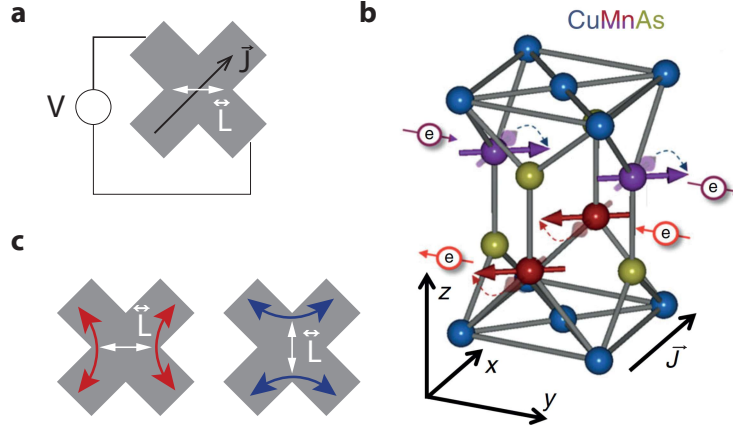


FIGURE 2.5: **Manipulating and probing the Néel vector in CuMnAs.** **a**, Measurement geometry for the detection of the AMR with the readout current  $\vec{J}$  and transverse voltage detection  $V$ . The white double sided arrow illustrates the Néel vector. Adapted from Ref. [86]. **b**, A writing current  $\vec{J}$  (black arrow) generates a spin-polarisation which alternates between the antiferromagnetic spin sublattices (purple and red arrow on the electron symbol). The NSOT causes the magnetic moment on Mn sites to be deflected. Adapted from Ref. [87]. **c**, Orthogonal writing pulses (red and blue double sided arrow). The pulses align the Néel vector perpendicular to the current flow as illustrated in b, enabling a  $90^\circ$  reorientation of the Néel vector. Applying the measurement geometry in a, the readout signal is maximised, see Eq. (2.16). Adapted from Ref. [86].

SOT rely on the transfer of angular momentum from the orbital to the spin momentum of the electrons and originates from the band structure itself. As a result, whenever a current is flowing through the material, a spin accumulation is generated [92]. There are various different mechanism causing the SOT, such as spin Hall effect or Rashba effect, which depend on the material properties and device geometry. For details on this subject we refer to the recent review paper [91]. Note that the symmetry of the SOT and STT is the same and described by Eq. (2.17).

Naturally, in AFMs, the spin torque resulting from the injection of a spin-polarised spin current will average to zero. Železný *et al.*[93] proposed that translating efficient spin torques to AFMs requires the spin torques to alternate sign between AFM sublattices. The spin torque then reads

$$d\vec{m}_{A,B}/dt = \tau_{\text{FL}}\vec{m}_{A,B} \times \vec{p}_{A,B} + \tau_{\text{DL}}\vec{m}_{A,B} \times (\vec{m}_{A,B} \times \vec{p}_{A,B}), \quad (2.18)$$

with  $A, B$  denoting the sublattices of the AFM [1, 7]. In other words, a global current needs to generate a local carrier spin-polarisation which changes sign between the antiferromagnetic sublattices, so that  $\vec{p}_A = -\vec{p}_B$ . This is possible for an AFM in which the antiferromagnetic sublattices form space-inversion partners and have a local broken inversion symmetry. The carrier spin-polarisation is considered to originate from the inverse spin-galvanic effect. These torques are called Néel order spin-orbit torque (NSOT) or Néel torques. Examples of materials showing Néel torques are  $\text{Mn}_2\text{Au}$  [15, 94] and  $\text{CuMnAs}$  [7] from which we illustrate the latter one in Fig. 2.5b. A current  $\vec{J}$ , shown by an black arrow, generates a carrier spin polarisation  $\vec{p}$  that alternates between the two antiferromagnetic sublattices, indicated as arrow on the purple and red electron symbols. The NSOT causes the magnetic

moment on the Mn atom, here illustrated as purple and red arrow on the lattice sites, to be deflected. The NSOT is supposed to align the Néel vector perpendicularly to the current direction [7]. Applying orthogonal current pulses enables a  $90^\circ$  rotation of the Néel vector as depicted in Fig. 2.5c. Here, the device geometry maximises the readout signal in Fig. 2.5a as the writing current in Fig. 2.5c aligns the Néel vector  $45^\circ$  with respect to the reading current.



# The nitrogen-vacancy centre in diamond – an atomic sized sensor

## Summary

*The Nitrogen vacancy (NV) centre is one of many colour defects existing in diamond [95]. It consists of a substitutional nitrogen atom next to a vacancy [96]. The NV centre's potential for quantum technology was revealed in 1997 by the first detection of electron paramagnetic resonance (EPR) from a single NV centre [97] and developed since then for a variety of applications [96]. Due to its photostability and low cytotoxicity, NV centres have been used, for instance, as robust single-photon emitters [98] and fluorescent biomarkers [99]. NV centres are atomic sized and show quantum behaviour up to room temperature [96]. The quantum mechanical interaction between the spin state and external perturbations enables a number of physical quantities, most prominently magnetic [97] and the measurement of electric fields [100]. In this chapter, we give a basic description of the NV centre and quantum sensing applications. We describe the magnetic states of the NV centre in its electronic ground state and its interaction with external perturbations. In the next step, we show how the NV centre can be used as a sensor of different physical quantities, such as magnetic and electric field, as well as strain, pressure and temperature. Finally, we introduce methods to optimise the sensor sensitivity. For more details on this subject we refer to recent review papers [21, 96, 101–103].*

---

## 3.1 Electronic structure of the NV centre in diamond

The NV centre exists in three possible charge states,  $NV^0$ ,  $NV^+$ , and  $NV^-$ , where only the latter one provides optical access to the spin state via spin dependent luminescence and is of use for magnetic field sensing [96]. In this thesis, we will exclusively focus on the negative charge state and refer to it as NV. The molecular orbitals are defined by the axial  $C_{3v}$  symmetry of the defect and filled in the ground state with 6 electrons originating from the nitrogen atom (2 electrons), the dangling bonds of the carbon atoms (3 electrons), and one electron captured from the lattice. The energy levels of the degenerate  $e$  orbitals, and one of the  $a_1$  orbital are located deep inside the diamond gap (5.5 eV) giving rise to the NV centre's photostability. The remaining  $a_1$  orbital lies within the valence band of the diamond host [104]. Optical excitation changes the configuration of the orbital occupation from  $a_1^2 e^2$  to  $a_1^1 e^3$

in the band gap.

In Figure 3.1a, the energy level diagram for the NV centre and the available optical transitions are shown. It consists of a triplet ground  $|g\rangle$  and excited state  $|e\rangle$  as well as a metastable singlet state  $|s\rangle$ . Transitions between  $|g\rangle$  and  $|e\rangle$  are spin conserving with a radiative lifetime of 13 ns. The transition probability for a decay from  $|e\rangle$  to the long-lived ( $\tau = 250$  ns) singlet state  $|s\rangle$  is however spin dependent and much higher for the spin sublevels  $|e, m_s = \pm 1\rangle$ . This additional non radiative decay channel leads to a spin dependent luminescence as illustrated in Fig. 3.1c by the time-resolved luminescence. Here, the NV centre is initially prepared in the  $|g, m_s = 0\rangle$  state (red),  $|g, m_s = \pm 1\rangle$  state (blue) ground state, respectively. An electron excited from the  $|g, m_s = \pm 1\rangle$  to the  $|e, m_s = \pm 1\rangle$  has a significant probability to decay over the non-radiative meta stable state  $|s\rangle$ . In contrast, an electron prepared in the  $|g, m_s = 0\rangle$  ground state is excited to the  $|e, m_s = 0\rangle$  where it mostly decays via the fast radiative transition leading to an optical contrast of approximately 30% between the  $|g, m_s = \pm 1\rangle$  and  $|g, m_s = 0\rangle$  spin sublevels of the ground state [96]. The contrast is temporary, as for longer (in Fig. 3.1c about 1  $\mu$ s) laser illumination the decay via the  $|s\rangle$  state polarises the electron to  $|g, m_s = 0\rangle$  and can reach up to 95% [96, 101]. The ability to initialise and read out the spin state of the NV centre are important prerequisites for quantum sensing and information processing applications [21].

## 3.2 Spin states of the nitrogen vacancy centre

The NV centre's spin Hamiltonian for the electronic ground state provides the basis for understanding the various sensing applications. It defines the spin eigenstates of the NV centre in the electronic ground state and describes how perturbations, such as magnetic fields, alter the eigenstates and cause a shift of the energy eigenvalues (see Fig. 3.1b). The NV centre's spin Hamiltonian here includes the zero-field splitting caused by the spin-spin interaction, the magnetic Zeeman splitting, electric interaction, and the hyperfine interaction due to the nitrogen nuclear spin. Following Ref. [96, 106, 107] the Hamiltonian reads

$$\frac{\mathcal{H}}{\hbar} = D \underbrace{\left( \hat{S}_z^2 - \frac{2}{3} \right)}_{\text{ZFS}} + \underbrace{\gamma_e \vec{B} \cdot \vec{S}}_{\text{Zeeman}} + \underbrace{\vec{S} \mathbf{A} \vec{I}}_{\text{hyperfine}} + \underbrace{\gamma_{^{15}\text{N}} \vec{B} \cdot \vec{I}}_{\text{nuclear Zeeman}} + \mathcal{H}_{\text{electric}}, \quad (3.1)$$

where

$$\mathcal{H}_{\text{electric}} = \epsilon_z E_z \left( \hat{S}_z^2 - \frac{2}{3} \right) + \epsilon_{xy} \left[ E_x (\hat{S}_x \hat{S}_y + \hat{S}_y \hat{S}_x) + E_y (\hat{S}_x^2 + \hat{S}_y^2) \right]. \quad (3.2)$$

Here,  $D$  denotes the zero-field splitting (ZFS) parameter,  $\vec{B}$  a vector magnetic field,  $\gamma_e$  the electron's gyromagnetic ratio, and  $\mathbf{A}$  the hyperfine coupling tensor acting on the nuclear spin of the nitrogen atom. Although  $^{14}\text{N}$  is the most abundant isotope of nitrogen, for fabrication reasons, all NV sensors employed in this thesis exclusively exhibit the  $^{15}\text{N}$  isotope with spin  $I = 1/2$  and gyromagnetic ratio  $\gamma_{^{15}\text{N}}$ .  $E_i$  are the vector electric field components and  $e_z, e_{xy}$  the corresponding electric field coupling constants. The NV centre's symmetry axis defines, by convention, the  $z$ -direction, which points along the  $[111]$  crystal direction. In Table 3.1 we list the coupling constants. We note that the magnetic interaction due to the Zeeman effect is by far



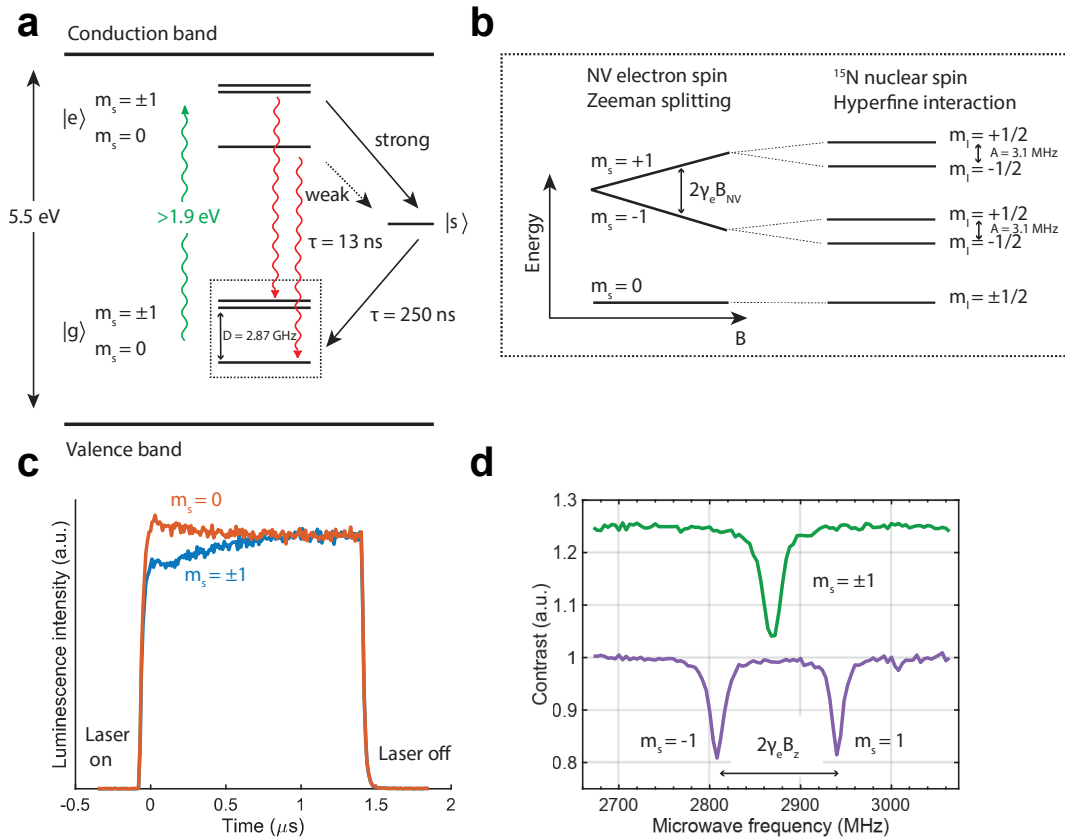


**FIGURE 3.1: Properties of the NV centre.** **a**, The energy level diagram of the NV centre is located deep inside the band gap of the diamond host crystal. Its electronic ground and excited state consist of spin-triplet sublevels. Optical excitation (relaxation) are indicated by green (red) wiggly arrows. An additional, non-radiative decay channel is given over a third long-lived metastable singlet state and shown by solid black arrows. The singlet state couples stronger to the  $|e, m_s = \pm 1\rangle$  spin sublevels of the excited state and relaxes to the  $|g, m_s = 0\rangle$  sublevel in the ground state. This slower and selective relaxation causes spin dependent luminescence and spin polarisation. Adapted from Ref. [96, 105] **b**, (Left) Energy levels of the ground state for a magnetic field  $B_{NV}$  applied along the high symmetry axis of the NV centre, i.e. along the [111] direction of the diamond crystal. The spin sublevels  $|g, m_s = \pm 1\rangle$  split due to the Zeeman effect by  $2\gamma_e B_{NV}$ . (Right) The hyperfine interaction of the NV electron spin with the intrinsic  $^{15}\text{N}$  nuclear spin ( $I = 1/2$ ) leads to an additional splitting of the spin sublevels by  $A = 3.1\text{ MHz}$ . Adapted from Ref. [105]. **c**, Time-resolved luminescence of the NV centre initially prepared in the  $|g, m_s = 0\rangle$  state (red),  $|g, m_s = \pm 1\rangle$  state (blue), respectively. Due to the spin dependent luminescence, a contrast between the blue and red curve is observed. Adapted from Ref [96, 103]. **d**, Optical detected magnetic resonance ODMR for zero magnetic bias field (blue) and for a magnetic field of 1.7 mT applied along the NV centre symmetry axis (red).

Quantity	Coupling coefficient	Typical sensitivity	Reference
Magnetic field	$\gamma_e = 28 \text{ GHz T}^{-1}$	$0.36 \mu\text{T}/\sqrt{\text{Hz}}$	[24, 96, 108–110]
Electric field	$\epsilon_z = 0.17 \text{ Hz V}^{-1} \text{ m}$ $\epsilon_{xy} = 3.5 \times 10^{-3} \text{ Hz V}^{-1} \text{ m}$	$5.8 \text{ kVcm}^{-1}/\sqrt{\text{Hz}}$ $280 \text{ kVcm}^{-1}/\sqrt{\text{Hz}}$	[96, 100, 107]
Temperature	$\partial D/\partial T = -74 \text{ kHz K}^{-1}$	$0.13 \text{ K}/\sqrt{\text{Hz}}$	[96, 111–113]
Pressure	$\partial D/\partial P = 1.5 \text{ kHz bar}^{-1}$	$6.8 \text{ bar}/\sqrt{\text{Hz}}$	[96, 114]

TABLE 3.1: Properties of a typical NV centre. Coupling coefficients and related common sensitivities. Adapted from reference [96].

stronger than the electric interaction caused by the Stark effect and spin-orbit coupling. The energy levels further shift due to pressure, and temperature which affect the ZFS. We simplify Eq. (3.1) by omitting the electric interaction and the nuclear Zeeman effect as they couple weakly to the NV centre’s spin. The hyperfine interaction further splits the energy levels, as illustrated in Fig. 3.1b, leading to additional spin resonances. The hyperfine splitting amounts to  $A = 3.1 \text{ MHz}$  and is independent on the applied magnetic field, adding only an offset to the spin resonance frequency [115]. In the following, the hyperfine interaction will not be considered in the description of the NV centre’s ground state. The NV centre’s Hamiltonian then reads

$$\frac{\mathcal{H}}{\hbar} = D \left( \hat{S}_z^2 - \frac{2}{3} \right) + \gamma_e \vec{B} \cdot \vec{S}. \quad (3.3)$$

In the case of a small magnetic field  $\vec{B}$  which is perfectly aligned with the NV centre’s symmetry axis, the ZFS is the dominating interaction and the other effects can be regarded as perturbations. In that case, the spin resonances shift linearly with an applied magnetic field. The NV centre hence provides a calibration-free measurement of a magnetic field according to the relation

$$B_{\text{NV}} = \Delta\nu/\gamma_e. \quad (3.4)$$

Here,  $B_{\text{NV}}$  is the field along the NV centre’s symmetry axis.

### 3.3 Optically detected magnetic resonance (ODMR)

The phenomenon of optically detected magnetic resonance (ODMR) is a consequence of the combination of spin-dependent luminescence and spin polarisation. The Zeeman effect acting on the spin sublevels  $m_s$  in the ground state provides the physical mechanism for using the NV centre as a magnetic field sensor. In its most basic form, the spin state is optically determined by sweeping an auxiliary microwave field over the electron paramagnetic resonance (EPR) frequency. While continuously pumping with a laser ( $\lambda \approx 532 \text{ nm}$ ) the excited state  $|e\rangle$ , excitations from  $|g, m_s = 0\rangle$  to  $|g, m_s = \pm 1\rangle$  occur at the EPR frequency and such preparing the NV centre in the

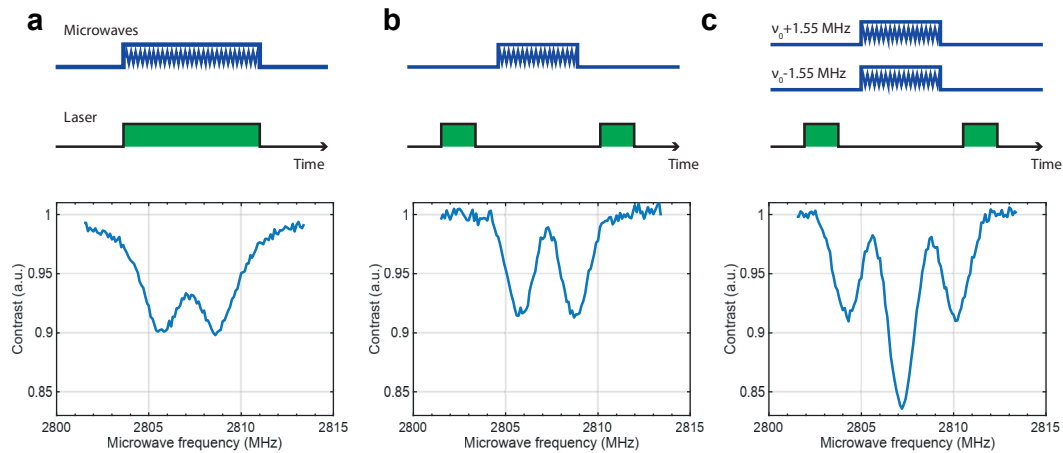


FIGURE 3.2: **Sensing protocols, showing pulse-timing diagrams (Top) and example measurements (bottom).** **a**, CW ODMR detection of the hyperfine splitting caused by the nitrogen nuclear spin of the  $^{15}\text{N}$  isotope. Microwave and laser power are adjusted such that the linewidth is minimal while preserving the optical contrast. **b**, Pulsed ODMR with narrower linewidth compared to CW ODMR in **a**. The  $\pi$ -pulse length of the microwave pulse is set to  $T_\pi = 600$  ns. **c**, Pulsed ODMR with same  $\pi$ -pulse length as in **b**. The microwaves are additionally modulated at the frequency 1.55 MHz. The centre dip of the ODMR spectra is twice as deep compared to the unmodulated spectra recorded in **b**. The contrast of the side dips are similar to those observed in **b**.

$|g, m_s = \pm 1\rangle$ . This leads to a reduction of the luminescence as explained in Fig 3.1c. Applying an external magnetic field lifts the degeneracy via the Zeeman effect and results in two EPR frequencies, separated by  $2\gamma_e B_{\text{NV}}$ . Here, we consider continuous excitation by the laser and microwave, which is known as continuous wave (CW) ODMR. The sensing protocol is illustrated as a pulse-timing diagram in Fig. 3.2a (Top). The sensitivity to detect weak magnetic fields depends on the microwave and laser power. In Section 3.5, we will describe how the sensitivity can be optimised by adjusting the microwave and laser power. For an appropriate choice of both, it is then possible to resolve the EPR splitting due to the hyperfine coupling with the nuclear spin of  $^{15}\text{N}$  as shown in Fig. 3.2a. The hyperfine splitting is recorded on the lower spin resonance of the ODMR spectra shown in Fig. 3.1c.

The NV centre can be used as a sensor, following the aforementioned experimental protocol, for any physical quantity altering the spin energy level, provided that the physical quantity can be disentangled from all others appearing in the NV Hamiltonian.

In the next section, we see how the magnetic field sensitivity can be further increased using pulsed experiments.

### 3.4 Pulsed ODMR

In contrast to CW experiments, in pulsed experiments, the laser is turned off during the sensing period. The advantage of pulsed experiments is that the spectral broadening is reduced compared to CW experiments, which can lead to higher sensitivity [103]. This approach relies on a pump-probe scheme with the NV centre first initialised by a laser pulse followed by a sensing period where the spin system is

manipulated by microwave pulses. Finally, the system is read out by a second laser pulse. There are many refined microwave sequences available for recording magnetic resonances [116], among which the pulsed ODMR experiment is, due to its robustness, relevant for this thesis and described next.

The experimental protocol for pulsed ODMR is illustrated in Fig 3.2b (Top). After optical initialisation of the NV centre into the state  $|g, m_s = 0\rangle$  in the ground state, a microwave pulse with frequency  $\nu_m$  is applied followed by optical readout. If the microwave pulse is resonant with one of the EPR transitions and the duration such that the resulting rotation is exactly  $\pi$ , the NV centre's spin state is transferred from  $|g, m_s = 0\rangle$  to  $|g, m_s = \pm 1\rangle$ . This results in an optical contrast due to the different luminescence intensities for the NV centre prepared in the  $|g, m_s = 0\rangle$  or  $|g, m_s = \pm 1\rangle$  state, see Fig. 3.1c. In order to increase the duty cycle, readout and initialisation of the the spin state is completed within one laser pulse. In Figure. 3.2b, we show an ODMR spectrum recorded with pulsed ODMR. The spectral power broadening is completely cancelled, which can be seen on a much narrower linewidth of the spectra compared to Fig. 3.2a.

Next, we present a measurement protocol, that exploits the hyperfine splitting in order to increase the contrast by almost a factor of two while mostly preserving a narrow linewidth. Thus, the sensitivity can be significantly increased, as we will see in the next section. In general, when sweeping the microwave frequency over the spin resonances, we only address one hyperfine level  $m_I$  at a time. However, by adding additional excitation channels to the spin sublevels  $|g, m_s = \pm 1\rangle$ , i.e. exciting both hyperfine levels simultaneously, the probability for the system to decay over the metastable state  $|s\rangle$  increases. Consequently, the luminescence intensity decreases, and therefore the optical contrast  $\epsilon$  increases. In order to address both hyperfine levels simultaneously, we modulated the microwaves at a frequency of  $\nu_{\text{mod}} = 1.55 \text{ MHz}$  which corresponds to half of the hyperfine splitting, see Fig. 3.1b. In other words we apply two microwave pulses of frequency  $\nu_m \pm \nu_{\text{mod}}$  as illustrated in Fig 3.2c (Top). Naturally, as can be seen in the same figure, three dips are observed in the ODMR spectra of which the side dips have a contrast similar to Fig. 3.2b and centre dip has twice that contrast.

### 3.5 Sensitivity of continuous wave ODMR and pulsed ODMR

In this section, we compare the sensitivity of CW ODMR and pulsed ODMR, i.e. the ability to detect weak magnetic fields. We introduce a relaxation mechanism limiting the sensitivity and present methods to optimise the sensitivity during the experiment. For extended details, we refer to Ref. [103]. We note that the sensitivity here is defined for dc magnetic field sensing. For the detection of ac signals see for instance Ref. [21, 105].

The intensity  $C$  of the EPR spectra or in other words, the rate of detected photons as a function of microwave frequency  $\nu_m$  can be described as

$$C(\nu_m) = C_0 \left[ 1 - \epsilon \cdot \mathcal{F} \left( \frac{\nu_m - \nu_{\text{res}}}{\Delta\nu} \right) \right], \quad (3.5)$$

where  $C_0$  stands for the rate of detected photons when the NV centre is in the bright  $|g, m_s = 0\rangle$  state and  $\epsilon$  for the EPR contrast, i.e. the reduction in luminescence intensity at the EPR resonance  $\nu_{\text{res}}$ . The function  $\mathcal{F}$  accounts for the fact that the EPR can be fitted, depending on the measurement protocol, by a Lorentzian or Gaussian profile with linewidth  $\Delta\nu$  [103]. For the same linewidth, a Gaussian profile has

somewhat steeper flanks, allowing to determine the centre frequency more accurately. However, this difference is marginal in most situations. In this thesis, we exclusively use a Lorentzian profile to fit the EPR spectra.

The sensitivity can be defined as the minimal shift of the EPR resonance by the frequency  $\delta\nu$  which is still detectable. The change of the resonance frequency  $\nu_{\text{res}}$  is seen by a variation of the luminescence intensity  $\delta C$ , which is largest at the points of maximum slope in the EPR profile. For a Lorentzian shape these are given at  $\nu_{\text{m}} - \nu_{\text{res}} = \Delta\nu/\sqrt{3}$ . The following derivation of the sensitivity is adapted from Ref. [117]. The luminescence intensity, i.e. the count-rate, responds to a shift in resonance frequency at the points of maximum slope

$$\delta C = \frac{\partial C}{\partial \nu_{\text{m}}} \delta \nu = \frac{3\sqrt{3}\epsilon C_0}{8\Delta\nu} \delta \nu. \quad (3.6)$$

The signal-to-noise ratio (SNR) is ultimately limited by shot noise giving the lower bound of the sensitivity

$$\text{SNR} = \frac{\delta C}{\sqrt{C}} = \frac{3\sqrt{3}\epsilon C_0 \delta \nu}{8\Delta\nu \sqrt{C}}. \quad (3.7)$$

We define the minimum detectable frequency shift for a SNR of 1 and approximate the count rate at the maximum slope  $C$  for the case of  $\epsilon \ll 1$  by the count rate  $C_0$ , such that

$$\delta \nu_{\text{min}} = \frac{8\Delta\nu}{3\sqrt{3}\epsilon \sqrt{C_0}}. \quad (3.8)$$

The minimum detectable signal  $\delta \nu_{\text{min}}$  scales with the contrast  $\epsilon$ , the linewidth  $\Delta\nu$  of the EPR spectra, and the count-rate  $C$ . The contrast and linewidth depend on the microwave power, the linewidth, and count-rate on the laser power [33, 103]. In general, for optimising the sensitivity one needs to choose an appropriate microwave and laser power. Unfortunately, a large microwave power and therewith a large contrast is not compatible with a small linewidth. Similarly, a large laser power results in a high count rate, however is also accompanied by a broadening of the EPR spectra [103, 118]. For CW ODMR, the optimal microwave and laser power can be found by recording a two-dimensional plot of the magnetic sensitivity for different microwave and laser powers as shown in Fig. 3.3. The magnetic sensitivity for CW ODMR in units of T/ $\sqrt{\text{Hz}}$  is calculated using Eq. (3.8), Eq. (3.4) and reads

$$\eta_{\text{Mag}}^{\text{CW}} = \frac{8\Delta\nu}{3\sqrt{3}\epsilon \sqrt{C_0} \gamma_e}. \quad (3.9)$$

In the example shown in Fig. 3.3 it can be decreased significantly down to  $\eta_{\text{Mag}}^{\text{CW}} = 2.6(2) \mu\text{T}/\sqrt{\text{Hz}}$  using appropriate values of microwave and laser power. For extended details, including a simplified model of the NV defect spin dynamics describing Fig. 3.3, we refer to Ref. [103].

In order to circumvent the laser power-induced broadening of the EPR one needs to separate the optical detection from the microwave excitation. The most basic protocol fulfilling these requirements is the aforementioned pulsed ODMR. As schematically shown in Fig. 3.4a, the spin state is read for the time  $T_{\text{sig}}$  and subsequently initialised for the time  $T_{\text{init}}$  resulting in an overall duration of the laser pulse of typically 2  $\mu\text{s}$ . Between the laser pulses a microwave pulse of length  $T_{\pi}$  is employed. Hereby, the linewidth is substantially reduced while preserving a high contrast. The

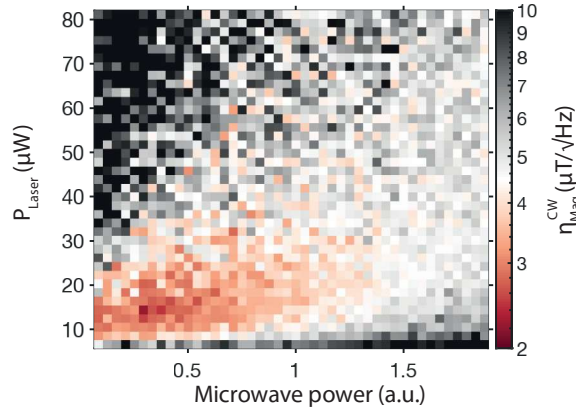


FIGURE 3.3: **Optimising the magnetic sensitivity for CW ODMR.** Two-dimensional plot of the magnetic sensitivity  $\eta_{\text{Mag}}^{\text{CW}}$  for different laser power and microwave powers. The magnetic sensitivity  $\eta_{\text{Mag}}^{\text{CW}}$  is calculated using Eq 3.9 with the linewidth  $\Delta\nu$  and  $\epsilon$  extracted from one of the hyperfine peaks of the ODMR spectra shown in Fig. 3.2a. The sensitivity strongly reduces with increasing laser or microwave power due to spectral power broadening.

sensitivity can be enhanced by up to one order of magnitude compared to a well-adjusted CW ODMR [103]. The pulsed ODMR spectra is determined by the convolution of the Fourier transform of the microwave pulse with length  $T_\pi$  and the Lorentzian profile describing the inhomogeneous dephasing of the NV centre's spin state. The FWHM of the latter one, is proportional to  $\propto 1/T_2^*$ , where  $T_2^*$  is the spin dephasing time. It is limited by low frequency magnetic noise of the nuclear spin bath, associated for example with the isotope  $^{13}\text{C}$  within the lattice and ranges up to a few microseconds in bulk diamond samples [96, 106]. We approximate the Fourier transform of the microwave pulse by Gauss function, resulting in Voigt profile of the pulsed ODMR spectra, where the linewidth is given by

$$\Delta\nu \propto \sqrt{(1/T_\pi)^2 + (1/T_2^*)^2} \quad (3.10)$$

Naturally, the linewidth of the recorded spectra scales with  $1/T_\pi$  until the coherence time  $T_2^* \propto T_\pi$  is reached. Then, the linewidth is given by the NV centre's intrinsic linewidth  $\Delta\nu_0 = 1/T_2^*$  as shown in Fig. 3.4c. However, further increasing of  $T_\pi$  reduces the contrast  $\epsilon$  while keeping the linewidth  $\Delta\nu$  unchanged, see Fig. 3.4d. Hereby, the contrast  $\epsilon$  is reduced due to decoherence and relaxation causing the pickup of random phase and spin-flip processes. Phenomenologically, the impact of the decoherence on the contrast can be described as

$$\epsilon(t) = \epsilon_0 e^{-(t/T_\chi)^a}, \quad (3.11)$$

where  $\epsilon_0$  is the contrast without decoherence and  $T_\chi$  is the decoherence time or relaxation time. The constant  $a$  is 1 for a Lorentzian fit [21]. The repetition time  $T_{\text{Seq}}$  is illustrated in Fig. 3.4a. Having the laser switched off during the sensing period, naturally its duty cycle and hence count rate reduces according to

$$C'_0 = C_0 \cdot \frac{T_{\text{Sig}}}{T_{\text{Seq}}}, \quad (3.12)$$



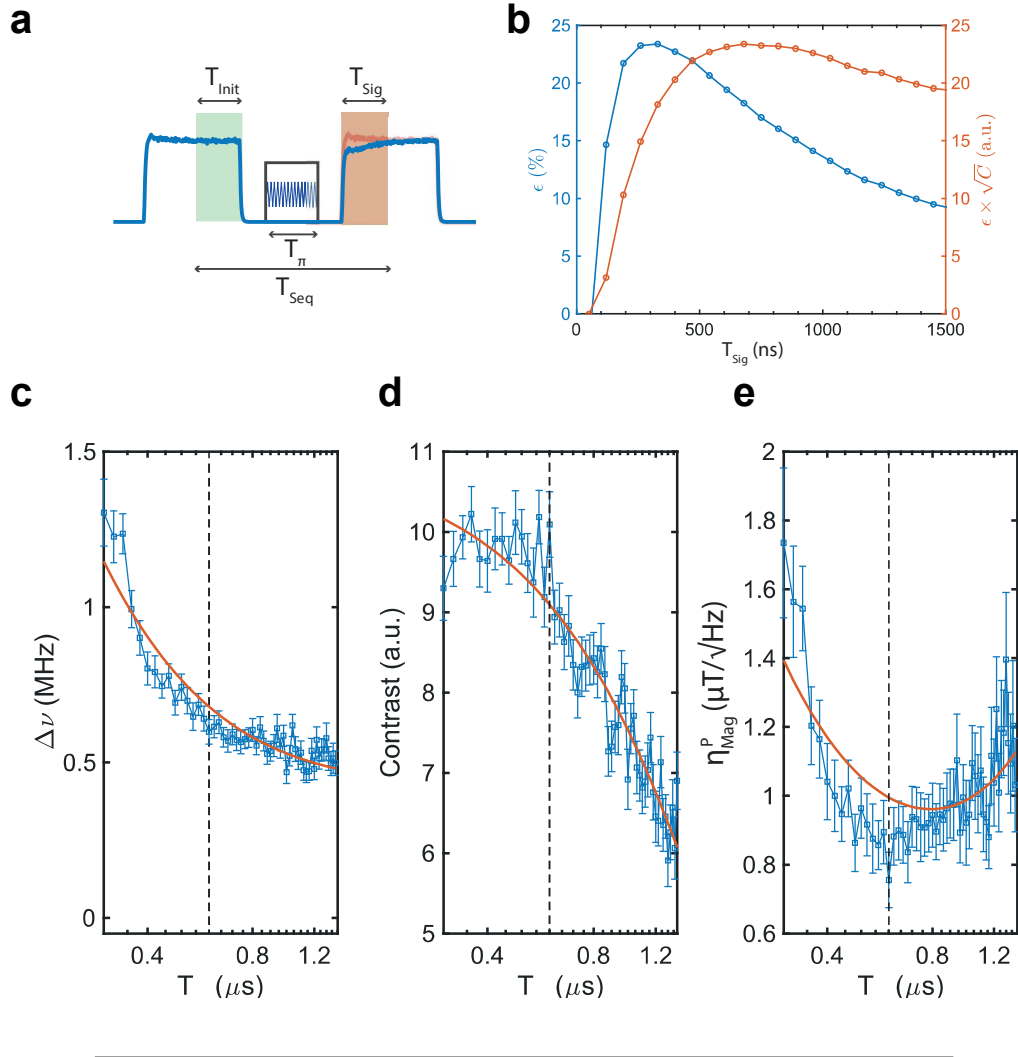


FIGURE 3.4: **Optimising the magnetic sensitivity for pulsed ODMR.** **a**, Pulse sequence of pulsed ODMR and relevant measurement times. The NV centre is first initialised for the duration  $T_{\text{init}}$  by a laser pulse (shaded green) followed by a microwave pulse of length  $T_{\pi}$ . Finally the NV state is read out by a second laser pulse (shaded red) for the duration  $T_{\text{sig}}$ . The repetition time of the sequence is denoted as  $T_{\text{seq}}$ . Between the laser and microwave a waiting time of 100 ns is inserted in order to guaranty a separation of optical detection and microwave manipulation. **b**, (Blue) EPR contrast  $\epsilon$  as a function of the readout time  $T_{\text{sig}}$ . Maximum contrast is obtained for an integration time of  $T_{\text{sig}} \approx 300$  ns. (Red) Optimised integration time  $\epsilon \times \sqrt{C}$  which also includes the square root of the count-rate entering Eq. (3.13). The optimised integration time has a broad maximum around 600 ns. We set the integration time for all pulsed experiments to  $T_{\text{sig}} = 600$  ns. **c,d**, Linewidth  $\Delta\nu$  (c) and contrast  $\epsilon$  (d) of the ODMR spectra for different microwave powers and corresponding  $\pi$ -pulse lengths  $T_{\pi}$ . While the linewidth  $\Delta\nu$  approaches the intrinsic linewidth of the EPR spectra, given by the dephasing time  $T_2^*$ , the contrast  $\epsilon$  reduces with increasing  $\pi$ -pulse length  $T_{\pi}$ , due to decoherence processes. The solid line in c is data fit of Eq. (3.10). The solid line in d is a data fit of Eq. (3.11) leading to  $T_{\chi} = 2.2(2)$   $\mu\text{s}$ . **e**, Magnetic sensitivity, calculated using Eq. (3.13) and the linewidth and contrast shown in panel c,d. The best sensitivity is given for a  $\pi$ -pulse length of  $T_{\pi} = 600$  ns and is  $\eta_{\text{Mag}}^{\text{P}} = 0.76(6)$   $\mu\text{T}/\sqrt{\text{Hz}}$ . The solid line is given by Eq. (3.13) where we insert the data of the solid lines from c and d. Dashed line in c-e indicates the optimum  $T_{\pi}$  pulse length.

with the repetition time  $T_{\text{Seq}}$  of the pulse sequence and readout time  $T_{\text{Sig}}$ , see Fig. 3.4a. Inserting the reduced count-rate from Eq. (3.12) into Eq. (3.9) we obtain

$$\eta_{\text{Mag}}^{\text{P}} \approx \frac{8\Delta\nu}{3\sqrt{3}\epsilon\sqrt{C_0 \cdot \frac{T_{\text{Sig}}}{T_{\text{Seq}}}\gamma_e}}. \quad (3.13)$$

For a fixed laser power the optimal sensitivity is found by varying the  $\pi$ -microwave pulse length, see Fig. 3.4e. It reflects a trade-off between contrast  $\epsilon$ , linewidth  $\Delta\nu$  and count-rate  $C$ . The optimal sensitivity is usually given for a  $\pi$ -microwave pulse length of approximately  $T_\pi = T_2^*$  [103]. In the example shown here, we reach a sensitivity of  $\eta_{\text{Mag}}^{\text{P}} \approx 0.76(6) \mu\text{T}/\sqrt{\text{Hz}}$  which is more than five times higher than for an optimised CW ODMR recorded with a similar sensor.

The sensitivity can be further increased by optimising the readout time of the laser pulse  $T_{\text{Sig}}$ . As can be seen in Fig. 3.4b (blue) the contrast  $\epsilon$  increases with the readout time until a maximum at 300 ns is reached. Longer readout times reduce the contrast. Keeping in mind that the sensitivity not only depends on the contrast  $\epsilon$  but also on the square root of the count-rate  $\sqrt{C}$  the optimised readout time is estimated by the maximum of  $\epsilon \times \sqrt{C}$ . The optimised readout time  $\epsilon \times \sqrt{C}$  (red) is shown in Fig. 3.4b and has a broad maximum around 600 ns for a laser power of 320  $\mu\text{W}$ .

### 3.6 Angular dependency of the NV energy levels on the magnetic field

The NV centre senses the vector projection of the magnetic field  $\vec{B}$  along the symmetry axis

$$B_{\text{NV}} = \vec{B} \cdot \vec{e}_{\text{NV}} = \sin \theta_{\text{NV}} \cos \phi_{\text{NV}} B_x + \sin \theta_{\text{NV}} \sin \phi_{\text{NV}} B_y + \cos \theta_{\text{NV}} B_z, \quad (3.14)$$

where  $\vec{e}_{\text{NV}}$  is the orientation of the symmetry axis which is described by the polar and azimuth angle  $\theta_{\text{NV}}$  and  $\phi_{\text{NV}}$  (see Fig. 3.5a). For small magnetic fields which are not perfectly aligned with the NV centre's symmetry axis, Eq. (3.4) is an approximation. In Figure 3.5c,d, we quantify the error made for erroneously assuming a linear conversion of spin resonance to magnetic field for the same field amplitude acting on the NV centre. The error in per cent is calculated as the difference  $\delta\nu$  between the spin resonance  $\nu_{\text{Lin}}$ , estimated from Eq. (3.4), and the spin resonance  $\nu_{\text{Ham}}$  obtained by solving the NV Hamiltonian given in Eq. (3.3) and normalised by  $\nu_{\text{Lin}}$  (see also Fig. 3.5b). Here,  $\theta$  denotes the angle between the magnetic field  $B$  and the NV centre's symmetry axis. The error is different for the lower  $|g, m_s = -1\rangle$  and higher  $|g, m_s = 1\rangle$  spin resonance as expected from Fig. 3.5b. For reasonably well aligned ( $\theta < 30^\circ$ ) and weak magnetic fields ( $B < 10\text{mT}$ ), Eq. (3.4) is a good approximation (error  $< 1\%$ ). Throughout this thesis we will use Eq. (3.4) to estimate the magnetic field.



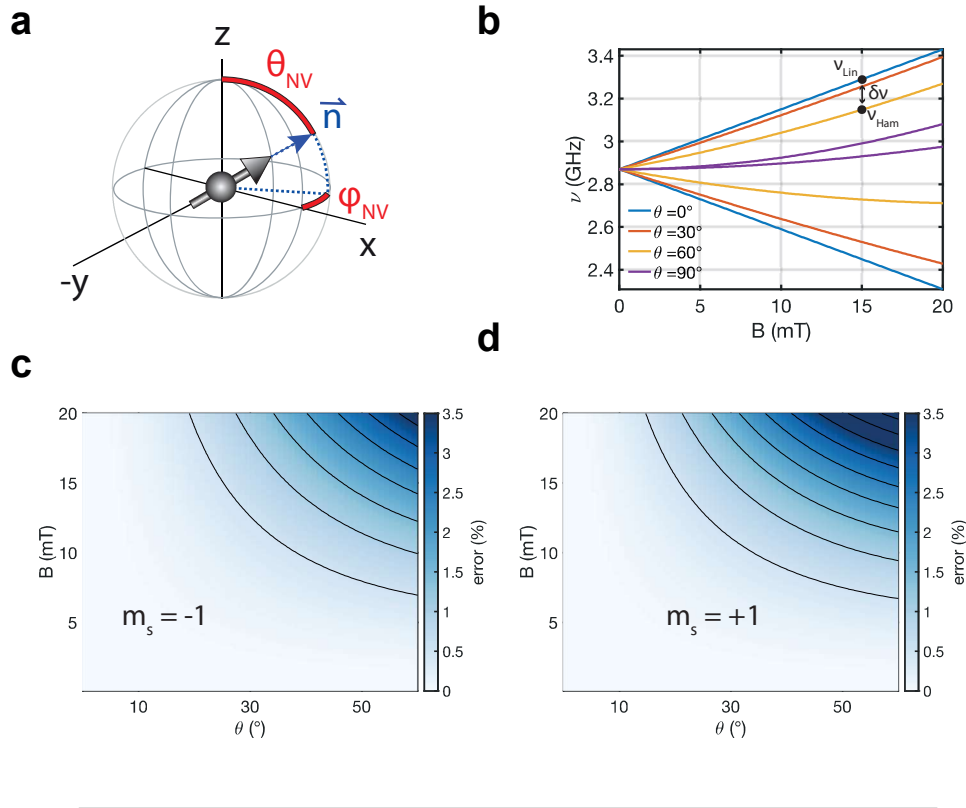


**FIGURE 3.5: Angular dependence of the NV ground energy levels on the magnetic field.** **a**, Coordinate system, defined by the sample stage. The spin of NV centre points along the  $[111]$  direction of the diamond host, specified by the polar and azimuth angle  $\theta_{\text{NV}}$  and  $\phi_{\text{NV}}$ . For fabrication and setup reasons the polar angle of the NV sensor, employed in this thesis, is fixed to  $\theta_{\text{NV}} = 54.7^\circ$ . **b**, Energy of the spin states described by the Hamiltonian in Eq. (3.3) for different angles  $\theta$  between the NV centre's symmetry axis and an applied magnetic field  $B$ . The deviation from the linear relation given in Eq. (3.4) increases with the angle and magnetic field  $B$ . **c,d** Error map for different magnetic fields  $B$  and angles. The error is calculated by the deviation  $\delta\nu = \nu_{\text{Ham}} - \nu_{\text{Lin}}$  and normalised to  $\nu_{\text{Lin}}$ , see also panel b. Here,  $\nu_{\text{Lin}}$  is the energy level according to the linear relation Eq. (3.4) for a given magnetic field  $B$ . The actual energy level  $\nu_{\text{Ham}}$ , is calculated by solving the Hamiltonian Eq. (3.3). As can be seen from panel b, the error is different for the spin sublevels  $|g, m_s = \pm 1\rangle$ .



# Construction of a nanoscale scanning diamond magnetometer

## Experimental apparatus

### Summary

*In this chapter, we introduce the experimental apparatus employing the NV as a magnetic field sensor. The nanoscale scanning diamond magnetometry setup is based on the design developed in the group of Prof. Degen. It combines a scanning probe microscope, an optical excitation and detection system, microwave channels for magnetic manipulation of the NV sensor and the sample under study, and a magnetic field provided by a permanent magnet mounted onto a piezo stage. Further, it is equipped with a magneto-optical Kerr effect module and a four-point resistance probe which enables for current injection and Hall effect measurements. The control software is written in python allowing for easy replacement of devices and installation. The instrument is designed for use under ambient conditions. In this chapter, the central components of the system are described. An overview of the key modules is given in Fig. 4.1. The magnetometer is capable of recording magnetic field maps with a spatial resolution of 50 nm and a sensitivity of  $< 1 \mu\text{T}/\sqrt{\text{Hz}}$ . Long-term drifts can be reduced to 50 nm per 24 h.*

---

The setup presented here was constructed and assembled by Pol Welter and myself with the help of Kevin Chang.

### 4.1 Quantum sensor tips

In this thesis, we exclusively use quantum sensor tips provided by QZabre LLC [119]. The tips are manufactured from high quality CVD diamond plates with a height between 0.8 – 3  $\mu\text{m}$  and an end diameter between 150 – 350 nm (see Fig. 4.2a,b). An optimised tip shape yields high saturation photon count rates between 0.3 – 1.2 MC/s. The NV centre is roughly located at  $\approx 10\text{nm}$  from the apex according to what the implantation energy predicts. The quantum sensor comes with an integrated tuning fork distance sensor and can be scanned using a standard atomic force microscopy controller. QZabre LLC provides the quantum sensor as a plug-and-play carrier chip solution.

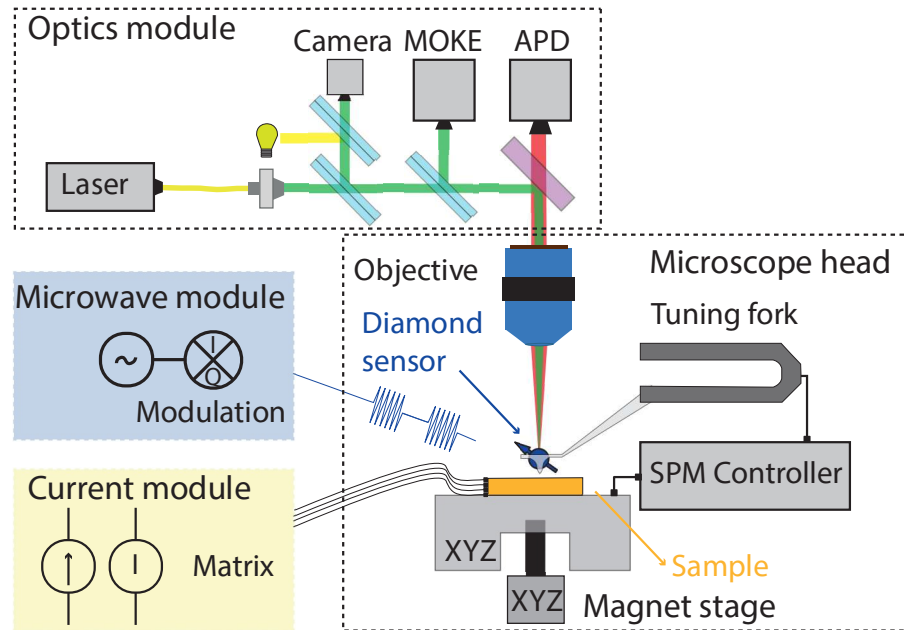


FIGURE 4.1: **Key modules of the NSDM instrument.** The NSDM instrument includes a scanning probe module incorporating the diamond NV sensor (microscope head), an optical fluorescence microscope for initialisation and readout of the sensor, a microwave module for manipulation of the magnetic spin of the sensor, and a magnet module for applying vector magnetic fields to the sample. The central box contains the actual microscope apparatus, the remaining components are peripheral instrumentation. The optics module also comprises a camera and MOKE setup. The current module provides means for current, longitudinal, and Hall resistance measurements. The instrument is mounted on a vibration-free optical table.

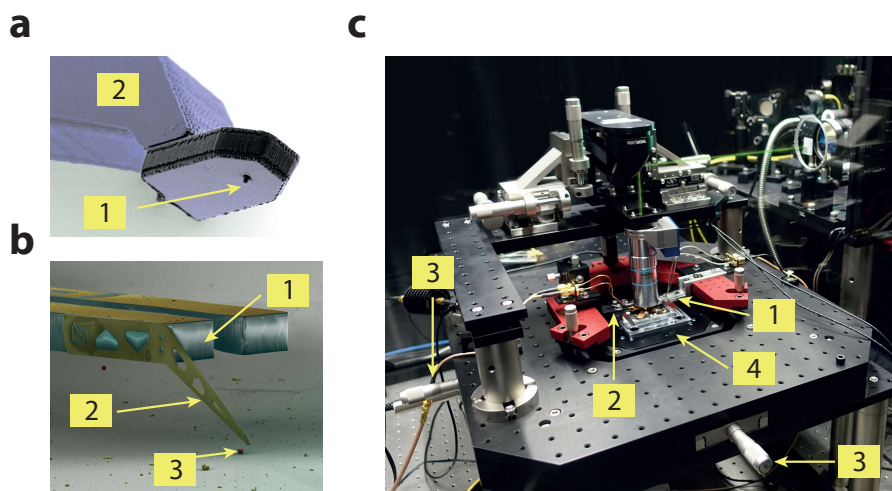


FIGURE 4.2: **Microscope head and sensor.** **a**, Image of the diamond plate with tip (1) attached to a silicon cantilever (2). The NV centre is implanted at the apex of the tip. **b**, The tuning fork based distance sensor is shown with the quartz tuning fork (1), silicon cantilever (2) and diamond tip (3). **c**, Photograph of the entire microscope head. The green excitation beam is focused from the top to the NV centre. The SPM (1) and microwave wire (2) are mounted on the red ring. The micrometer stages (3) allow for the coarse positioning of the sample. For fine positioning, a piezo stage (4) is used. a,b, courtesy of J. Rhensius, QZabre LLC.

## 4.2 Microscope head

The microscope head combines a SPM with a confocal fluorescence microscope. The SPM is used to navigate the diamond probe over the surface under study. The tuning-fork distance sensor operates in non-contact mode using amplitude modulation in a closed-loop feedback system. Here a current amplifier (Zurich Instrument, HF2TA) and lock-in amplifier with a built-in proportional-integral-derivative controller (PID-Controller, Zurich Instruments, HF2LI) for the distance control is employed. The instrument has a field-of-view of  $200\ \mu\text{m} \times 200\ \mu\text{m}$  with a horizontal resolution of  $\approx 1\ \text{nm}$ , a vertical resolution of  $\approx 0.2\ \text{nm}$  and a lateral drift well below  $50\ \text{nm}$  over 12 h at room temperature. The microscope head is equipped with a rapid sample exchange mechanism and an alignment camera. In Figure 4.2c a photograph of the microscope head is shown. The SPM (1) and microwave wire (2) are mounted on the red ring. Due to symmetry, a possible thermal drift of the SPM is therefore reduced. Micrometer stages (3) and the piezo stage (4) (PI, P-527.3CL) allow for coarse and fine positioning of the sample.

## 4.3 Optics module

The optics module combines a confocal fluorescence microscope with a 520 nm excitation channel ( $< 150\ \mu\text{W}$  at sample) and a 630 – 800 nm detection channel operated in single-photon counting mode. Excitation and detection can be gated and clocked at 40 ns by a laser diode and photon time-tagging electronics. The schematics of the optics are shown in Fig. 4.3.

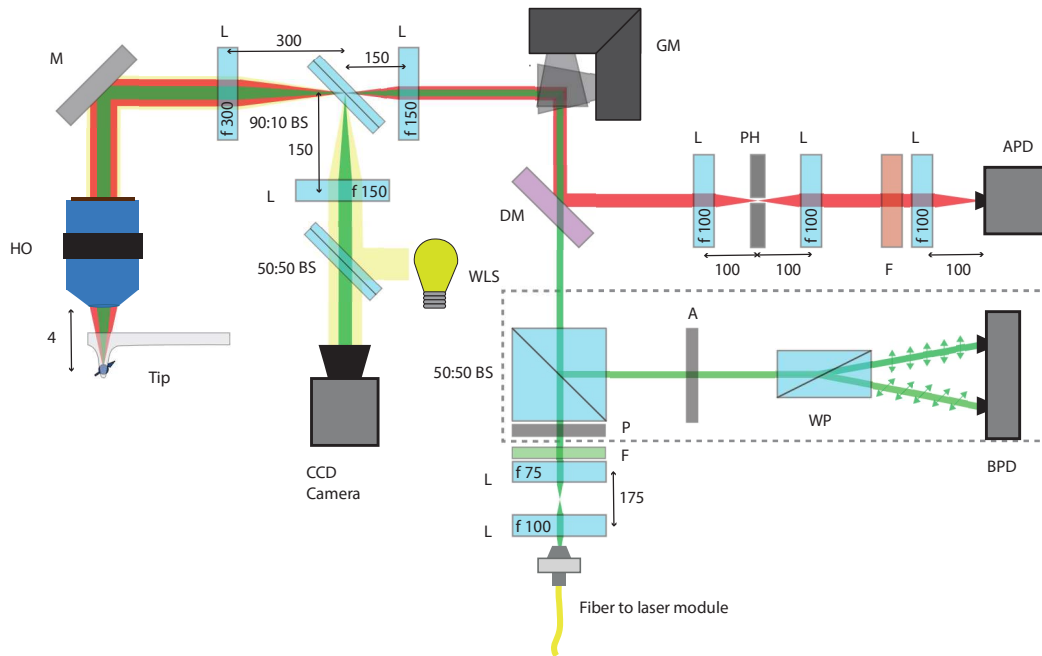


FIGURE 4.3: **Optics module.** The optics consist of four modules which are partially overlapping. The excitation path, indicated with green light, and detection path of the red shifted photons, shown in red, are essential for the NSDM. The setup is further equipped with an optical microscope, indicated by yellow, and a MOKE module, see dashed rectangle. Mirrors (M) and lenses (L) are denoted with capital letters. Details of each element are given in the text. Relevant distances and focal lengths, given in mm, are denoted in the schematics.

We use a custom-built nanosecond-resolution laser diode driver module [120] with wavelength  $\lambda = 520$  nm and typical rise times of 40 ns. The laser beam is transferred to the custom-built confocal microscope via a single-mode fibre (PAF-X-18-PC-B, Thorlabs), passing a Laser line filter (F, Thorlabs, FL532-10), and steered over the quantum sensor using a pair of galvanometric mirrors (GM, GVS012, Thorlabs). A high numerical-aperture ( $NA = 0.75$ ) objective (HO, Mitutoyo, Z04004316) focusses the beam onto the tip (NV centre). The focal plane is adjusted using a high-precision, piezo-electric actuator (Piezo Systems Jena, MIPOS-100). Red-shifted photons, emitted by the NV centre, are collected via the same path and separated from the excitation path using a dichroic mirror (DM, Thorlabs, DMLP550L) and are spatially filtered by a subsequent  $30 \mu\text{m}$  large pin-hole (PH). Finally, the remaining photons are spectrally filtered with a bandpass filter and long-pass filter (F, Thorlabs, FGL610M, FESH0950) resulting in a collective bandwidth of 630 – 800 nm and detected by an avalanche photodiode (APD, Perkin Elmer SPCM-AQR).

The setup is equipped with a wide-field camera (Thorlabs, CCD Camera) for coarse posing of the laser beam and sample. We use a white light source (WLS, Thorlabs) and a 90:10 beam splitter (BS) to illuminate the sample. The beam splitter is mounted on a flip mount and can be removed during the NV measurement to increase the photon count rate.

## 4.4 Magneto-optical Kerr microscopy

We further implemented a MOKE module. This module allows for directly measuring the magnetisation via the magneto-optical Kerr effect, using the exciting laser beam. It offers fast, yet diffraction-limited, access to the magnetisation which can be used to locate regions of interest, for example, domain walls. The Kerr effect can be measured while simultaneously recording the EPR spectra. As reconstructing a magnetic texture based on stray field measurements is an underconstrained inverse problem [121], a rough determination of the magnetisation using MOKE gives additional boundary conditions that provide the necessary constraints for the reconstruction. Given the confocal microscope and scanning stage, it can be easily implemented by initially polarising (P, B. Halle Nachfl. GmbH, PGT 1.08.05) the exciting laser beam. The reflected green light is then separated using a (50:50 BS, Thorlabs, BS016) and after passing an analyser (A, B. Halle Nachfl. GmbH, PGT 1.08.05) decomposed into its orthogonal polarisation states using a Wollaston prism (WP, B. Halle Nachfl. GmbH, PWK 20.10). The intensity of the orthogonal components are then detected by a balanced photo-detector (BPD, PDB210A/M, Thorlabs). This module can also be used to record a reflectivity map of the sample surface and enables a more precise positioning with respect to using the CCD camera.

The magneto-optical Kerr microscope ( $\lambda = 520\text{ nm}$ ) was tested on Pt/Co/AlO<sub>x</sub> stripes and the results were compared to an existing Kerr microscope in Prof. Gambardella's group ( $\lambda = 515\text{ nm}$ ), see Fig. 4.4. The small difference in wavelength for both setups as well as the weak spectral dependence of the polar Kerr rotation in Co [122] around  $\lambda = 520\text{ nm}$  justify this comparison. The stripe reveals regions, denoted as *Domain 1* and *Domain 2* in 4.4a, with different coercive fields which can be seen from the hysteresis loops in 4.4b. To estimate the sensitivity of the MOKE module a domain wall between both regions was nucleated in the following way. The magnetisation in both regions was first saturated by an external magnetic field. Then the external field was reversed and increased until the region with a smaller coercive field switched. To resolve the domain wall, a sensitivity of less than 0.5 mrad is necessary which can be seen from the hysteresis loops in Fig. 4.4b.

## 4.5 Microwave module and control/readout electronics

The measurement protocols require gated and clocked excitation and detection. To ensure proper synchronisation of all devices the 10 MHz reference clock of a frequency oscillator (LO, Quicksyn FSW-0020) is distributed to all peripheral devices. We employ an arbitrary waveform generator (AWG Zurich instruments, HDAWG4) and an IQ-mixer (Marki, IQ1545) in the single-sideband regime to control the microwave pulses we use to manipulate the electron spin of the NV centre. The IQ-mixer serves as a phase and amplitude modulator taking the two analog outputs of the AWG as the I and Q inputs. The AWG outputs are set to a carrier frequency of 100 MHz and up-converted to a signal at frequency 1 – 4 GHz with a low-phase-noise and tunable frequency oscillator (L0). The microwaves are delivered to the probe via a power amplifier (Mini-Circuits, ZHL-16W-43-S+) and a local antenna (Fig. 4.5). A digital output of the AWG gates the laser module. The incoming photons are detected by an APD and time-tagged using a data acquisition card (DAQ card, National Instruments, PCIe-6363). The signal generation and acquisition are triggered by the AWG. The remaining analog outputs of the AWG are used for current modulation when measuring the current distribution in a conductor. Time-tagging the incoming photons and synchronising all devices enables the



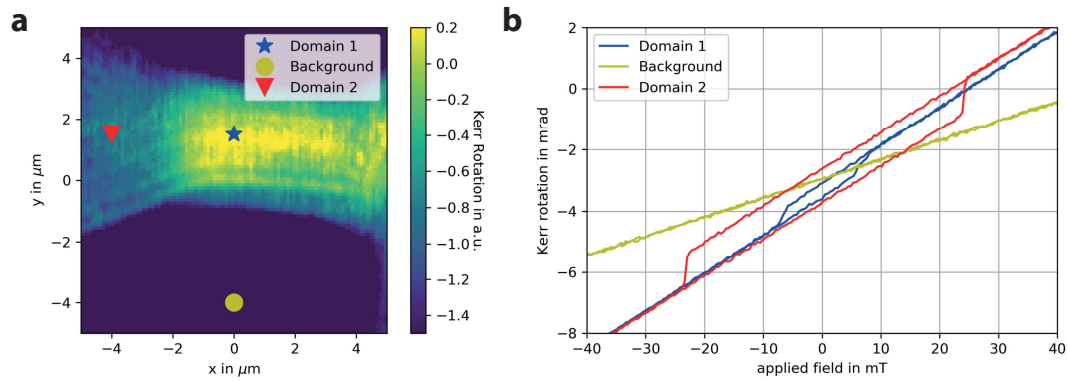


FIGURE 4.4: **Magneto-optical Kerr microscopy module.** **a**, MOKE image, taken with the NSDM setup on Pt/Co/ $\text{AlO}_x$ . *Domain* and *Contact Pad* are regions with different coercive field. **b**, Hysteresis loops were recorded on the domain, contact pad and next to the magnetic stripe with the existing Kerr microscope in Prof. Gambardella's group by Christoph Murer. The difference of the Kerr rotation in zero field is used to estimate the magnetic Kerr contrast between the *Domain* and the *Contact Pad* to estimate the minimal sensitivity of the new NSDM setup.

binning of photons to specific events, like laser excitation, readout, or evolution of the spin system during microwave application. The optics module is controlled by the DAQ card.

## 4.6 Magnetic field module

A permanent magnet (NdFeB) is mounted on a 3-axis translation stage and located below the sample to control the magnetic field at the sample location. The magnet is positioned by three stepping motor actuators (Newport, Conex-CC) with a closed-loop range of 25 mm and 1  $\mu\text{m}$  precision. Vertical fields of up to 150 mT and horizontal fields of  $\approx 150$  mT can be generated with this module.

## 4.7 Current source and switching matrix

In this thesis, we report experiments that require current, longitudinal, and Hall resistance measurements while simultaneously recording the magnetic stray fields using diamond magnetometry. To meet these requirements, we have implemented a 4-probe stage comprising of a source measure unit (SMU, Keithley, 2400), voltage-controlled current source (VCCS, Stanford Research Systems, CS580), and a home built signal-routing matrix. The latter one allows for quick altering of the measurement configuration. For instance, assuming a cross-shaped device with four contacts, Hall probe measurements can be conducted by sending a source current along one arm and sensing the voltage drop perpendicularly to it. Additionally, current pulses along each arm are feasible and offer a large variety of different current configurations. The current measurements are synchronised with the AWG and can be used to estimate the current density in a conductor by measuring its magnetic field using the diamond sensor.



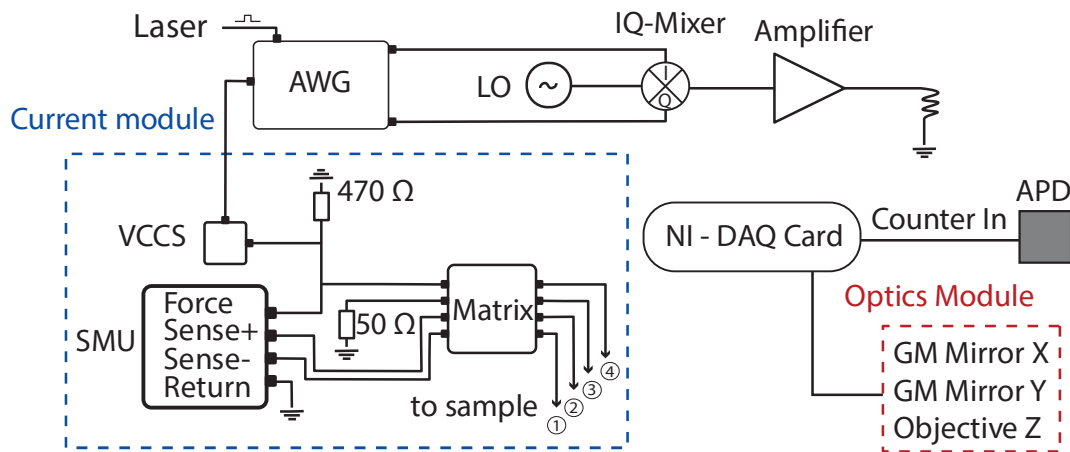


FIGURE 4.5: **Readout and control electronics.** a, An AWG combined with an IQ-mixer and low noise frequency oscillator are used to generate the microwave pulses. The microwaves are amplified and sent to a wirebond loop which serves as an antenna. One digital output of the AWG gates the laser module. The incoming photons are detected by the APD and time-tagged by the DAQ Card. The latter also controls the optics module, i.e. the galvanometric mirrors X and Y, and the piezo-electric actuator adjusting the focal plane. The current module consists of a VCCS which receives an arbitrary waveform from the AWG. A matrix (homebuilt) enables the measurement along different current directions. Additionally, a SMU is used to perform a four-point measurement. The  $470\ \Omega$  resistance protects the damaging of the sample from peak current densities. Details on each element are given in the text.



# Relations between magnetisation and magnetic field

## Summary

*This chapter elaborates on the generic question of what can be learned about the magnetisation from a measurement of the magnetic stray field above a thin film. We begin this chapter by describing how the magnetic stray field is related to the magnetisation. We then show that for certain antiferromagnetic systems a stray field can be expected. Last, we discuss the conditions required to unambiguously reconstruct the magnetisation from the magnetic stray field. We introduce relations to calculate the vector magnetic field from an arbitrary projection and distance.*

---

This chapter is mostly based on Ref. [123] and [117]. The Subsection 5.2.2 and 5.2.3 are adapted of the Supplementary Information from Ref. [35] and [36], respectively.

## 5.1 Magnetisation

### 5.1.1 Magnetostatic potential

The relations between magnetisation and magnetic field can be derived via the magnetic potential, as detailed in Beardsley [123]. The magnetostatic potential is given by

$$\phi(\vec{r}) = \frac{1}{4\pi} \iiint \frac{-\vec{\nabla} \cdot \vec{M}(\vec{r}')}{|\vec{r} - \vec{r}'|} d^3\vec{r}' \quad (5.1)$$

where  $\vec{r} = (x, y, z)$ . The magnetic field is then given by

$$\vec{B}(\vec{r}) = -\mu_0 \vec{\nabla} \phi(\vec{r}). \quad (5.2)$$

### 5.1.2 Basic equations for a two-dimensional thin magnetic film

We now focus on the case of a thin film of thickness  $d$  that extends in the  $xy$  plane from  $z = -d$  to  $z = 0$ . To continue, we transform the magnetostatic potential  $\phi(\vec{r})$

into Fourier space with respect to  $x$  and  $y$ . As derived in Eq. (6-10) of Ref. [124], the magnetostatic potential  $\phi(\vec{K}, z)$  above the film (for  $z > 0$ ) is

$$\phi(\vec{K}, z) = \left( -\frac{i\vec{K} \cdot \vec{M}_{||}}{K^2} + \frac{M_z}{K} \right) \sinh \frac{Kd}{2} e^{-K(z+d/2)} \quad (5.3)$$

where  $\vec{K} = (k_x, k_y)$  is the planar  $k$ -vector and  $K = \sqrt{k_x^2 + k_y^2}$ .  $\vec{M}_{||} = (M_x, M_y)$  is the in-plane magnetisation and  $M_z$  is the out-of-plane magnetisation. In the following, all fields and magnetisation maps are in  $k$ -space unless otherwise stated. The in-plane and out-of-plane components of the magnetic field are given by

$$\begin{aligned} \vec{B}_{||} &= -i\mu_0 \vec{K} \phi = \left( -\frac{\vec{K}(\vec{K} \cdot \vec{M}_{||})}{K^2} - \frac{i\vec{K}M_z}{K} \right) \eta \\ B_z &= \mu_0 \frac{\partial \phi}{\partial z} = \left( -\frac{i\vec{K} \cdot \vec{M}_{||}}{K} + M_z \right) \eta \end{aligned} \quad (5.4)$$

where we have introduced the decay function

$$\eta(K, z) = \mu_0 \sinh \frac{Kd}{2} e^{-K(z+d/2)}. \quad (5.5)$$

### 5.1.3 Decay function for ferromagnets

The decay function  $\eta$  can be recast as

$$\eta = \mu_0 \sinh \frac{Kd}{2} e^{-K(z+d/2)} \quad (5.6)$$

$$= \frac{1}{2} \mu_0 \left[ e^{+Kd/2} - e^{-Kd/2} \right] e^{-K(z+d/2)} \quad (5.7)$$

$$= \frac{1}{2} \mu_0 \left[ 1 - e^{-Kd} \right] e^{-Kz} \quad (5.8)$$

and for very thin films where  $d \ll z$  further simplified to

$$\eta \approx \frac{\mu_0 Kd}{2} e^{-Kz}. \quad (5.9)$$

We notice that the decay function has a maximum when  $Kz = 1$ . That is, the magnetic field at location  $z$  is maximised for magnetic features that have a length scale similar to the  $z$ -distance. The magnetic field of finer features decays too quickly ( $\propto e^{-Kz}$ ) while extended features of constant magnetisation produce a negligible magnetic field ( $\propto K$ ).

### 5.1.4 Decay function for antiferromagnets

One key feature praising magnetic storage devices employing antiferromagnetic systems is the vanishing magnetic stray field [1]. Here, we discuss the amplitude and decay of the magnetic stray field above the surface of a layered AFM. Antiferromagnetic ordering can formally often be constructed from ferromagnetic layers of opposite polarity. The result of net magnetisation is then typically given by a uniformly magnetised surface layer. For example, tetragonal CuMnAs or Cr<sub>2</sub>O<sub>3</sub> films consist of vertically alternating layers of opposite magnetisation. To calculate the

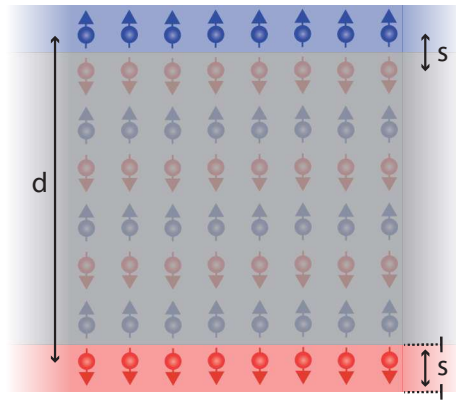


FIGURE 5.1: **Effective surface magnetisation in AFMs.** Arrows denote magnetic moments and describe the antiferromagnetic ordering. The alternating layers of opposite polarisation are assigned to two oppositely magnetised volumes (blue, red shading) which are vertically shifted with respect to each other by  $s$ . Within the bulk (gray shading) the magnetisation of the two volumes is exactly compensated, except in the two layers of thickness  $s$  at the top and bottom of the body. These uncompensated layers lead to an effective surface layer magnetisation  $\sigma = sM_s$ . In the case of very thick samples compared to the sensor-to-sample distance, i.e.  $d \gg z$ , only the topmost layer is contributing to the magnetic stray field.

stray field for layered AFMs, we decompose the magnetic body into two volumes (blue, red shading in Fig. 5.1) of opposite polarisation that are shifted with respect to each other. Specifically, we assume that the layers of opposite spin are vertically separated by a distance  $s$  (which is smaller than one unit cell height) and that each volume carries a magnetisation  $M_s = nm/V$ , where  $n$  are the number of spins per polarity per unit cell (i.e, one half the number of spins per cell),  $m$  is the magnetic moment per spin, and  $V$  is the unit cell volume. The magnetic stray field is then given by the difference of the stray fields from each volume,

$$B_j = B_j^{\text{spin up}} - B_j^{\text{spin down}} \quad (5.10)$$

$$= A_j [\eta(z) - \eta(z+s)] = A_j \eta(z) [1 - e^{-Ks}] := A_j \eta_{\text{AFM}}, \quad (5.11)$$

where

$$\eta_{\text{AFM}} = \frac{1}{2} \mu_0 K s [1 - e^{-Kd}] e^{-Kz} \quad (5.12)$$

for  $Ks \ll 1$ . Here,  $j = x, y, z$  refers to the component of magnetic field, the  $A_j$  summarize the geometric terms in Eq. (5.4) and  $\eta$  is taken from Eq. (5.8). The last expression indicates that the magnetic field of the entire film equals the sum of two magnetic sublayers of effective thickness  $s$  with opposite magnetisation, one located at the top  $z$  and one located at the bottom  $z + d$  of the film, (see blue, red shaded layer in Fig. 5.1). Within the bulk, the magnetisation of the two volumes compensate (see grey shading in Fig. 5.1). Simplified expressions can be given for the cases of

very thick ( $t \ll z$ ) and very thin ( $t \gg z$ ) films:

$$B_j^{\text{thick}} = A_j \frac{1}{2} \mu_0 K s e^{-Kz} \quad \text{for thick films} \quad (5.13a)$$

$$B_j^{\text{thin}} = A_j \frac{1}{2} \mu_0 K s e^{-Kz} K d = B_j^{\text{thick}} K d \quad \text{for thin films.} \quad (5.13b)$$

Thus, for thick films  $d \gg z$ , the magnetic field is simply given by two-dimensional surface layer of thickness  $s$ , with an effective surface magnetisation of  $M_s^{2D} = \sigma = sM_s = nms/V$ . An alternative way to derive the surface magnetisation is given in Ref. [125]. In that work, the author discusses the analogy of the surface charge arising from ferroelectric polarisation and the surface magnetic dipole moment arising from the magnetoelectric multipolarisation to estimate the surface magnetisation.

In the following, we refer to  $\eta_{\text{AFM}}$ ,  $\eta_{\text{FM}}$  when describing antiferromagnetic, ferromagnetic systems, respectively, and  $\eta$  when the system is not further specified.

### 5.1.5 Decomposition of the in-plane magnetisation

We have seen that, in principle, a non-vanishing magnetic stray field can be expected from antiferromagnetic materials. In the next step we analyse how the magnetic texture influences the magnetic stray field. The in-plane magnetisation  $\vec{M}_{\parallel}$  can be further decomposed into a “diverging” component  $\vec{M}_{\text{div}}$  that has no curl, and a “curly” component  $\vec{M}_{\text{rot}}$  that has no divergence,

$$\vec{M}_{\parallel} = \vec{M}_{\text{div}} + \vec{M}_{\text{rot}}. \quad (5.14)$$

By definition,

$$\begin{aligned} k_x M_{\text{div},y} - k_y M_{\text{div},x} &= 0 \\ k_x M_{\text{rot},x} + k_y M_{\text{rot},y} &= 0. \end{aligned} \quad (5.15)$$

The components are given by

$$\begin{aligned} \vec{M}_{\text{div}} &= \frac{\vec{K}(\vec{K} \cdot \vec{M}_{\parallel})}{K^2} \\ \vec{M}_{\text{rot}} &= -\frac{\vec{K} \times (\vec{K} \times \vec{M}_{\parallel})}{K^2} \end{aligned} \quad (5.16)$$

where in the second equation,  $\vec{K} = (k_x, k_y, 0)$  and  $\vec{M}_{\parallel} = (M_x, M_y, 0)$ . This is the Helmholtz theorem in two dimensions. According to the Helmholtz theorem, any in-plane field can be decomposed into  $\vec{M}_{\text{div}}$  and  $\vec{M}_{\text{rot}}$  and the decomposition is unique.

In a simple picture, the “curly” component corresponds to a magnetisation whose vector field lines are closed within the plane of the film, while the “diverging” component corresponds to field lines that connect sources and sinks in the film’s plane. Since the three-dimensional magnetic field is divergence-free (has no sources or sinks), the “diverging” component necessarily produces magnetic field lines that enter or exit the film and are thus detectable outside of the film.

By entering the two components into Eq. (5.4), we see that only the diverging component  $\vec{M}_{\text{div}}$  contributes to the magnetic field outside of the film and that the

contribution by the curly component is zero. This means that by measuring a magnetic stray field, we cannot uniquely determine the magnetisation of a film. Only the diverging part of the magnetisation plus the  $M_z$  component can be determined.

We can rewrite Eq. (5.4) assuming that  $\vec{M}_{||}$  is curl-free. Under this assumption  $\vec{K}(\vec{K} \cdot \vec{M}_{\text{div}}) = K^2 \vec{M}_{\text{div}}$ , and the in-plane component of the magnetic field becomes (the out-of-plane component is unchanged)

$$\vec{B}_{||} = \left( -\vec{M}_{\text{div}} - \frac{i\vec{K}M_z}{K} \right) \eta. \quad (5.17)$$

For later use we rewrite Eq. (5.4) in components,

$$\begin{aligned} B_x &= \left( -M_{\text{div},x} - i\frac{k_x}{K}M_z \right) \eta \\ B_y &= \left( -M_{\text{div},y} - i\frac{k_y}{K}M_z \right) \eta \\ B_z &= \left( -i\frac{k_x}{K}M_{\text{div},x} - i\frac{k_y}{K}M_{\text{div},y} + M_z \right) \eta. \end{aligned} \quad (5.18)$$

## 5.2 Reconstruction of the magnetisation

To reconstruct the magnetisation, we need to disentangle the contributions of  $M_z$ ,  $\vec{M}_{\text{div}}$ , and  $\vec{M}_{\text{rot}}$  to the magnetic stray field. Because  $\vec{M}_{\text{rot}}$  does not produce any stray field, we cannot reconstruct the magnetisation in a general case. However, it is still possible to recover the magnetisation (or some aspects of it) in a more specific situation, for example, when the magnetisation is entirely out-of-plane or if there are additional constraints on the magnetisation (such as that the magnitude  $|\vec{M}|$  is constant over the film). We now discuss a few basic cases.

### 5.2.1 Out-of-plane magnetisation

Assuming that the in-plane magnetisation is zero,  $M_x = M_y = 0$ , Eq. (5.4) simplifies to

$$\begin{aligned} B_x &= i\frac{k_x}{K}M_z\eta \\ B_y &= i\frac{k_y}{K}M_z\eta \\ B_z &= M_z\eta. \end{aligned} \quad (5.19)$$

The field measured by an NV center oriented along the unit vector  $\vec{e} = (e_x, e_y, e_z) = (\sin \theta_{\text{NV}} \cos \phi_{\text{NV}}, \sin \theta_{\text{NV}} \sin \phi_{\text{NV}}, \cos \theta_{\text{NV}})$  is

$$B_{\text{NV}} = \vec{e} \cdot \vec{B} = \frac{M_z\eta (ik_x e_x + ik_y e_y + K e_z)}{K}. \quad (5.20)$$

The reconstructed magnetisation is

$$M_z = \frac{KB_{\text{NV}}}{\eta(ik_x e_x + ik_y e_y + K e_z)}. \quad (5.21)$$

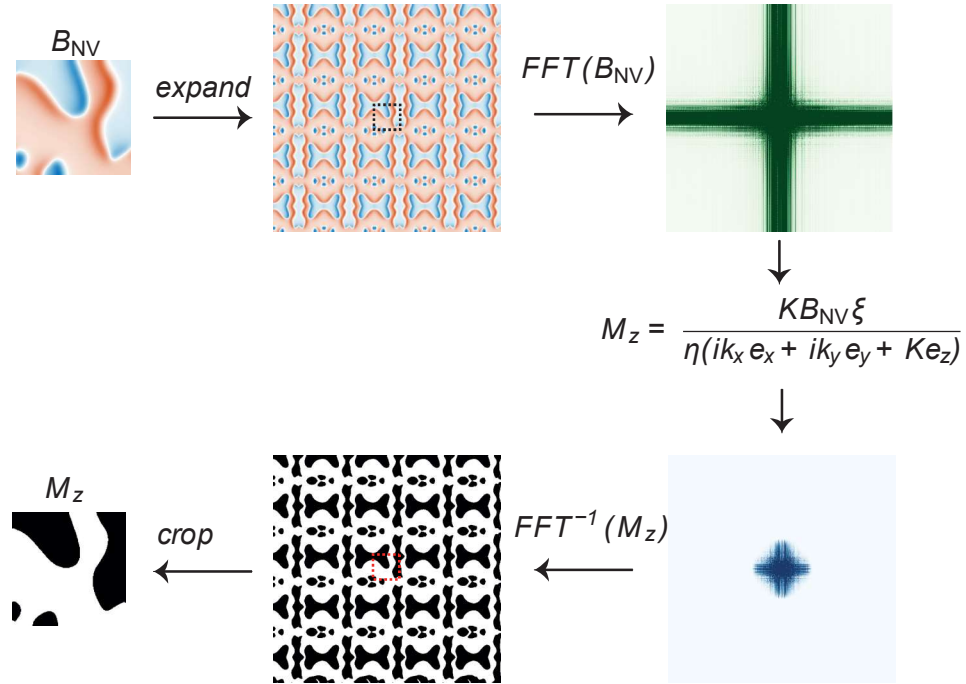


FIGURE 5.2: **Reconstruction of  $M_z$ .** First, the stray field map  $B_{NV}$  is expanded by multiple reflection at the boundaries. The unit cell is indicated by a dashed rectangular. This improves the subsequent Fourier transformation ( $FFT$ ) and reduces reconstruction artefacts at the boundaries of the field map. In a next step, we introduce a suitable window function  $\xi = \xi(k)$  that provides a high-frequency cutoff, when applying Eq. (5.21). Finally, we perform the inverse Fourier transformation ( $FFT^{-1}$ ) on the reconstructed  $M_z$  map and crop the image to the size of the initial field map.

In Fig. 5.2 we illustrate the reconstruction steps when applying Eq. (5.21).



### 5.2.2 In-plane magnetisation

Assuming that the out-of-plane magnetisation is zero,  $M_z = 0$ , we can reconstruct the in-plane magnetisation, but only the diverging part  $\vec{M}_{\text{div}}$ . Therefore, we start with Eq. (5.18) and set  $M_z = 0$

$$\begin{aligned} B_x &= -M_{\text{div},x}\eta \\ B_y &= -M_{\text{div},y}\eta \\ B_z &= \left( i\frac{k_x}{K}M_{\text{div},x} + i\frac{k_y}{K}M_{\text{div},y} \right) \eta. \end{aligned} \quad (5.22)$$

The field measured by an NV center is

$$B_{\text{NV}} = \vec{e} \cdot \vec{B} = M_{\text{div},x}\eta \left( -e_x + i\frac{k_x}{K}e_z \right) + M_{\text{div},y}\eta \left( -e_y + i\frac{k_y}{K}e_z \right). \quad (5.23)$$

Solving for  $\vec{M}_{\parallel}$  yields

$$\vec{M}_{\text{div}} = \frac{-i\vec{K}B_{\text{NV}}}{\eta(ik_x e_x + ik_y e_y + Ke_z)}. \quad (5.24)$$

To also reconstruct the curly part  $\vec{M}_{\text{rot}}$  and recover the full in-plane magnetisation vector  $\vec{M} = \vec{M}_{\text{div}} + \vec{M}_{\text{rot}}$ , further information is required.

#### Recipe for reconstructing the in-plane magnetisation for a single domain orientation

As above, there is no unique correspondence between the stray field  $\vec{B}(x, y, z)$  and the in-plane magnetisation pattern  $\vec{M}_{\parallel}(x, y)$ . However, a best estimate for  $\vec{M}_{\parallel}(x, y)$  can be found (i) if the vector length is constant,  $|\vec{M}_{\parallel}(x, y)| = M_s$ , and (ii) if the magnetic system is uniaxial with a single domain orientation (e.g.,  $\vec{M}_{\parallel} \parallel \pm x$ ). For example, both assumptions are expected to be valid for  $t < 50\text{nm}$  films in tetragonal CuMnAs.

In the Subsection 5.1.5, we have seen that only the diverging component  $\vec{M}_{\text{div}}$  produces a stray field because the field lines of the curly component  $\vec{M}_{\text{rot}}$  are closed within the magnetised volume. Moreover, the correspondence between  $\vec{M}_{\text{div}}$  and  $\vec{B}$  is unique. When attempting to reconstruct  $\vec{M}_{\parallel}(x, y)$  from a measured field map  $\vec{B}(x, y, z)$ , we therefore recover the diverging part  $\vec{M}_{\text{div}}$ , but not the full magnetisation  $\vec{M}_{\parallel} = \vec{M}_{\text{div}} + \vec{M}_{\text{rot}}$ . We now show that under the assumptions (i) and (ii) given above,  $\vec{M}_{\text{rot}}$  can also be recovered and a best estimate for  $\vec{M}_{\parallel}$  can be made.

We develop the following recipe to calculate the in-plane magnetisation.

1. Calculate the diverging component  $\vec{M}_{\text{div}}$  by using Eq. (5.24):

$$\vec{M}_{\text{div}}(k_x, k_y) = \frac{-i\vec{K}B_{\text{NV}}(k_x, k_y, z)}{\eta(ik_x e_x + ik_y e_y + Ke_z)}. \quad (5.25)$$

2. Rotate  $\vec{M}'_{\text{div}} = \mathcal{R}(\alpha) \vec{M}_{\text{div}}$  by the angle  $\alpha$  such that the  $x$  component of  $\vec{M}'_{\text{div}}$  is parallel to the domain orientation, and the  $y$  component is perpendicular to the domain orientation. The correct  $\alpha$  will be determined below by a least-squares minimisation.

3. Set  $M'_{\text{rot},y} = -M'_{\text{div},y}$ , because  $M'_y = 0$ .
4. Set  $M'_{\text{rot},x} = -\left(k'_y/k'_x\right) M'_{\text{rot},y}$  because of Eq. (5.15). Note that the  $k$ -vectors also need to be rotated, using the same rotation matrix as described in step 2,  $\vec{K}' = \mathcal{R}(\alpha)\vec{K}$ . We apply a bandpass filter to avoid division by zero and amplification of high frequency noise. A useful way is to set  $M'_{\text{rot},x} = -k'_y / (k'_x + [\text{sign } k'_x] k_{\text{min}}) M'_{\text{rot},y}$ , where  $k_{\text{min}}$  is a small number, and applying a Hann window to suppress high  $k'_y$ .
5. Rotate the vector back to obtain  $\vec{M}_{\text{rot}} = \mathcal{R}(-\alpha) \vec{M}'_{\text{rot}}$ .
6. Calculate the full in-plane magnetisation  $\vec{M} \equiv (M_x, M_y) = (M_{\text{div},x} + M_{\text{rot},x}, M_{\text{div},y} + M_{\text{rot},y})$ . Compute the real-space  $\vec{M}(x, y)$  from  $\vec{M}(k_x, k_y)$ . Note that  $\vec{M}(x, y)$  is not uniform in space because of the filtering applied in steps 1 and 4.
7. Optionally, rescale  $\vec{M}_{\parallel}(x, y) \rightarrow M_s \vec{M}_{\parallel}(x, y) / |\vec{M}_{\parallel}(x, y)|$  by an arbitrary  $M_s$ . The best guess for  $M_s$  will be determined below using a least-squares minimisation. Calculate the magnetic field map  $B_{\text{NV}}^{\text{calc}}$  predicted by this  $\vec{M}_{\parallel}$  and the error variance  $\varepsilon = \text{var}(B_{\text{NV}} - B_{\text{NV}}^{\text{calc}})$ .

We determine the most likely  $\alpha$  by iterating over steps 2-6 for  $\alpha = 0 - 2\pi$  and minimising the variance  $\text{var}|\vec{M}_{\parallel}|$ . The associated magnetisation is then given by  $M_s = \text{mean}|\vec{M}_{\parallel}|$ . Alternatively, we iterate over steps 2-7 for  $\alpha = 0 - 2\pi$  and various  $M_s$  values and minimise the error variance  $\varepsilon$  of step 7, yielding the most likely  $(\alpha, M_s)$  pair.

### 5.2.3 Extract magnetisation from line scan

An important task is to extract the change in  $z$  magnetisation across a domain wall or step edge in an out-of-plane magnetised film. This allows us to estimate the saturation magnetisation of a ferromagnet or the surface saturation magnetisation of a layered antiferromagnet. As shown in the following, it is possible to extract the magnetisation change from a line scan, provided the line scan extends far enough into regions of homogeneous magnetisation (and zero field). Let a domain wall extend along the  $y$ -direction. Then, the magnetisation change simply is the integral of  $B_x$  along the line scan irrespective of the sample-to-sensor distance  $z$  and the domain-wall profile and chirality.

Assume an out-of-plane magnetised film with magnetisation  $\vec{M}(x')$  and a step edge or domain wall along  $y$ . The step edge can have an  $M_x$  or  $M_y$  component. The magnetic field  $B_x$  produced at the position  $x$  by the magnetisation element  $dx' \vec{M}(x')$  at the position  $x'$  is

$$dB(x) = \frac{\mu_0 j_y(x') dx' z d}{2\pi [(x - x')^2 + z^2]} \quad (5.26)$$

where  $j_y(x') = [\vec{\nabla} \times \vec{M}]_y(x') = -[\partial_x M_z](x')$  is the bound current element associated with  $\vec{M}(x')$  and  $d$  is the film thickness ( $d \ll z$ ). Note that field and magnetisation maps are in real space for the entire subsection. The total magnetic field at position

$x$  is

$$B(x) = \int_{-\infty}^{\infty} dx' \frac{\mu_0 j_y(x') z d}{2\pi[(x-x')^2 + z^2]} = - \int_{-\infty}^{\infty} dx' \frac{\mu_0 z d}{2\pi[(x-x')^2 + z^2]} [\partial_x M_z](x') \quad (5.27)$$

and the integrated  $B(x)$  is

$$\int_{-\infty}^{\infty} dx B(x) = - \left( \int_{-\infty}^{\infty} dx'' \frac{\mu_0 z d}{2\pi[(x'')^2 + z^2]} \right) \left( \int_{-\infty}^{\infty} dx' [\partial_x M_z](x') \right) \quad (5.28)$$

$$= - \frac{\mu_0 d}{2} [M_z(+\infty) - M_z(-\infty)] = \mu_0 M_s d. \quad (5.29)$$

where we have used Fubini's theorem  $[\int f * g = (\int f)(\int g)]$  and the last equation is for a domain wall where  $[M_z(+\infty) - M_z(-\infty)] = -2M_s$ . Importantly, the  $M_x$  component does not contribute to the integral (because the field produced by  $M_x$  integrates to zero from  $-\infty$  to  $\infty$ ), hence the integral is insensitive to the chirality of the domain wall.

### 5.3 Vector magnetic field from an arbitrary projection and distance

In this section, we show that the vector magnetic field can be reconstructed from an arbitrary projection on the NV axis. In principle, this is not required to reconstruct the magnetisation, as Eqs. 5.21 and 5.25 already take into account the projection on the NV axis. However, it is useful for the extraction of the magnetisation from a line scan, see Subsection 5.2.3. In the next step we explain how the magnetic field for a given distance  $z$  can be directly calculated for any  $z$  without calculating a magnetisation or current density.

#### 5.3.1 Reconstruction of the vector magnetic field from an arbitrary projection

By using the fact that the magnetic field above the plane of magnetisation is source free, we can compute all three components of the magnetic field vector  $\vec{B} = (B_x, B_y, B_z)$  from a *single* projection  $B_{\text{NV}} = \vec{e} \cdot \vec{B}$  of the field vector. Starting with  $\vec{\nabla} \times \vec{B} = 0$  for  $|z| > d/2$  we obtain in real space

$$\begin{aligned} \partial_x B_y &= \partial_y B_x \\ \partial_x B_z &= \partial_z B_x \\ \partial_y B_z &= \partial_z B_y, \end{aligned} \quad (5.30)$$

and in Fourier space

$$\begin{aligned} ik_x B_y &= ik_y B_x \\ ik_x B_z &= k B_x \\ ik_y B_z &= k B_y, \end{aligned} \quad (5.31)$$

using the magnetic gradient in Fourier space

$$\begin{aligned}\partial_x \vec{B} &= -ik_x \vec{B} \\ \partial_y \vec{B} &= -ik_y \vec{B} \\ \partial_z \vec{B} &= -K\vec{B}.\end{aligned}\tag{5.32}$$

The projection is then given by

$$B_{NV} = e_x B_x + e_y B_y + e_z B_z \tag{5.33}$$

$$= e_x B_x + e_y \frac{k_y}{k_x} B_x - ie_z \frac{K}{k_x} B_x \tag{5.34}$$

where we have used the relations of Eq. (5.31). Solving the equation for  $B_x$  we find

$$B_x = \frac{ik_x B_{NV}}{ie_x k_x + ie_y k_y + e_z K} \tag{5.35}$$

Likewise, we find for  $B_y$  and  $B_z$

$$B_y = \frac{ik_y B_{NV}}{ie_x k_x + ie_y k_y + e_z K} \tag{5.36}$$

$$B_z = \frac{KB_{NV}}{ie_x k_x + ie_y k_y + e_z K}.\tag{5.37}$$

### 5.3.2 Calculation of magnetic field for arbitrary distance $z$

Assuming that we know the magnetic field  $\vec{B}(\vec{K}, z_0)$  at a fixed distance  $z_0$  from the two-dimensional magnetic layer (or current distribution), we can directly calculate  $\vec{B}(\vec{K}, z)$  for any  $z$  without calculating a magnetisation or current density. From Eq. (5.4) we see that the only term that depends on  $z$  is the decay function  $\eta(\vec{K}, z)$ . For the decay function, we obtain in the ferromagnetic case

$$\eta(K, z) = \eta(K, z_0 + \Delta z) = \mu_0 \sinh \frac{Kd}{2} e^{-Kz_0} e^{-K\Delta z} = \eta(\vec{K}, z_0) e^{-K\Delta z} \tag{5.38}$$

where  $\Delta z = z - z_0$  is the relative height difference between the planes at  $z$  and  $z_0$ . Combining this with Eq. (5.17) we find

$$\vec{B}(K, z) = \vec{B}(K, z_0) e^{-K\Delta z}.\tag{5.39}$$

Note that Eq. (5.39) is also valid for antiferromagnetic systems.

# High-speed domain wall racetracks in a magnetic insulator

## Summary

*Recent reports of current-induced switching of ferrimagnetic oxides coupled to a heavy metal layer have opened realistic prospects for implementing magnetic insulators into electrically addressable spintronic devices. However, key aspects such as the configuration and dynamics of magnetic domain walls driven by electrical currents in insulating oxides remain unexplored. Here, we investigate the internal structure of the domain walls in  $Tm_3Fe_5O_{12}$  (TmIG) and TmIG/Pt bilayers. Scanning nitrogen-vacancy magnetometry reveals that the domain walls of thin TmIG thin films grown on  $Gd_3Sc_2Ga_3O_{12}$  are Néel walls with left-handed Néel chirality, changing to an intermediate Néel-Bloch configuration upon Pt deposition. These results indicate the presence of interfacial Dzyaloshinskii-Moriya interaction in magnetic garnets, opening the possibility to stabilise chiral spin textures in centrosymmetric magnetic insulators.*

---

This chapter is based on parts of the publication "High-speed domain wall racetracks in a magnetic insulator" (Ref. [39]). S. Vélez fabricated the TmIG/Pt devices and performed and analysed the electrical measurements. S. Vélez, J. Schaab and M. Müller performed the MOKE measurements and S. Vélez and J. Schaab analysed the data. M. Müller, C. Gutgsell and C. Nistor built the wide-field MOKE setup. P. Welter, C. L. Degen and myself built the scanning NV magnetometer and performed and analysed the scanning NV measurements. M. Trassin, M. Fiebig, C. L. Degen and P. Gambardella supervised the work. I co-wrote the NSDM related parts of the paper. S. Vélez and P. Gambardella wrote the manuscript. All authors contributed to the scientific discussion and manuscript revision.

## 6.1 Introduction

Spintronics employs current-induced torques to manipulate the magnetisation of nano-devices [126]. Typically, heavy metals such as Pt, Ta or W are used to convert a charge current into a spin-polarised current. The spin current, having a non-zero angular momentum, is injected into an adjacent ferromagnetic layer exerting a torque on the magnetisation [91, 127]. These so-called spin-orbit torques (SOT) are capable

of driving domain walls [128, 129] or reversing the magnetisation in a very efficient manner [130]. Most studies in that field have been performed on ultrathin metallic ferromagnets [25, 131–133].

However, magnetic insulators, in particular ferrimagnetic rare-earth garnets coupled to a heavy metal layer, also provide an exciting perspective for spintronic applications [134–136]. Ferrimagnetic garnets have attracted attention, among others, for their low-power and high frequency magnetisation dynamics [137]. Current induced switching has been demonstrated in  $\text{Tm}_3\text{Fe}_5\text{O}_{12}$  (TmIG) and  $\text{BaFe}_{12}\text{O}_{19}$  coupled either to a Pt or W layer [138–140]. However, the dynamics of the switching process remain unexplored.

In this work, we present a combined NSDM and spatially-resolved MOKE study of the domain wall structure and dynamics driven by SOTs in racetrack structures embedded in a TmIG layer. We further provide the first direct characterisation of the domain wall width and internal structure in thin-film TmIG as well as TmIG/Pt bilayers. Previous studies in garnets were only able to provide estimates of the domain wall width based on indirect or diffraction-limited optical measurements, with reported values ranging from tens of nanometers to micrometers [42, 141–143]. Scanning NV magnetometry reveals that the domain walls in TmIG films are only  $\sim 20$  nm wide and have a well-defined chiral structure, which changes from left Néel in TmIG to intermediate left Néel-Bloch in TmIG/Pt. Given that the crystal structure of TmIG is centrosymmetric, these findings evidence the presence of strong interfacial DMI in TmIG grown on substituted gadolinium gallium garnet  $\text{Gd}_3\text{Sc}_2\text{Ga}_3\text{O}_{12}$  (SGGG), which is attenuated by the deposition of Pt. The DMI is the key ingredient required to stabilise chiral Néel domain walls in ferromagnets and ferrimagnets with perpendicular magnetisation, which can then be driven by SOTs at very high velocities [144, 145]. Our measurements reveal robust domain wall velocities of up to  $\sim 200$  ms for domain expansion and  $\sim 400$  ms for domain contraction, which are comparable to the ones found in all-metallic structures under similar conditions [128, 132, 144, 146]. Most remarkably, however, the domain wall mobility  $\mu_{\text{DW}} = v_{\text{DW}}/J_x$ , where  $v_{\text{DW}}$  is the domain wall velocity and  $J_x$  the applied current density, reaches values in excess of  $3 \times 10^{-10} \text{ m}^3 \text{ A}^{-1} \text{ s}$  for  $J_x = 5 \times 10^7 \text{ A cm}^{-1}$ , which is comparable to that observed in compensated metallic ferrimagnets [144, 147]. In contrast, most metallic ferromagnets feature  $\mu_{\text{DW}} = 0$  in this current range [128, 132, 145, 146]. Our results show that ferrimagnetic garnets are ideal materials for fabricating efficient and high-speed domain wall racetracks.

## 6.2 Ferrimagnetic garnet $\text{Tm}_3\text{Fe}_5\text{O}_{12}$ (TmIG)

The TmIG(8nm)/Pt(5nm) bilayer samples are grown on SGGG (111)-oriented substrates. The numbers between parentheses denote the thickness of each layer. The Pt current lines are patterned by optical lithography and consecutive etching of the metal (see Fig. 6.1). For details about the sample growth and fabrication, we refer to Ref. [48]. The films exhibit robust perpendicular magnetic anisotropy with a coercive field of about 40 Oe, i.e. the magnetisation points out-of-plane.

## 6.3 Domain wall structure and chirality in TmIG and TmIG/Pt

We use NSDM to reveal the domain wall magnetisation profile in both TmIG and TmIG/Pt layers by sensing the magnetic stray field  $B_{\text{NV}}(X, Y)$  emanating from a magnetic surface (Fig. 6.2a). Details on the measurement are given in appendix B.1.

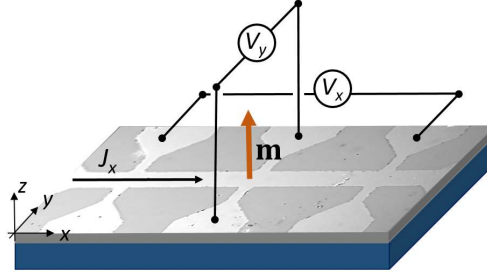


FIGURE 6.1: **Device schematic of TmIG** . Optical image of a Pt Hall bar patterned on TmIG with superposed electric wiring, coordinate system and magnetisation vector  $\mathbf{m}$ .

Figure 6.2b shows  $B_{\text{NV}}(X, Y)$  of the TmIG film measured in a region where a domain wall intersects an area partially covered by Pt. From this measurement, we reconstruct the out-of-plane component of the surface magnetisation  $M_Z(X, Y)t$  (see Appendix B.2), as shown in Fig. 6.2c. Although the domain wall runs continuously across the Pt edge, the linescans of  $B_{\text{NV}}(X, Y)$  shown in Fig. 6.2d and 6.2e reveal that the domain wall structure changes going from TmIG/Pt to TmIG. In order to extract the magnetisation profile of the domain wall from these measurements, we fit  $B_{\text{NV}}(X, Y)$  by assuming that the magnetisation components vary as [25, 42]

$$M_X(X) = M_s \frac{\cos \psi}{\cosh\left(\frac{X-X_0}{\Delta_{\text{DW}}}\right)}, \quad (6.1a)$$

$$M_Y(X) = M_s \frac{\sin \psi}{\cosh\left(\frac{X-X_0}{\Delta_{\text{DW}}}\right)}, \quad (6.1b)$$

$$M_Z(X) = -M_s \tanh\left(\frac{X-X_0}{\Delta_{\text{DW}}}\right), \quad (6.1c)$$

where  $\psi$  defines the angle of the in-plane magnetisation direction with respect to the  $X$ -axis,  $\Delta_{\text{DW}}$  is the domain wall width, and  $M_s$  the saturation magnetisation. In a first step, we fitted line cuts across the TmIG to TmIG/Pt step edge to extract the NV centre stand-off distance,  $z = (104 \pm 5)$  nm (see appendix B.3). To characterise the chirality and width of the domain wall we took line cuts of  $B_{\text{NV}}$  perpendicular to the domain wall as shown in Fig. 6.2b and compared them to the analytical model given by Eq. (6.1). The associated magnetic stray field was obtained by forward propagation of Eq. (6.1) in  $k$ -space according to the relations introduced in Eq. (5.4). The film thickness  $d$  is taken to be 8.3 and 7.3 nm for the TmIG/Pt and TmIG regions, respectively (see supplementary Notes 2 in Ref. [48] for topographic characterisation of the films). To extract values for  $M_s$ ,  $\chi$  and  $\Delta_{\text{DW}}$  we fitted the experimentally measured  $B_{\text{NV}}$  to the analytical prediction by Eqs. 6.1, with the domain wall position  $X = X_0$  as an additional fit parameter. By repeating the fitting procedure for a series of line scans, we obtained distributions for all parameters together with their means and standard deviations. A detailed description of the fitting procedure and error analysis is given in Appendix B.4. Note that we can infer  $\Delta_{\text{DW}}$  values that are below the NV-to-sample distance due to the large signal-to-noise ratio in our experiments and because the stray field extends far beyond the nominal domain wall width (see Eq. (6.1)). Figures 6.2d and 6.2e compare representative  $B_{\text{NV}}(X, Y)$  line profiles



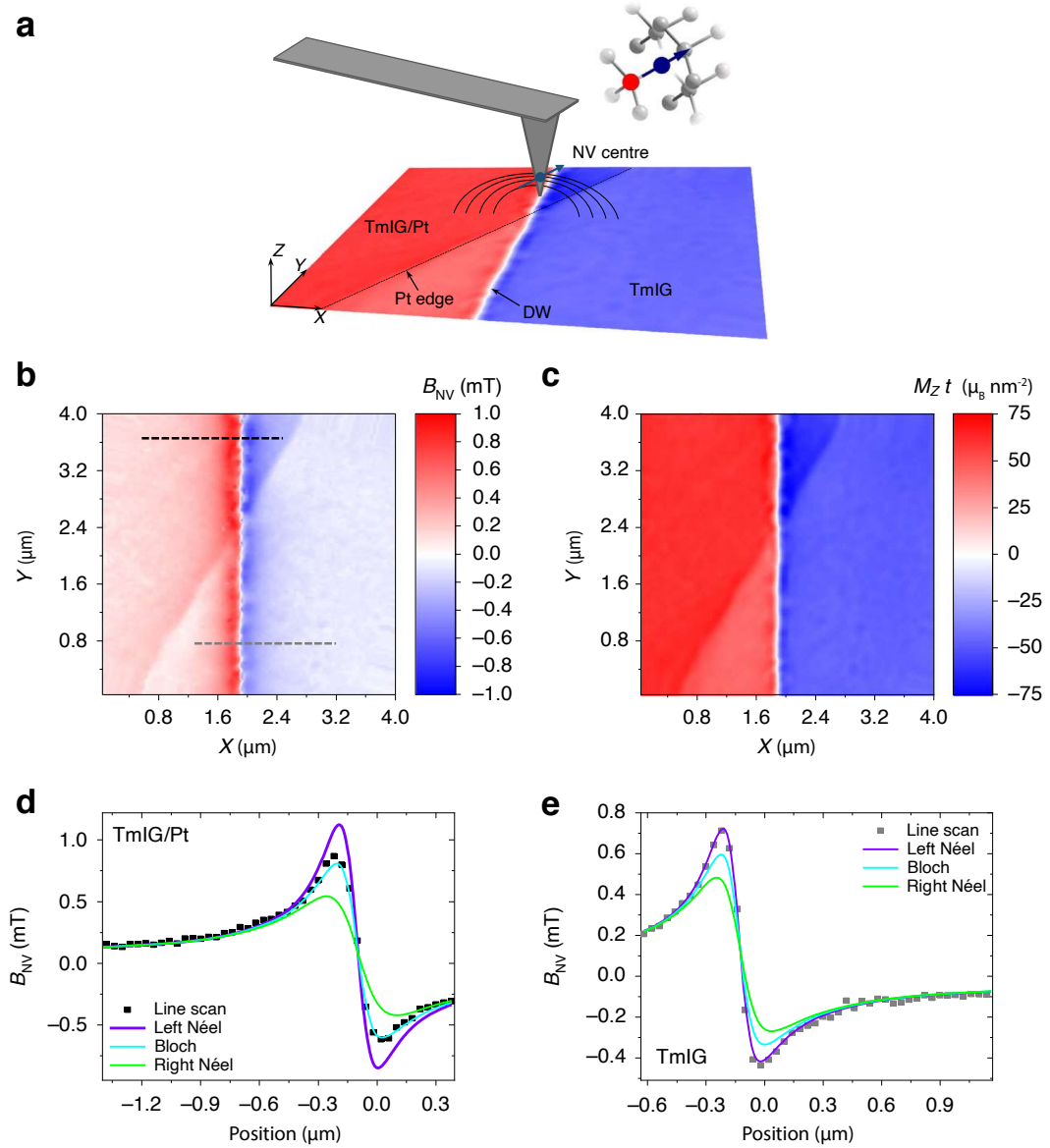


FIGURE 6.2: **Domain wall structure and chirality in TmIG and TmIG/Pt measured by NSDM.** **a**, Schematic of the NV probe and sample. The color code represents the out-of-plane component of the surface magnetisation of the film, with red (blue) corresponding to areas of opposite magnetisation. A domain wall crosses the TmIG/Pt and TmIG regions. The inset shows a NV centre within the diamond lattice and the corresponding spin quantisation axis. **b**, Stray field  $B_{NV}(X, Y)$  measured by scanning the diamond tip over the sample surface shown in a. **c**, Reconstructed out-of-plane magnetic surface map  $M_Z(X, Y)t$  from the data shown in b, where  $t$  is the thickness of the TmIG layer (see appendix B.2) and  $\mu_B$  the Bohr magneton. The difference in the measured surface magnetisation  $M_Z t = (66.8 \pm 1.5) \mu_B/\text{nm}^2$  in TmIG/Pt and  $M_Z t = (39.5 \pm 2.2) \mu_B/\text{nm}^2$  in TmIG is attributed to both the etching process and to proximity-induced polarization of the Pt layer (see main text). **d, e** Line scans of  $B_{NV}$  along the dashed lines indicated in b (square dots). The solid lines are calculated  $B_{NV}$  profiles using Eq. (6.1) assuming pure Bloch ( $\psi = 90^\circ$ , cyan), left-handed Néel ( $\psi = 180^\circ$ , violet), and right-handed Néel ( $\psi = 0^\circ$ , green) domain wall structures for comparison with the measured stray field profiles.  $M_s t$  and  $\Delta_{DW}$  are set from the fits of the  $B_{NV}(X, Y)$  map. The fits give  $\psi = (116 \pm 33)^\circ$  and  $\Delta_{DW} = (17 \pm 17)$  nm for Tm<sub>3</sub>Fe<sub>5</sub>O<sub>12</sub>/Pt and  $\psi = (173 \pm 17)^\circ$  and  $\Delta_{DW} = (26 \pm 6)$  nm for TmIG.



for TmIG/Pt and TmIG together with the stray field profile of a pure Bloch wall ( $\psi = 90^\circ$ ), a left Néel wall ( $\psi = 180^\circ$ ), and a right Néel wall ( $\psi = 0^\circ$ ). The best fits of the  $B_{\text{NV}}(X, Y)$  line profiles give  $\psi = (116 \pm 33)^\circ$  and  $\psi = (173 \pm 17)^\circ$ , corresponding to an intermediate left-handed Néel-Bloch wall for TmIG/Pt and a left-handed Néel wall for TmIG, respectively. The domain wall widths are  $\Delta_{\text{DW}} = (17 \pm 17)$  nm and  $\Delta_{\text{DW}} = (26 \pm 6)$  nm for TmIG/Pt and TmIG, respectively. Despite the large uncertainty in  $\Delta_{\text{DW}}$ , which is due to the weak dependence of  $B_{\text{NV}}$  on  $\Delta_{\text{DW}}$ , and which prevents us to determine the relative change of domain wall width between TmIG/Pt and TmIG, the fits show that the domain walls in 8-nm-thick TmIG are very narrow. Measurements performed in a reference unetched TmIG layer of the same thickness showed that  $\psi = 180^\circ$  and  $\Delta_{\text{DW}} = (20 \pm 4)$  nm (see appendix B.5), which confirms the left-handed Néel chirality and the narrow width of the domain walls in thin TmIG films grown on SGGG. The change of the domain wall chirality from left-handed Néel to an intermediate left-handed Néel-Bloch configuration in going from TmIG to TmIG/Pt is a compelling indication of the presence of negative DMI in the bare TmIG layer, most likely due to symmetry breaking at the SGGG/TmIG interface. The deposition of Pt reduces the DMI, which we ascribe to the presence of positive DMI at the TmIG/Pt interface, consistently with the sign of the DMI found in metallic ferromagnetic/Pt bilayers [25, 132, 146]. These findings have important consequences for the operation of domain wall racetracks in magnetic insulators, because the reduced  $\Delta_{\text{DW}}$  favours the localisation of domain walls, whereas the finite DMI allows for their efficient manipulation by spin-orbit torques.

## 6.4 Domain wall dynamics

The chiral structure of the domain wall is supported by a complementary study of the domain wall dynamics driven by SOTs. We use spatially resolved MOKE to capture the displacement of the domain wall upon injection of current pulses (see Fig. 6.3a). In agreement with a previous report [138], the magnetisation of TmIG can be deterministically switched upon the application of a current pulse of sufficient current density  $J_x$  in the presence of a constant in-plane field  $H_x$ . The switching occurs by domain wall nucleation and consecutive propagation of the domain wall. The switching polarity is determined by the damping-like component of the SOT [127, 130, 148], which stabilises  $+\mathbf{m}$  for  $J_x$  parallel to  $H_x$  and  $-\mathbf{m}$  for  $J_x$  antiparallel to  $H_x$  in TmIG/Pt. Notably, we found that full switching can be achieved with pulses of 1 ms at current densities below  $1 \times 10^7$  A/cm<sup>2</sup> for an in-plane field as small as  $|H_x| = 20$  Oe, which confirms the high quality of our devices (see also Supplementary Section Note S3 in Ref. [39]). The domain wall speed  $v_{\text{DW}}$  can be estimated by the displacement  $\Delta x$  of the domain wall and the number of applied current pulses  $N_p$  of duration  $t_p$  according to  $v_{\text{DW}} = \Delta x / (N_p t_p)$ . A systematic study of the  $v_{\text{DW}}$ , by analysing the displacement  $\Delta x$  for different  $t_p$  but constant  $N_p t_p$ , allows us to conclude that the domain wall speed is accurately evaluated upon changing  $t_p$  and not influenced by domain wall inertia (see Fig. 6.3b,c). We observe a slightly larger  $v_{\text{DW}}$  when the domain wall moves against the direction of the current (see Fig. 6.4f). The same behaviour is also confirmed for down-up domain walls (see Fig. 6.4g). This asymmetry, which is characteristic of chiral Néel domain walls [132, 146], is consistent with the partially left-handed Néel chirality and the sign of the torques in TmIG/Pt as detailed in Fig. 6.4a-e and in agreement with the NSDM measurement. Provided that the dynamics of the domain walls is restricted to the flow regime, we can estimate the effective internal DMI field of the domain walls by

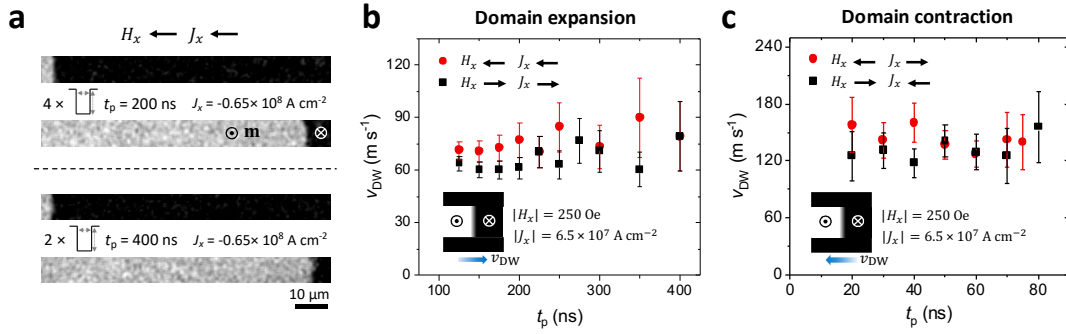
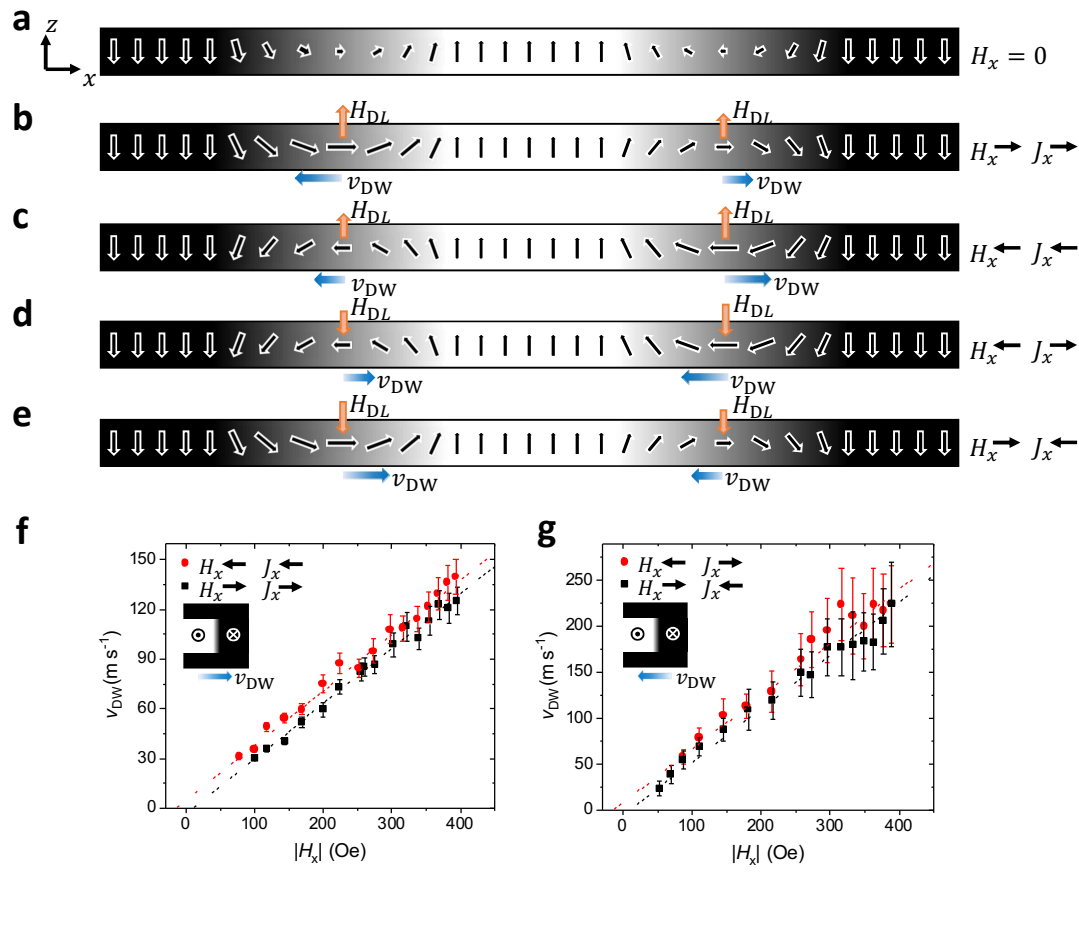


FIGURE 6.3: **Spatially-resolved MOKE-dependence of  $v_{DW}$ .** **a**, Differential MOKE images showing the displacement of an up-down domain wall after the application of  $N = 4$  current pulses of  $t_p = 200$  ns and  $N = 2$  pulses of  $t_p = 400$  ns. We apply an in-plane magnetic field of strength  $H_x = -250$  Oe and current pulse of amplitude  $J_x = -6.5 \times 10^7$  A/cm<sup>2</sup> along the  $x$ -direction in both cases. The same displacement  $\Delta x$  is observed for both sequences of current pulses, leading to the same estimate for the domain wall speed  $v_{DW} = \Delta x / (N_p t_p)$ . **b**, Systematic evaluation of  $v_{DW}$  for an up-down domain wall during domain expansion as a function of  $t_p$  in the regime where domain walls move upon the application of current pulses but are not strongly influenced by Joule heating. **c**, Same as b for domain contraction. Within the experimental error,  $v_{DW}$  remains roughly constant although  $t_p$  changes by a factor of 4, which allows us to conclude that the domain wall speed is accurately evaluated upon changing  $t_p$  and not influenced by domain wall inertia. The error bars in b and c indicate the uncertainty in estimating  $v_{DW}$  from the domain wall displacement obtained for a sequence of current pulses.

fitting  $v_{DW}(H_x)$  to a linear function and extrapolating it to  $v_{DW} = 0$  (see Ref. [146]). The fit yields  $|H_{DMI}| \sim 12 \pm 3$  Oe (see Fig. 6.4f,g), which allows us to calculate the effective DMI constant as [128, 132]  $D = \mu_0 H_{DMI} M_s \Delta_{DW} \sim -2 \pm 2$   $\mu\text{J}/\text{m}^2$ , where we have taken  $M_s = (6.0 \pm 1.0) \times 10^4$  A m<sup>-1</sup> and  $\Delta_{DW} \sim 20$  nm. Alternatively, the DMI constant can be estimated from the DW chirality using the equation  $\cos \psi = D/D_c$ , where  $D_c = 2\mu_0 M_s^2 t \ln 2 / \pi^2$  (see Refs. [149] and [150]). This estimate gives  $D \sim -2.3 \pm 2.6$   $\mu\text{J}/\text{m}^2$ , in good agreement with the value obtained from the analysis of the domain wall velocity.

## 6.5 Saturation magnetisation

The NV-related results are further supported by comparing the saturation magnetisation  $M_s$  extracted from the NSDM measurements to those recorded using a commercial SQUID magnetometer. For calculating  $M_s$  from the SQUID measurements, we assume that the effective TmIG thickness of the TmIG sample is reduced by about 1 nm to 7.3 nm after the etching of the Pt due to partial etching (as evidenced by atomic force microscopy, see Supplementary Information of Ref. [48]) and likely passivation of the top surface of the TmIG layer, as suggested by the comparison of the SQUID data taken for the reference TmIG(8.5 nm) film before and after exposure to the Ar-plasma (see Fig. 6.5a), and between the measured  $M_s$  of the pristine reference TmIG film and the TmIG/Pt sample after etching. For the reference TmIG(8.5 nm) film, the surface was exposed to the Ar-plasma in order to reproduce the exposure time of the TmIG surface of the TmIG(8.3 nm)/Pt(5.0 nm) sample during the etching of the Pt layer. The exposure time was set according to the calibrated



**FIGURE 6.4: Schematics of the domain wall structure and current-induced domain wall motion in the presence of  $H_x$  and DMI.** **a**, Cross-sectional schematics ( $x - z$ -plane) of a down-up and an up-down domain wall (positioned along the  $y$ -direction) in TmIG/Pt illustrating its internal structure in the absence of  $H_x$ . The finite left-handed Néel chirality of the domain walls reflects the negative DMI found in TmIG/Pt. **b-e**, The internal magnetisation of the domain walls can be controlled by applying a magnetic field  $H_x$  exceeding the effective DMI field  $H_{DMI}$ , where the latter is positive (negative) for a down-up (up-down) domain wall (see a). Consequently, upon the application of  $H_x$ , the internal magnetisation of up-down and down-up domain walls has either a larger or smaller projection on the direction of  $J_x$ . As the amplitude of the damping-like SOT is maximal when the domain wall magnetisation is parallel or antiparallel to  $J_x$ , up-down and down-up DWs move at different speed. The damping-like SOT is represented by the corresponding effective field  $H_{DL}$  in the figure. Application of current pulses drives the DWs as indicated for all four possible combinations of  $H_x$  and  $J_x$  applied (see b-e). Domain walls are driven at larger (smaller) velocities when moving against (towards)  $J_x$ . **f**,  $v_{DW}$  of an up-down domain wall as a function of  $H_x$  upon expansion and **g** contraction. The current density is fixed at  $J_x = 0.75 \times 10^8$  A/cm<sup>2</sup> in either case. Domain walls move faster when  $J_x$  is opposite to (red symbols), indicating the presence of a weak DMI favoring left-handed Néel chiral domain walls. Dashed lines in either f and g are linear fits to the experimental data assuming the same slope of for both polarities of and opposite magnetic field at which crosses zero, which allows evaluating the effective DMI field  $|H_{DMI}| \sim 12 \pm 3$  Oe (for details see Ref. [146] and [39]).

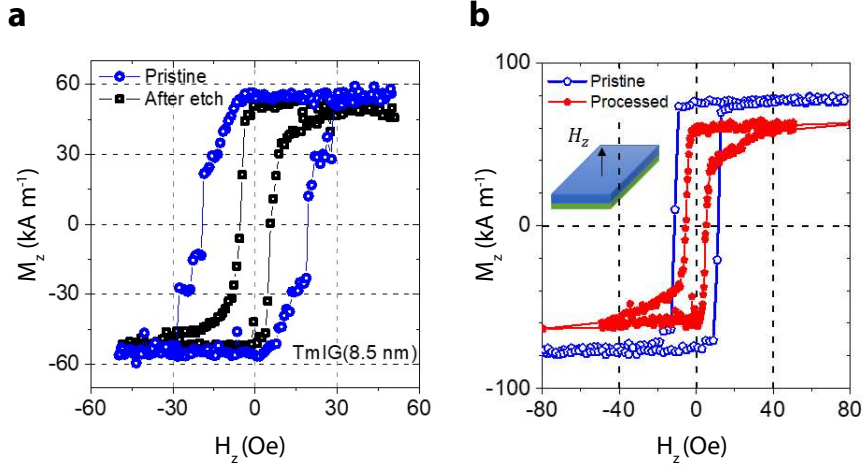


FIGURE 6.5: **SQUID magnetometry of the TmIG samples.** **a**, Magnetic characterisation of the TmIG(8.5 nm) reference film. Out-of-plane SQUID measurements performed in the film before (blue) and after exposure of the surface to the Ar-plasma (black), which reproduces the exposure of the TmIG surface to the Ar-plasma in the TmIG(8.3 nm)/Pt(5.0 nm) sample during the etching of the Pt layer. For calculating  $M_Z$ , we considered that the effective thickness of the TmIG layer has been reduced to 7.5 nm after exposure of the surface to the Ar-plasma due to both etching and surface passivation. **b**, Magnetic characterisation of the TmIG(8.3 nm)/Pt(5.0 nm) sample. Out-of-plane SQUID measurements performed before (blue) and after (red) patterning of the Pt layer. For calculating  $M_Z$ , we considered that the effective thickness of the TmIG layer is 7.3 nm after etching.

etching rate of Pt determined using Pt reference films.

By assuming a 1 nm reduction of the TmIG thickness, the SQUID measurements indicate that the saturation magnetisation is  $M_s = 55 \pm 2 \text{ kAm}^{-1}$  and  $M_s = 52 \pm 3 \text{ kAm}^{-1}$  in the reference TmIG film before and after the Ar-plasma exposure (see Fig. 6.5a), respectively and that  $M_s = 59 \pm 2 \text{ kAm}^{-1}$  in the TmIG/Pt sample after etching (see Fig. 6.5b). Note that some portion of the film surface is still covered with Pt after etching, which explains the slightly larger  $M_s$  measured for the TmIG/Pt sample (see also the NSDM data described in Section 6.3). The saturation magnetisation in TmIG/Pt is larger than in TmIG (red curve, see Fig. 6.5b). From the SQUID measurements, we find that in TmIG/Pt the saturation magnetisation is  $M_s = 77 \pm 2 \text{ kAm}^{-1}$ , which corresponds to a difference in  $M_s$  of  $\sim 20 \text{ kAm}^{-1}$  with respect to TmIG. This difference is likely to be due to a partial polarisation of the Pt atoms in proximity with TmIG. By assuming that the first three atomic layers of Pt in contact with TmIG get polarised, we estimate that this difference is equivalent to a magnetic moment per Pt atom of about  $0.4 \mu_B$ .

We compare the SQUID and NSDM measurement by dividing the surface magnetisation  $M_Z t$ , extracted from the NSDM measurement, of the TmIG/Pt sample after etching (see Fig. 6.2) by  $t = 8.3 \text{ nm}$  and  $t = 7.3 \text{ nm}$  for the TmIG/Pt and TmIG regions, respectively, we obtain  $M_s = 75 \pm 2 \text{ kAm}^{-1}$  and  $M_s = 50 \pm 3 \text{ kAm}^{-1}$ . Regarding the reference sample, the surface magnetisation measured by NSDM before the exposure of the surface to the Ar-plasma was  $M_Z t = (48.9 \pm 3.2) \mu_B/\text{nm}^2$ , which corresponds to  $M_s = 53 \pm 4 \text{ kAm}^{-1}$  (see also appendix B.5). We find that the magnetisation estimated by SQUID magnetometry and NSDM agree well for the TmIG and TmIG/Pt samples.

## 6.6 Conclusion

Our results reveal the internal structure of magnetic domains in thin garnet layers. The chiral Néel domain walls in TmIG indicate that oxide interfaces support a finite DMI even in the absence of heavy metal layers, which makes it possible, in principle, to stabilise nontrivial topological configurations in centrosymmetric insulating magnetic thin films, such as spin spirals and skyrmions. The good agreement of the NSDM related results with the aforementioned complementary measurement techniques demonstrate NSDM as a powerful technique to investigate the domain wall texture and magnetisation properties.

In the next chapter we will extend and improve the analysis of domain walls and surface magnetisation using NSDM from FM [25] and FIM [48] to AFM [36].



# Co-existence of Bloch and Néel walls in a collinear antiferromagnet

## Summary

*We resolve the domain-wall structure of the model antiferromagnet  $\text{Cr}_2\text{O}_3$  using nanoscale scanning diamond magnetometry and second-harmonic-generation microscopy. We find that the  $180^\circ$  domain walls are predominantly Bloch-like, and can co-exist with Néel walls in crystals with significant in-plane anisotropy. In the latter case, Néel walls that run perpendicular to a magnetic easy axis acquire a well-defined chirality. We further report quantitative measurement of the domain-wall width and surface magnetisation. Our results provide fundamental input and an experimental methodology for the understanding of domain walls in pure, intrinsic antiferromagnets, which is relevant to achieve electrical control of domain-wall motion in antiferromagnetic compounds.*

---

This chapter is based on the publication “Co-existence of Bloch and Néel walls in a collinear antiferromagnet” (Ref. [36]). I initiated the project, which was supervised by C. L. Degen, M. Fiebig and P. Gambardella. I performed the NSDM measurements. C. L. Degen and I analysed the data with the help of P. Welter and P. Gambardella. M. Fiebig, P. Gambardella, C. L. Degen and myself co-wrote the paper. All SHG images were recorded by M. Giraldo.

## 7.1 Introduction

The domain wall that separates regions with different orientations of the magnetic order parameter and influences the thermal stability [151], exchange bias [152], and magnetoresistance [35, 153] of antiferromagnets. Furthermore, the type of domain wall, Bloch or Néel, determines their response to current-induced spin torques [17, 154–156], which is of relevance for emerging applications of antiferromagnets in spintronics [91, 157, 158].

Unlike for ferromagnets [159], the internal structure of the domain walls in antiferromagnets is not generally known. Whereas the antiferromagnetic domain pattern has been imaged for a number of materials including intrinsic antiferromagnets, multiferroics, and magnetically-coupled thin films [16, 75, 160], these studies generally do not consider the detailed internal domain wall structure. Exceptions include



a few systems where antiferromagnetic order is accompanied by strain [19] or defects [20] as well as monolayer-thin films [18]. By contrast, studies for bulk, intrinsic antiferromagnets still need to be reported. Theoretical analysis suggests that, in the absence of in-plane magnetic anisotropy or a Dzyaloshinskii-Moriya interaction (DMI), no preference is expressed for either Bloch or Néel walls [55–58, 161]. The limited experimental knowledge about antiferromagnetic domain walls is due to a lack of techniques capable of spatially resolving the internal wall structure.

In this work, we use nanoscale scanning diamond magnetometry (NSDM) to investigate the spin structure of the pure intrinsic antiferromagnet  $\text{Cr}_2\text{O}_3$ . NSDM microscopy is an emerging quantum technique for the imaging of weak magnetic fields with nanometer spatial resolution (Fig. 7.1), with remarkable progress on antiferromagnets [35, 76, 162], multiferroics [34], and helimagnets [32]. Here, we extend NSDM to the imaging of antiferromagnetic  $180^\circ$  domain-wall structures. We obtain quantitative information about the domain-wall width, chirality, and surface magnetisation, and connect it to a model of interplaying demagnetising and anisotropy energies. We find that both Bloch and Néel walls can be present. Our work extends the knowledge about antiferromagnetic domain wall structure to the most basic class of intrinsic, bulk antiferromagnets.

## 7.2 One-dimensional model of antiferromagnetic domain walls

In order to motivate and explain our experimental observations, we refer to Section 2.3 for a brief review on antiferromagnetic domain walls. For a layered antiferromagnet like  $\text{Cr}_2\text{O}_3$ , it is convenient to express the domain wall profile, described in Eq. (2.10) in terms of the intrinsic surface magnetisation  $\vec{\sigma}(x)$ :

$$\sigma_x(x) = \sigma_z^0 \left[ \cosh \left( \frac{x - x_0}{\Delta_{\text{DW}}} \right) \right]^{-1} \cos \chi, \quad (7.1a)$$

$$\sigma_y(x) = \sigma_z^0 \left[ \cosh \left( \frac{x - x_0}{\Delta_{\text{DW}}} \right) \right]^{-1} \sin \chi, \quad (7.1b)$$

$$\sigma_z(x) = \sigma_z^0 \tanh \left( \frac{x - x_0}{\Delta_{\text{DW}}} \right), \quad (7.1c)$$

In Section 2.3 we have seen that the DMI can further lead to a preference for Néel-type domain walls when the Dzyaloshinskii vector runs parallel to the domain wall direction (the  $y$ -axis, Fig. 2.2) [55, 56, 61]. Although the DMI is zero in bulk monodomain  $\text{Cr}_2\text{O}_3$  for symmetry reasons [43], the formation of two magnetic domains with an order parameter along  $\pm z$  breaks the inversion symmetry between two adjacent spins along  $x$ . Such a symmetry breaking might allow for a finite DMI or higher-order chiral interactions to emerge in the proximity of the domain walls in  $\text{Cr}_2\text{O}_3$ . If such local chiral interactions are larger than or comparable to the demagnetising energy, the domain walls will be of either Néel or intermediate Bloch-Néel-type with a unique chirality. The results presented in our study provide experimental support to this hypothesis.

## 7.3 Materials and methods

We investigate the domain wall structure and chirality in the prototypical  $180^\circ$  antiferromagnet  $\text{Cr}_2\text{O}_3$ .  $\text{Cr}_2\text{O}_3$  is an antiferromagnetic insulator consisting of a hexagonal close packed array of  $\text{O}^{2-}$  anions with  $2/3$  of the octahedral holes occupied by



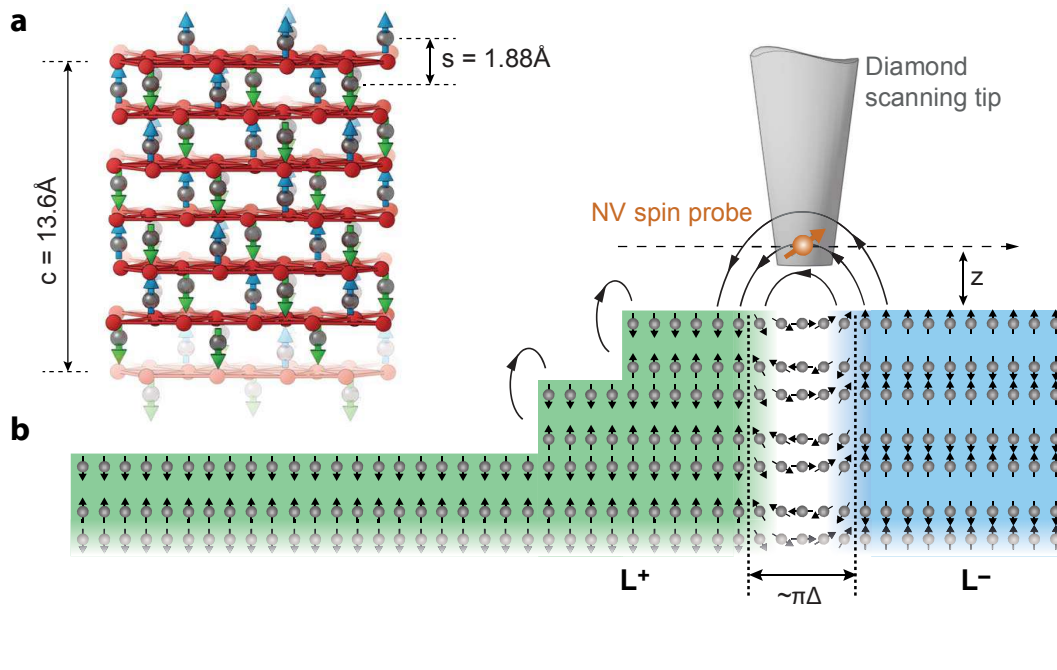


FIGURE 7.1: **Cr<sub>2</sub>O<sub>3</sub> crystal structure and experimental arrangement.** **a**, Side view of the hexagonal unit cell. Blue and green arrows symbolise Cr<sup>3+</sup> moments of opposite magnetic polarisation, and red atoms are O<sup>2-</sup> ions. **b**, Lateral cut through the *c*-oriented Cr<sub>2</sub>O<sub>3</sub> sample surface. Strong magnetic stray fields (black field lines) are expected at antiferromagnetic domain walls and weak fields at monolayer topographic steps. Blue and green shading indicate regions of opposite order parameter  $L^+$  and  $L^-$ , defined by the orientation (up or down) of the topmost Cr<sup>3+</sup> atom in the unit cell [163]. The regions are separated by a domain wall (white) of approximate width  $\pi\Delta_{\text{DW}}$ . The diamond scanning tip and NV centre are shown in grey and orange, respectively. To map the stray field distribution, we scan a spin probe – a NV centre in a diamond tip (orange arrow) – at constant height ( $z = 60 - 70$  nm) above the sample surface. The spin probe detects the component of magnetic field  $B_{\text{NV}}$  parallel to its internal anisotropy axis (here,  $55^\circ$  off the surface normal, see Appendix C.1.3). Experiments are performed under ambient conditions using a custom-built NSDM microscope.

Cr<sup>3+</sup> [163] (Fig. 7.1a). Below  $T_{\text{N}} = 307.6$  K, Cr<sub>2</sub>O<sub>3</sub> forms an antiferromagnetically ordered phase, where the Cr<sup>3+</sup> ions organise in alternating layers of opposite magnetic polarisation (green and blue spins in Fig. 7.1a). Because of its fundamental role in antiferromagnetism, Cr<sub>2</sub>O<sub>3</sub> has served as a model system for uniaxial antiferromagnetic order [43, 164, 165], magnetoelectric coupling [166–168], and electrically controlled exchange bias [169, 170]. More recently, Cr<sub>2</sub>O<sub>3</sub> has attracted attention as a candidate material for antiferromagnetic magnetoelectric random access memories [162], spin colossal magnetoresistance [171], and as a generator of sub-THz spin currents [172]. Although the domain wall plays a critical role in many of these phenomena, the spin structure is unknown beyond initial theoretical work [173], presenting an important experimental test case.

We investigate the Cr<sub>2</sub>O<sub>3</sub> domain texture of three bulk single crystals. Samples A and B are grown by the Verneuil method and polished to a surface roughness of 1 – 3 nm-rms. Sample C is a flux-grown platelet with an as-grown surface. In a previous study [174], we found that the spin-flop transition – normally requiring a magnetic field of 5.8 T (Ref. [163]) – occurs spontaneously at 150 K in sample C, pointing to an unusually strong in-plane anisotropy on top of the dominating out-of-plane anisotropy. In addition, this sample has a lower Néel temperature ( $T_{\text{N}} = 304.6$  K),

probably due to strain or oxygen deficiency. We create antiferromagnetic domains by repeatedly cooling samples through the transition temperature  $T_N$  using magnetoelectric poling [175] or until a multi-domain state spontaneously forms. Further details about the samples are given in Appendix C.1.1.

We use a combination of optical second-harmonic generation (SHG) microscopy and NSDM to locate the antiferromagnetic domains and measure the domain wall profile. SHG is a non-linear optical method capable of resolving the global  $180^\circ$  domain pattern, yet has a diffraction-limited spatial resolution and is not sensitive to the absolute sign of the order parameter [71]. For more details about the SHG measurement, we refer to the Appendix C.1.2. To map the stray field distribution, we scan a diamond tip with a NV-centre (orange arrow), at a constant height ( $z = 60 - 70$  nm) above the sample surface (Fig. 7.1b). The NV spin detects the component of the stray magnetic field  $B_{NV}$  parallel to its internal anisotropy axis (here,  $55^\circ$  off the surface normal). The experiments are performed under ambient conditions at a temperature of 295 K. Details on the NSDM measurements are given in Appendix C.1.3.

## 7.4 Experimental results

### 7.4.1 Domain states

Figure 7.2(a) shows a laser-optical second-harmonic-generation (SHG) [174] micrograph of the global domain pattern. We observe that the domains in the bulk  $\text{Cr}_2\text{O}_3$  crystals are large, typically in the range of hundreds of micrometers, and stable below  $T_N$ , in agreement with earlier studies [71]. We find no correlation between the domain pattern and the in-plane crystal axes (Fig. 7.2a), indicating that the domain-wall location is set by the local defect or strain distribution or is completely random.

Once the domains are localised, we acquire high-resolution magnetic imaging scans along the domain walls using NSDM microscopy (Fig. 7.2b). The domain wall appears as a narrow track of a strong magnetic stray field in the magnetometry image; this strong field is due to the  $180^\circ$  reversal of uncompensated moments near the sample surface (see Fig. 7.1b). Fainter features within the domains reflect residual stray fields associated with surface topography [77]. We do not observe any correlation between the domain wall location and the sample structure, suggesting that there are no surface-induced pinning effects. Further, when cycling the sample through the transition temperature  $T_N$ , domain walls usually form in random locations of the sample with no correlation between consecutive warming-cooling cycles.

To retrieve the absolute sign of the order parameter we reconstruct (see Appendix C.2.2) the two-dimensional (2D) surface magnetisation  $\sigma_z$  from the stray field map of Fig. 7.2b, shown in panel c. Here, a positive sign of  $\sigma_z$  (dark contrast) reflects a positive  $\text{Cr}^{3+}$  surface magnetisation and order parameter  $L^-$  (vice versa for  $L^+$ ). We find that the correlation between SHG contrast and surface magnetisation is maintained for all domain walls on all samples with different surface roughness (Appendix C.1.1, Figs. C.1 and C.2 in Appendix C). Combined with the absence of strong magnetic features in the interior of domains, these findings directly confirm that the magnetic polarisation of  $\text{Cr}_2\text{O}_3$  is robust against surface roughness [76, 170], and that  $\text{Cr}_2\text{O}_3$  always terminates with the same  $\text{Cr}^{3+}$  surface magnetisation for a given sign of the order parameter  $L$ .

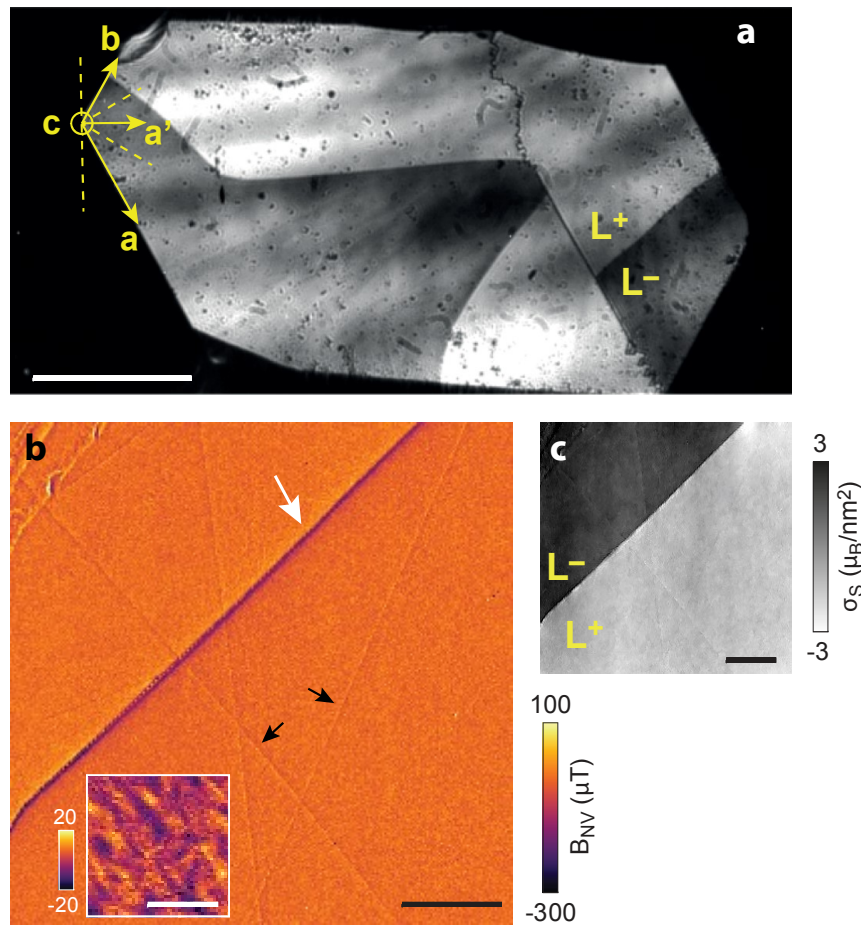


FIGURE 7.2: **Antiferromagnetic domain pattern in  $c$ -oriented  $\text{Cr}_2\text{O}_3$ .** **a**, SHG image revealing bright and dark domains of opposite order parameter in sample C; corresponding images for samples A and B are given in Figs. C.1 and C.2. The order parameter ( $L^+$  and  $L^-$ ) is assigned based on the magnetisation map in panel c. The image is acquired with right-handed circularly-polarised illumination. The two-fold axes  $a$ ,  $a'$  and  $b$  (crystallographic  $y$ -axes, yellow vectors), determined by x-ray crystallography, coincide with the in-plane magnetic easy axes of the spin-flop phase. Dashed lines indicate the in-plane magnetic hard axes. Scale bar:  $500\ \mu\text{m}$ . **b**, Magnetometry image of the stray field above a domain wall (white arrow) in sample A. Fainter features are due to surface topography, such as scratch marks from sample polishing (black arrows). The inset shows a high-sensitivity scan above a uniform domain on sample B, revealing weak stray fields due to surface roughness, see Appendix C.2.3. Dwell time per pixel is 1.5 s and the total acquisition time is 26 h. **c**, Surface magnetisation  $\sigma_z$  reconstructed from the stray field map of panel b, given in units of Bohr magnetons ( $\mu_B$ ) per  $\text{nm}^2$ . Scale bars for b and c:  $2\ \mu\text{m}$ .

#### 7.4.2 Domain-wall cross-section

To investigate the internal structure of a domain wall, we acquire a large number of magnetometry images along the domain wall and analyse the magnitude and spatial profile of the stray field [25, 48]. We then compare the magnetic field along the cross-section with the expected stray field from the static solution of the one-dimensional domain-wall model, Eq. (7.1), and compute the magnetic stray field from Eq. (7.1) using the forward propagation (see Eq. 5.4). By fitting the computed stray field to the experimental cross-section, we obtain quantitative estimates for the surface

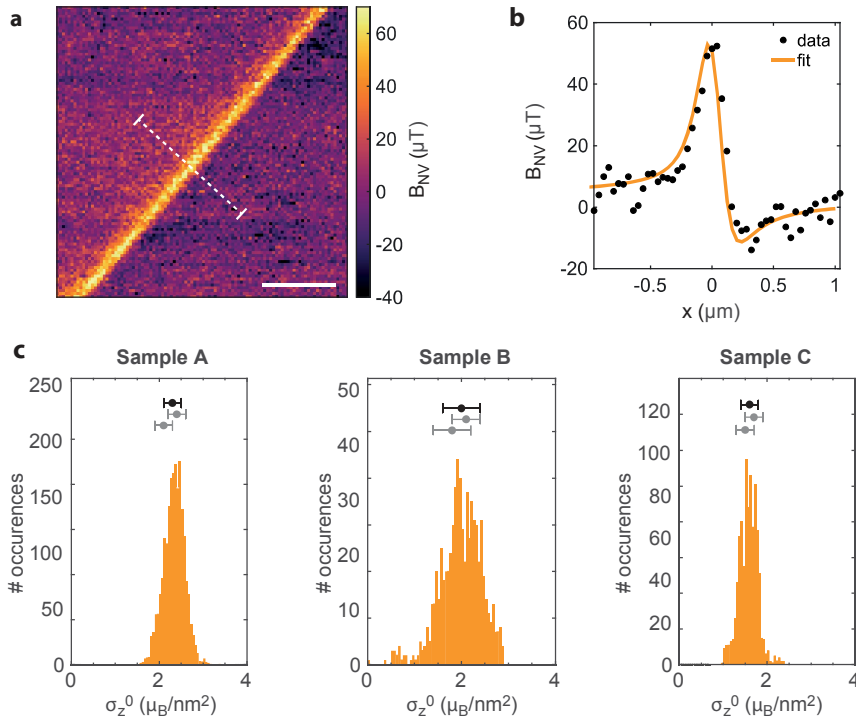


FIGURE 7.3: **Quantitative measurement of domain-wall structure and surface magnetisation.** **a**, Two-dimensional magnetometry scan of a domain wall in sample C. Scale bar: 1  $\mu\text{m}$ . **b**, Cross-section along the white dashed line in **a**, showing the stray field  $B_{\text{NV}}(x)$  as a function of the relative distance  $x$  to the domain wall. Dots are the experimental data and the solid line is a fit to the domain-wall model given by Eq. (7.1). Free fit parameters are the surface magnetisation  $\sigma_z^0$ , the domain-wall width  $\Delta_{\text{DW}}$ , and the angle  $\chi$ , see Appendix C.2.4. **(c)** Histograms of  $\sigma_z^0$  obtained from many line scan fits. Mean and standard deviation (s.d.) are included above the histograms as black dots with horizontal error bars ( $\pm 1\text{s.d.}$ ). Light grey bars reflect the  $\sigma_z^0$  values obtained by a secondary analysis (see Appendix C.2.5; the central bar reflects the step height, and the lower bar reflects the integrated  $B_x$  field). The number of line scans per histogram is 2512 for sample A, 726 for sample B, and 1012 for sample C.

magnetisation  $\sigma_z^0$ , domain-wall width  $\Delta_{\text{DW}}$ , and twist angle  $\chi$ . Figures 7.3a and 7.3b show an exemplary line scan across a domain wall of sample C together with the least-squares fit. To build statistics and avoid possible cross-correlation between fit parameters, we analyse about  $10^3$  line scans for each sample and validate results by a secondary data analysis (Figs. C.3 and C.4 in Appendix C). To exclude long-term drifts, we acquire scans along a domain wall in random order and find no temporal correlations as we proceed with the scanning.

### 7.4.3 Surface magnetisation

Figure 7.3c reports quantitative measurements of the surface magnetisation  $\sigma_z^0$ . We find a narrow distribution of  $\sigma_z^0$  values ranging from  $1.6(2) \mu_{\text{B}}/\text{nm}^2$  in sample C to  $2.3(2) \mu_{\text{B}}/\text{nm}^2$  in sample A. These values are only 15 – 21% of the theoretical  $\sigma_z^0$  for a perfectly ordered  $\text{Cr}^{3+}$  crystal, which is  $\sigma_z^0(0) = 10.9 \mu_{\text{B}}/\text{nm}^2$  for the surface termination shown in Fig. 7.2a at zero temperature (see Appendix C.2.1). The low  $\sigma_z^0$  is partially explained by the decay of magnetic order close to  $T_{\text{N}}$ , and is more pronounced for sample C due to the lower  $T_{\text{N}}$ . According to Ref. [76], the surface

magnetisation close to  $T_N$  is approximately given by  $\sigma_z^0(T) = \sigma_z^0(0)[1 - (T/T_N)]^{0.35}$ , which gives  $\sigma_z^0(T)/\sigma_z^0(0) \sim 30\%$  at  $T = 295$  K. Since low values for  $\sigma_z^0$  have also been reported by other experimental studies [76, 176], and since we observe a narrow distribution of  $\sigma_z^0$  that is uniform across the sample surface, we believe that the reduced  $\sigma_z^0$  is a general and unexplained property of  $\text{Cr}_2\text{O}_3$ . We hypothesise that the reduced surface moment density may be due to disorder within the exposed layer of terminating  $\text{Cr}^{3+}$  ions (see Fig. 7.1a).

#### 7.4.4 Domain wall chirality and width

Figures 7.4a-7.4c plot the fit results for the domain-wall width  $\Delta_{\text{DW}}$  and angle  $\chi$  obtained from the extensive datasets recorded on samples A-C. Each plotted  $(\chi, \Delta_{\text{DW}})$  pair represents a  $\sim 4 \times 4 \mu\text{m}^2$  magnetometry scan, and color-coding reflects the propagation direction of the domain wall. For samples A and B we find all domain walls to be predominantly Bloch-like, indicated by a  $\chi$  angle close to  $90^\circ$  (Fig. 7.4a and 7.4b). The domain-wall widths are not identical, but of similar magnitude  $\Delta_{\text{DW}} \sim 40$  nm, and well in the range of 20 – 80 nm predicted by theory [173]. Clearly, there is no correlation between  $(\chi, \Delta_{\text{DW}})$  and the spatial location or propagation direction  $\alpha$  of the domain wall (see Figs. 7.4d and 7.4e), indicating that the crystal structure plays no role in domain-wall formation. The consistency of the results from the two samples, which are grown independently by the same technique, confirms that our methods for quantifying the domain-wall structure are robust and reproducible.

Interestingly, sample C – which has an unusually strong global in-plane anisotropy [174] – shows a behavior that is distinctly different from samples A and B. Most prominently, we find both Néel and Bloch walls and a pronounced dependence of the twist angle on the wall orientation. For walls that run approximately parallel to one of magnetic hard axes (dashed lines in Fig. 7.2a and Fig. 7.4d-7.4f), the domain wall has a distinct left Néel character (blue data points in Fig. 7.4c). Once the angle  $\alpha$  between the propagation direction and the hard axis exceeds about  $9^\circ$ , the wall changes to Bloch-type, and becomes similar to samples A and B. In addition, the domain-wall width increases from  $\Delta_{\text{DW}} = 42$  nm the Néel to  $\Delta_{\text{DW}} = 65$  nm in the Bloch configuration. The correlation between  $(\chi, \Delta_{\text{DW}})$  and  $\alpha$  is not complete, but pervasive, suggesting that a delicate balance of interactions determines the local structure of the wall.

## 7.5 Discussion

The formation of distinct Bloch and Néel walls in  $\text{Cr}_2\text{O}_3$  is intriguing because, in the absence of a demagnetising field and in-plane anisotropy, the domain-wall energy of a collinear antiferromagnet is independent of the angle  $\chi$  [55, 57, 58]. Therefore, no domain-wall type is energetically favoured. In  $\text{Cr}_2\text{O}_3$ , however, domain walls have a non-vanishing local magnetic moment associated with the spatially inhomogeneous order parameter [57, 59], giving rise to a small but non-zero demagnetising field. We propose that this residual demagnetising field, which is mostly a bulk effect, is responsible for the observation of Bloch walls in samples A and B, similar to the situation encountered in uniaxial ferromagnets [159]. Note, that the local part of the dipolar interaction, which leads to the higher-order anisotropies as stated in the monographs of Turov and Akhieser, can also be relevant to determine the type of domain wall [62, 63].



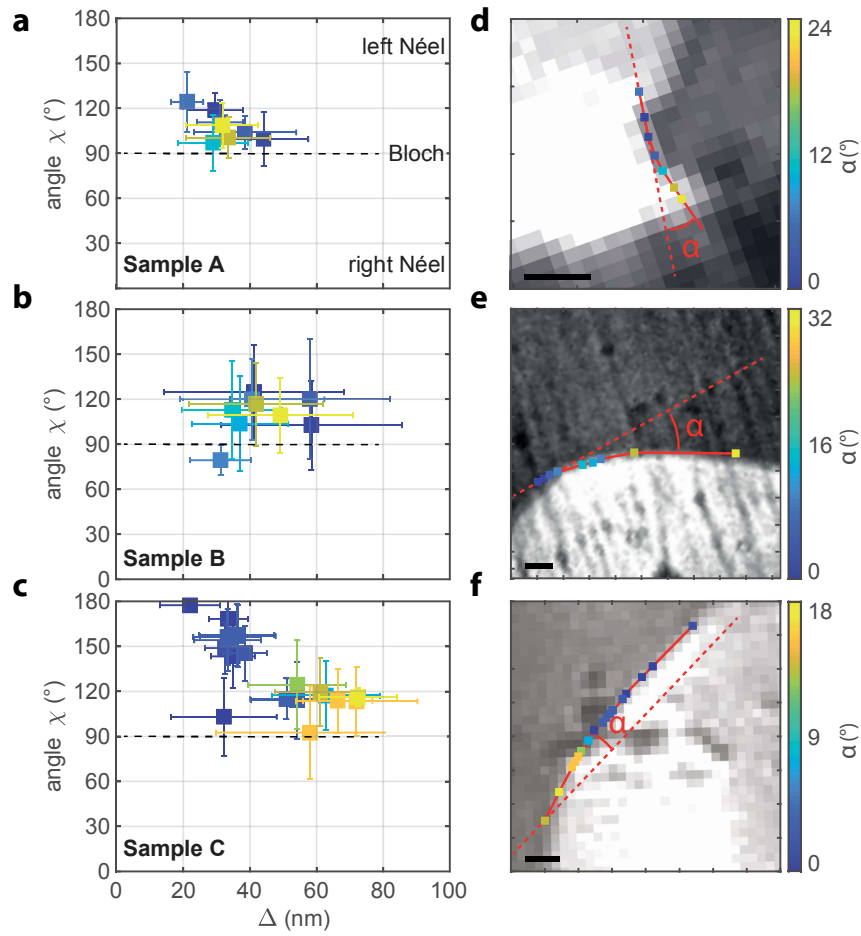


FIGURE 7.4: **Observation of Bloch and Néel walls.** **a-c**, Twist angle  $\chi$  plotted against the domain-wall width  $\Delta_{\text{DW}}$  for samples A-C. Each point represents the data from a two-dimensional magnetometry scan. Error bars ( $\pm 1$ s.d.) are obtained by separate fits to each line of the the 2D scan and computing the standard deviation (s.d.) of the fit results. Color coding reflects the propagation direction of the domain wall (see right panels). No correlation between chirality and spatial position is evident for samples A and B, whereas a clear correlation is evident for sample C. Mean angle and domain-wall widths are  $(\chi, \Delta_{\text{DW}}) = (106(6)^\circ, 34(5) \text{ nm})$  for sample A,  $(113(11)^\circ, 45(8) \text{ nm})$  for sample B,  $(143(12)^\circ, 42(6) \text{ nm})$  for sample C with  $\alpha < 9^\circ$ , and  $(117(7)^\circ, 65(4) \text{ nm})$  for sample C with  $\alpha > 9^\circ$ ; brackets denote standard error. **d-f**, SHG images of the domain-wall regions analysed in panels a-c. Colored squares show the scan locations.  $\alpha$  is the angle between the local propagation direction of the domain wall (red solid line) and one of the magnetic hard axes (red dashed line, see Fig. 7.2a). Scale bars: 25  $\mu\text{m}$ .

The preference for Bloch walls is challenged once significant in-plane anisotropy is present (sample C). An in-plane anisotropy favours  $\text{Cr}^{3+}$  spins aligned with the in-plane easy axis and for a sufficiently strong anisotropy, the domain wall is expected to change from Bloch to Néel (see Section 2.3). Due to the three-fold crystal symmetry of  $\text{Cr}_2\text{O}_3$ , three in-plane easy axes exist (that coincide with the crystal axes  $a$ ,  $a'$ , and  $b$ , see Fig. 7.2a) leading to six preferred directions in  $60^\circ$  intervals. Therefore, the  $\text{Cr}^{3+}$  spins will tend to align to the nearest preferred easy direction. The alignment is strongest when the domain wall is perpendicular to an easy axis, explaining the appearance of Néel walls near  $\alpha \approx 0^\circ$  (blue data points in Fig. 7.4c).

Once  $\alpha$  becomes larger, the in-plane anisotropy torque is reduced, and the domain wall eventually changes back to a Bloch type (yellow data points). The critical angle where this change occurs is not well defined but is roughly  $\alpha \approx 9^\circ$ . At the same time as the domain-wall type changes from Néel to Bloch, the domain-wall width is expected to increase, in line with our observation (Fig. 7.4c). Using Eq. (2.13) and setting  $M = s\sigma_z^0$ , the one-dimensional model predicts a ratio of domain-wall widths of  $\Delta_{\text{DW}}^{\text{Néel}} / \Delta_{\text{DW}}^{\text{Bloch}} = 0.85$  for  $\text{Cr}_2\text{O}_3$ , in reasonable agreement with the experimental result of  $r = 0.65 \pm 0.10$  (Fig. 7.4c). The good overall agreement between experiment and theory motivates the conclusion that the non-vanishing magnetic moment and in-plane anisotropy determine the domain-wall structure of  $\text{Cr}_2\text{O}_3$ .

A final point that remains to be explained is the preference for left chiral Néel walls in sample C, which is also partially present in samples A and B (Figs. 7.4a-7.4c). Although the asymmetry is conspicuous, it is not entirely surprising given the complex magnetoelectric properties of  $\text{Cr}_2\text{O}_3$  [175]. Because the orientation of the spins in a left chiral Néel wall is against the stray field produced by the uncompensated magnetisation of the top-most surface layers of  $\text{Cr}_2\text{O}_3$  (Fig. 7.1b), the preference for left walls cannot be attributed to a magnetostatic effect, unlike the change of a Bloch wall into a Néel wall observed in the near-surface region of ferromagnets [159]. Future theoretical work shall determine whether a wall-related DMI is responsible for the domain-wall chirality (see Section 2.3). In a non-centrosymmetric environment, the DMI results in canting of the spins when  $L$  has a non-zero in-plane component [43, 177], which, unlike in bulk  $\text{Cr}_2\text{O}_3$ , may be the case *within* the  $\text{Cr}_2\text{O}_3$  domain wall.

## 7.6 Summary and Outlook

In summary, we have resolved the spin structure of  $180^\circ$  domain walls in the prototype uniaxial antiferromagnet  $\text{Cr}_2\text{O}_3$ . We propose that the structure of the domain wall is determined by the weak energy scales provided by the non-vanishing magnetisation of the wall, the in-plane magnetic anisotropy, and possibly the DMI. Domain walls are Bloch-like in crystals with weak or negligible in-plane magnetic anisotropy, and either Bloch- or Néel-like in the crystal with larger in-plane anisotropy. In the latter case, the domain-wall type turns to Néel if the wall runs orthogonal to an in-plane easy axis, which coincides with the spin direction in the spin-flop phase of  $\text{Cr}_2\text{O}_3$  [163]. In agreement with simple theoretical considerations, the domain-wall width decreases from  $\Delta_{\text{DW}} = 65$  nm in the Bloch configuration to  $\Delta_{\text{DW}} = 42$  nm in the Néel configuration. Finally, the comparison between SHG and NSDM allows for determining the absolute sign of the order parameter in different domains, which is not possible by optical imaging alone.

Besides its fundamental interest, insight into the domain walls of collinear antiferromagnets is relevant for the development of antiferromagnetic spintronic devices that exploit current-induced domain wall motion to switch the orientation of the order parameter [17, 155]. For example, in antiferromagnetic/heavy-metal bilayers the domain wall velocity is predicted to be zero for Bloch walls when considering only the damping-like spin-orbit torque, and nonzero but offset by a threshold current density when including the field-like spin-orbit torque [17]. In contrast, a nonzero domain-wall velocity is predicted for Néel walls at any current density (in the absence of pinning), making this type of wall much more efficient for achieving current-induced domain-wall displacements. In our work, we show that the residual demagnetisation field in the walls of a collinear antiferromagnet with uniaxial

anisotropy favors the formation of Bloch walls, whereas the presence of in-plane magnetocrystalline anisotropy, likely in combination with chiral spin interactions, favors the formation of Néel walls. Future studies should aim at confirming the presence of a wall-related bulk DMI in  $\text{Cr}_2\text{O}_3$  and determine whether an additional interfacial DMI can be induced by proximity to heavy metals such as Pt.

In the next chapter, we extend the NSDM study of antiferromagnets for the first time to in-plane antiferromagnets applying the gained insights of the surface magnetisation to that type of antiferromagnet.



# Current-induced fragmentation of antiferromagnetic domains

## Summary

*Electrical and optical pulsing allow for manipulating the order parameter and magnetoresistance of antiferromagnets, opening novel prospects for digital and analog data storage in spintronic devices. Recent experiments in CuMnAs have demonstrated giant resistive switching signals in single-layer antiferromagnetic films together with analog switching and relaxation characteristics relevant for neuromorphic computing. Here we report simultaneous electrical pulsing and nanoscale scanning diamond magnetometry of antiferromagnetic domains in CuMnAs performed using a repetitive excitation scheme. We observe a nanoscale fragmentation of the antiferromagnetic domains, which is controlled by the current amplitude and independent of the current direction. The fragmented antiferromagnetic state conserves a memory of the pristine domain pattern, towards which it relaxes. Domain fragmentation coexists with permanent switching due to the reorientation of the antiferromagnetic moments. Our simultaneous imaging and resistance measurements show a correlation between the antiferromagnetic domain fragmentation and the largest resistive switching signals in CuMnAs.*

---

This chapter is based on the publication "Current-induced fragmentation of antiferromagnetic domains" (Ref. [35]). I conceived the work and designed the experiments together with P. Welter, T. Jungwirth, C. L. Degen and P. Gambardella. P. Welter and I performed the measurements, which were interpreted by myself, Z. Kašpar, K. Olejník, T. Jungwirth, C. L. Degen and P. Gambardella. I performed the reconstruction of the magnetic stray field maps and simulations together with C. L. Degen. T. Jungwirth, C. L. Degen, P. Gambardella and myself co-wrote the manuscript.

## 8.1 Introduction

Antiferromagnets have been established as promising candidate materials for memory devices capable of electrical or optical writing and readout [6, 91, 158]. Following in the footsteps of FMs, initial studies have focused on encoding information in the orientation of the magnetic order parameter, that is, in the orientation of the Néel vector [15, 178, 179]. In these early studies, an antiferromagnetic variant

of the current-induced spin-orbit torque [91, 180] has been considered as the underlying writing mechanism in, for example, thin metallic films of collinear room-temperature AFMs CuMnAs or Mn<sub>2</sub>Au [15, 178, 179]. Electrical 90° switching of the Néel vector in antiferromagnetic domains consistent with this scenario and controlled by the sign or orientation of the writing current has been confirmed by XMLD-PEEM [156, 178, 181–183].

Electrical readout signals observed after bi(multi)-polar writing current pulses have been attributed to the anisotropic AMR following the 90° reorientation of the Néel vector in the antiferromagnetic domains. Experiments with CuMnAs have shown that the onset of the AMR switching signal is correlated with the onset of the 90° domain switching seen in XMLD-PEEM at comparable threshold writing currents [181, 182]. In these measurements, which used 50-ms-long writing pulses with current densities of  $\sim 10^6$  A cm<sup>-2</sup>, the relative change in resistance due to the switching was limited to  $\sim 0.1\%$ .

Subsequent studies in CuMnAs [86, 184] have demonstrated switching pulse durations from ms to  $\sim 1$  ps with corresponding switching current densities increasing from  $\sim 10^7$  A cm<sup>-2</sup> to  $\sim 10^9$  A cm<sup>-2</sup>. Recently, the pulse duration has been reduced to 100 fs by replacing electrical switching with infrared laser pulses [8]. The observed resistive switching signals were independent of the light polarisation and could be controlled by the light intensity. The same study demonstrated that reversible switching signals could also be controlled by the amplitude of the electrical writing pulses without changing the current direction. The resulting resistive switching ratios have approached 20% at room temperature and  $\sim 100\%$  at 30 K [8]. These exceed by 2 – 3 orders of magnitude the AMR signals associated with the Néel vector reorientation [85, 181, 182] and, together with the observed optical switching, point to a complementary mechanism for writing information in AFMs.

In this work, we use NSDM to investigate the magnetic stray field emanating from antiferromagnetic domain textures during and after relaxation following the injection of current pulses into CuMnAs microdevices. Our study shows that the large resistive changes are correlated with a nanoscale fragmentation of domains induced by the writing current pulses. By imaging the current density distribution in microdevices with a cross geometry, we further show that the current-induced changes of the domain pattern are non-uniform across the devices. Images of the magnetic stray field acquired at varying delay times reveal that the fragmented domain patterns maintain a memory of the pristine state towards which they relax. In polarity-dependent switching experiments, we observe coexistence of fragmentation with a 180° Néel vector reversal in the domains. Our measurements shed light on the microscopic mechanisms leading to the electrical switching of metallic AFMs and point out directions for future research in the field of antiferromagnetic spintronics.

## 8.2 Imaging an in-plane antiferromagnet with nanoscale scanning diamond magnetometry

### 8.2.1 CuMnAs samples

Our samples are 30-nm- and 50-nm-thick CuMnAs films grown by molecular beam epitaxy on a GaP (001) substrate by Z. Kašpar, K. Olejník and V. Novák (see Appendix D.1). Tetragonal CuMnAs films consist of alternating Mn layers with opposite in-plane magnetisation. The crystal and magnetic structure of CuMnAs are shown in Fig. 8.1a. The possible set of domain orientations in these samples is re-

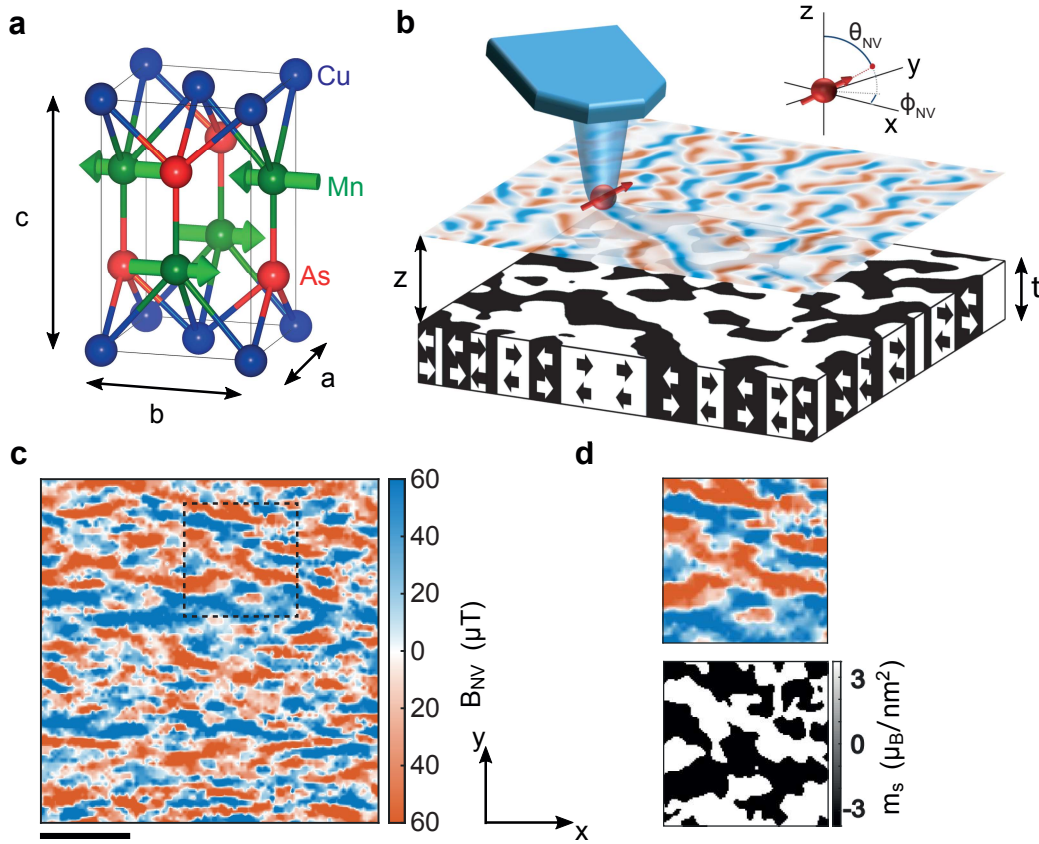


FIGURE 8.1: **Nanoscale scanning diamond magnetometry of CuMnAs.** **a**, Unit cell of CuMnAs. The magnetic moments of the  $\text{Mn}^{2+}$  ions (green arrows) are oriented in plane and alternate along the [001] direction (the  $c$ -axis). **b**, Schematic of the NSDM. A diamond tip (blue) containing an NV centre (red arrow) is scanned over an antiferromagnetic film (thickness  $t = 30 - 50\text{nm}$ ). Antiferromagnetic domains are represented by black and white areas with co-planar spins. The NSDM records the antiferromagnetic magnetic stray field  $B_{\text{NV}}(x, y)$  at a distance  $z = 50 - 100\text{nm}$  above the surface (red/blue pattern). The inset defines the  $(\theta_{\text{NV}}, \phi_{\text{NV}})$  vector orientation of the NV centre. **c**, Example of a magnetic stray field map of a pristine 30-nm-thick CuMnAs film. NV centre parameters are ( $z = 60 \pm 7\text{ nm}$ ,  $\phi_{\text{NV}} = 270^\circ \pm 5^\circ$ ,  $\theta_{\text{NV}} = 55^\circ$ ). **d**, Upper panel: Enlarged stray field map of area shown as dashed rectangular in panel c, Lower Panel: Domain pattern reconstructed from the field map in the upper panel as described in the text. Scale bar, 800 nm.

stricted by the magnetic anisotropy: in thinner films ( $t < 50\text{nm}$ ), the anisotropy tends to be uniaxial with a  $180^\circ$  reorientation of the Néel vector between adjacent domains. Thicker films have a stronger biaxial component and both  $90^\circ$  and  $180^\circ$  domain walls are present [182, 185]. XMLD-PEEM images indicate Néel-type domain walls with the Néel vector rotating in the  $a - b$  plane [182].

### 8.2.2 Reconstruction of the domain pattern

Figure 8.1b,c shows a schematic of the measurement principle and an example magnetic stray field map recorded from a 30 nm-thick CuMnAs film, respectively. For details on the NSDM measurement see Appendix D.2. To recover the domain pattern and analyse the measurements, we model the AFM by two thin layers of opposite

polarisation located at the top and bottom of the film, respectively (see Section 5.1.4 and Appendix D.3). Each layer carries a surface magnetisation of  $M_s = nms/V$ , where  $n$  is the number of  $\text{Mn}^{2+}$  ions per polarity per unit cell,  $m$  is the magnetic moment per  $\text{Mn}^{2+}$  ion,  $s = 0.2$  nm is the vertical separation between oppositely polarised  $\text{Mn}^{2+}$  ions, and  $V$  is the unit cell volume. The total magnetic stray field measured by the NV center is then given by the sum of top and bottom contributions, and dominated by the top layer because of the closer proximity to the probe. So, although our measurement technique is unable to resolve the individual magnetic moments, the stray field is effectively that of two very thin magnetised layers on each side of the film. Close to domain boundaries, this stray field is relatively strong and long-range enough to be picked up by our sensor.

In general, it is not possible to unambiguously reconstruct the magnetisation from the magnetic stray field map, as the divergence-free part of the magnetisation does not produce a stray field outside of the material, see Chapter 5. However, a rigorous reconstruction of the domain pattern can be obtained if we assume (i) uniaxial domain orientation with  $|M_s(x, y)| = M_s$ , and (ii) neglect the finite width of the domain walls (see Subsection 5.2.2 and Appendix D.4). Condition (i) can be assumed for thinner samples ( $t < 50$  nm) which have an uniaxial anisotropy[185]. For simplicity, we assume condition (ii) and consider later on broad domains. The reconstructed domain pattern from Fig. 8.1c is shown in Fig. 8.1d. We find that the easy axis is approximately pointing along the  $[110]$  ( $\pm y$ ) direction. Note that the magnetic field map in Fig. 8.1c relates the morphology of the domain pattern shown in Fig. 8.1d, provided that the spatial sensitivity is comparable to the domain feature size. Comparison with XMLD-PEEM images [181, 182] reveals similar domain patterns as those observed in Fig. 8.1d. Additional control measurements and simulations exclude ferromagnetic defects as the origin of the magnetic signals as these give rise to a much larger stray field (see Appendix D.5). A significant topography signal to the stray field due to atomic roughness can be excluded as detailed in Appendix D.10.

### 8.3 Current distribution and switching of CuMnAs microdevices

To investigate the effect of an electric current on the domain pattern, we combine electrical resistance measurements and NSDM. Figure 8.2 shows the cross-shaped geometry of a patterned CuMnAs device used for electrical pulsing experiments. According to previous XMLD-PEEM studies [181, 182], cross shaped devices enable  $90^\circ$  switching of the Néel vector by applying orthogonal current pulses or by flipping the polarity of the pulses (see Section 2.6). We define the orthogonal current directions  $P0^\pm$  and  $P1^\pm$  in Fig. 8.2a, where  $\pm$  indicates the polarity of the pulse. The direction of these current pulses is in line with existing work, and it is expected to maximise the observed AMR signal from the spin torques (see Section 2.6).

In a first step, we image the current density distribution by recording the Oersted field [33] (see Appendix D.6). In Fig. 8.2b we show the current distribution for the current direction  $P0^\pm$ . The current density is highest at the corners of the cross, as expected, and presents a granular texture that changes from device to device. Figure 8.2c shows an analogous current density map recorded for  $P1^\pm$ .

The magnetic stray field map in Fig. 8.2e shows the pristine state of the domain pattern of the 50-nm-thick CuMnAs film in the lower corner of the cross (dashed square in Fig. 8.2b), before any current pulses are applied. After applying a  $P0^+$



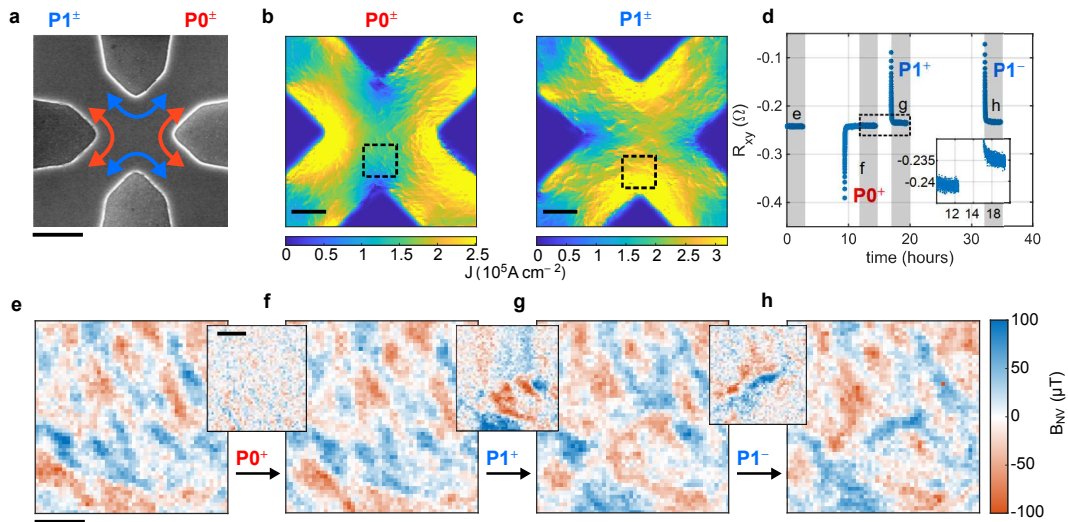


**FIGURE 8.2: Current distribution, electrical resistance, and magnetic stray field maps of the relaxed state after switching.** **a**, Scanning electron micrograph of a cross-shaped CuMnAs device. The arms of the cross are  $5\text{-}\mu\text{m}$ -wide and oriented parallel to the  $[100]$  and  $[010]$  crystal axes of the CuMnAs film. The pulse directions are defined as  $P0^\pm$  (red arrows) and  $P1^\pm$  (blue arrows). The sign denotes polarity of the pulse. Scale bar,  $5\text{ }\mu\text{m}$ . **b,c**, Current density distribution for  $P1$  and  $P0$  pulses measured using scanning NV magnetometry (see Appendix D.6). The current was  $0.8\text{ mA}$  for the device in panel b, and  $1\text{ mA}$  for the device in panel c. Scale bar,  $2\text{ }\mu\text{m}$ . **d**, Transverse electrical resistance  $R_{xy}$  as a function of time. Three current pulses of amplitude  $J = 1.58 \times 10^7\text{ A cm}^{-2}$ , duration  $100\text{ }\mu\text{s}$ , and different direction are injected during this measurement, as indicated next to each spike of  $R_{xy}$ . The measurement is performed simultaneously with the stray field scans shown in panels e-h. The total acquisition time of each scan is indicated by the shaded grey regions. The inset magnifies the electrical measurement within the dashed rectangle. A difference in the electrical signal is still visible after hours. **e-h**, Magnetic stray field images of the lower region of the cross (dashed square in panel b,c) before any pulsing (panel e), after a  $P0^+$  pulse (f), after a  $P1^+$  pulse (g), and after a  $P1^-$  pulse (h). The insets show difference images between successive scans. The NV sensor parameters are ( $z = 63 \pm 4\text{ nm}$ ,  $\phi_{\text{NV}} = 185^\circ \pm 5^\circ$ ,  $\theta_{\text{NV}} = 55^\circ$ ). Scale bar,  $400\text{ nm}$ .

pulse of  $56\text{ mA}$  and duration  $100\text{ }\mu\text{s}$ , corresponding to an average current density  $J = 1.58 \times 10^7\text{ A cm}^{-2}$  over the nominal  $\sqrt{2}(50\text{ nm} \times 5\text{ }\mu\text{m})$  cross-section of the device, we record a second magnetic stray field map (Fig. 8.2f). When comparing Figs. 8.2e and 8.2f, we observe no change of the stray field pattern due to a  $P0^+$  pulse. This observation is consistent with the current flowing mostly in the adjoining corners of the cross and a negligible current density in the mapped region. A  $P1^+$  pulse, on the other hand, produces a high current density in the imaged area (Fig. 8.2c), and we observe a significant change in the domain pattern. The strongest changes occur in the lower portion of the scan, where the current density is highest. This is consistent with the expected switching of the Néel vector in regions of high current density. Inverting the polarity of the pulse to  $P1^-$  also leads to a change of the domain pattern, as seen in Fig. 8.2h. The variation of the stray field between Figs. 8.2g and 8.2h is compatible with  $180^\circ$  switching of the Néel vector, as suggested by previous electrical measurements for pulses of opposite polarity [87], possibly in combination with  $90^\circ$  switching due to domain wall motion [182].

In addition to mapping the stray field and current density, we also record the transverse resistance  $R_{xy}$  by sending a readout current along one arm of the cross and measuring the voltage perpendicular to the current flow [178, 181]. The readout current amplitude is about fifty times weaker than the writing current and safely below the switching threshold. Electrical measurements performed after  $P0$  ( $P1$ ) pulses show a decrease (increase) of  $R_{xy}$  of  $\sim 160 \text{ m}\Omega$  with a characteristic decay time in the tens of seconds (Fig. 8.2d).  $R_{xy}$  is recorded for every pixel in the NV images simultaneously with  $B_{NV}$ . The time required to acquire a complete  $B_{NV}(x, y)$  map is about 3 h. The NV maps, therefore, correspond to a relaxed  $R_{xy}$  signal (grey regions in Fig. 8.2d). Despite an almost complete relaxation of the  $R_{xy}$  signal, a tiny  $\sim 5 \text{ m}\Omega$  difference remains between the relaxed  $R_{xy}$  values for  $P0$  and  $P1$  pulses even after many hours (inset to Fig. 8.2d), corresponding to a resistive switching ratio of less than 0.1% relative to the  $20 \text{ m}\Omega/\text{sq}$  sheet resistance of our film. Similarly weak electrical switching signals were linked in previous XMLD-PEEM studies to the  $90^\circ$  reorientation of the Néel vector in the antiferromagnetic domains and to the corresponding AMR [178, 181]. The initial values of  $R_{xy}$  before relaxation are, however, two orders of magnitude higher than the relaxed values. Both the large amplitude and the relaxation in a tens of seconds time-scale at room temperature have been reported in recent electrical and optical pulsing experiments [8]. These observations point to a new switching mechanism unrelated to the net Néel vector reorientation and AMR. In the following section we focus on the NV imaging of the AFM state corresponding to these initial unrelaxed  $R_{xy}$  signals within a few seconds after the writing pulse.

## 8.4 Current-induced domain fragmentation

To probe the domain structure during the initial fast decay of the electrical resistance, corresponding to the grey shaded region in Fig. 8.3a, we implement a repetitive excitation scheme that interleaves the data acquisition with electrical current pulsing. We also vary the current density to probe the relaxation after pulses that induce changes of  $R_{xy}$  in the  $\text{m}\Omega$  to  $\Omega$  range, as shown in Fig. 8.3b. In the repetitive excitation method, described in Fig. 8.3c, we apply a writing current pulse before the acquisition of each pixel and measure  $B_{NV}$  during the first 4 s after the pulse. Two scans are recorded at the same time, with their pixels interleaved, one after application of a  $P0^+$  pulse, the other after a  $P1^+$  pulse. In this way, we are able to probe the magnetic state averaged over the first 4 s of the relaxation process for both current directions. For these measurements we probe the central region of the cross-shaped devices, where approximately the same current density can be expected for  $P0$  and  $P1$  pulses. Examples of stray field images acquired in the repetitive excitation mode for a 30-nm-thick CuMnAs film are shown in Figs. 8.3d-g.

We first focus on writing currents close to the density threshold of the large switching  $R_{xy}$  signal. In Fig. 8.3a we show the time-dependence of  $R_{xy}$  after a  $100 \mu\text{s}$  writing pulse of average current density  $J = 1.89 \times 10^7 \text{ A cm}^{-2}$ , which is just above the threshold shown in Fig. 8.3b. The first image (Fig. 8.3d) acquired after  $P0^+$  pulses with  $J = 1.89 \times 10^7 \text{ A cm}^{-2}$  shows a stray field pattern very similar to that of the pristine sample, indicating that the current density in the centre of the cross is not sufficient to modify the antiferromagnetic domains in an appreciable way. Upon increasing the current density to  $J = 1.98 \times 10^7 \text{ A cm}^{-2}$ , however, we observe a striking reduction of the amplitude of the magnetic stray field (Fig. 8.3f), which we quantify by taking the root mean square of  $B_{NV}(x, y)$  over the entire magnetic field

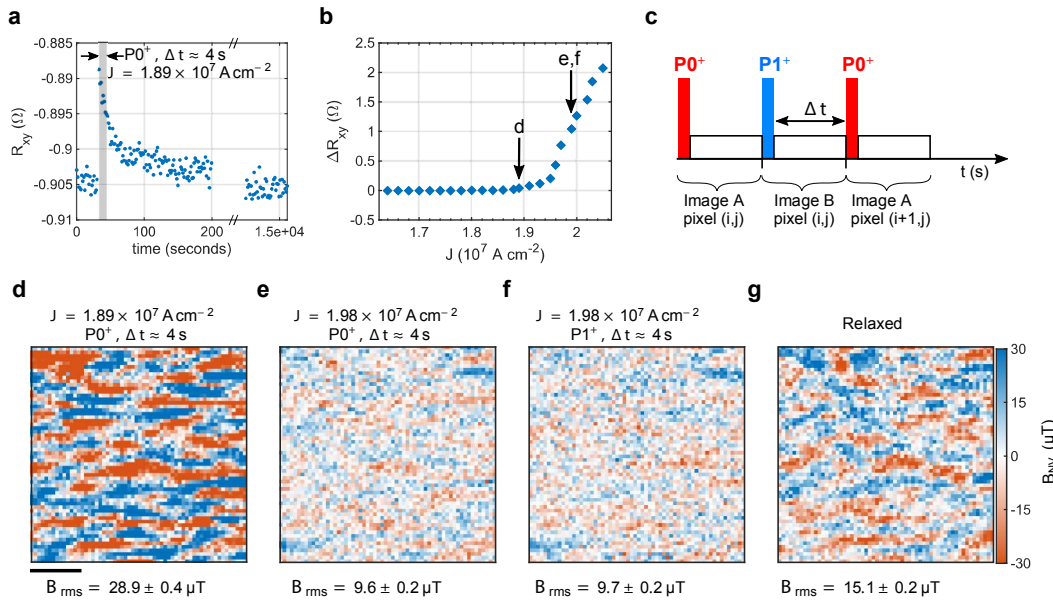


**FIGURE 8.3: Repeated excitation measurements and stray field maps of the excited and relaxed states.** **a**, Temporal evolution of  $R_{xy}$  after application of a single  $P1^+$  current pulse of amplitude  $J = 1.89 \times 10^7 \text{ A cm}^{-2}$  and duration  $100 \mu\text{s}$  to a 30-nm-thick CuMnAs device. The shaded region marks the period where the stray field was measured, see panels c-g. **b**, Current density  $J$  vs. maximum switching amplitude  $R_{xy}$ . **c**, Schematic of the measurement sequence. For each image pixel  $(i, j)$  we measure the magnetic stray field twice, once after a  $P0^+$  pulse and once after a  $P1^+$  pulse. The stray field measurement starts immediately after a pulse and is integrated over  $\Delta t = 4\text{s}$  (grey shaded area region in panel a). This sequence is repeated pixel by pixel to build up the images shown in panels d-g. **d-g**, Magnetic stray field maps of the 30-nm-thick CuMnAs film after  $P0^+$  pulses (d,e),  $P1^+$  pulses (f), and 75 hours after the last pulse (g). The measurements are performed in the centre of the cross and the pulse amplitude is given above each scan. The sensor parameters are ( $z \approx 52 \pm 11 \text{ nm}$ ,  $\phi_{\text{NV}} \approx 88^\circ \pm 5^\circ$ ,  $\theta_{\text{NV}} \approx 55^\circ$ ). Scale bar, 400 nm.

map,  $B_{\text{rms}}$  (see Appendix D.2). The reduction in  $B_{\text{rms}}$  is similar for the images acquired after  $P0^+$  and  $P1^+$  pulses (Fig. 8.3e,f), indicating that the direction of the writing current does not play a role in this effect.

Once the pulsing stops, the stray field amplitude slowly recover on a time scale of days. The relaxed image (Fig. 8.3g), which is acquired 75 h after applying the last pulse from Fig. 8.3f, shows that the system maintains a memory of the pristine domain configuration even after a long sequence of excitations. The memory effect is not perfect, as can be seen by comparing the upper left corner of Fig. 8.3d-g, but pervasive to both the excited and relaxed states. Note, that no obvious difference between  $P0$  and  $P1$  pulsing in panels 8.3e,f is visible, due to the strong uniaxial anisotropy present in that sample which hampers a  $90^\circ$  rotation of the Néel vector. In Appendix D.9, we show deterministic  $180^\circ$  switching, permitted by the uniaxial anisotropy, for the very same sample.

## 8.5 Simulation of the fragmented domain state

We now argue that the reduction of the stray field amplitude is caused by finely broken-up domains. This behaviour can be understood by simulating the stray field produced by varying domain configurations. We generate a domain pattern with finite domain wall width and its corresponding magnetic stray field map (see Figs. 8.4a and 8.4b, respectively) which present a similar morphology and magnetic contrast as the experimental data, shown in Fig. 8.3d. As detailed in Appendix D.7, we use image-to-image translation with conditional adversarial networks to find a best match for the domain pattern [186]. This approach allows for, in contrast to the reconstruction technique introduced in Subsection 8.2.2, implementing domain walls of finite width and states a more realistic description of the domain pattern. We introduce finely broken-up domains, i.e. fragmentation, retaining the overall shape of the domain pattern as defined by regions with a prevailing orientation of the Néel vector (Figs. 8.4c,d,f). The simulated stray field maps of the pristine and

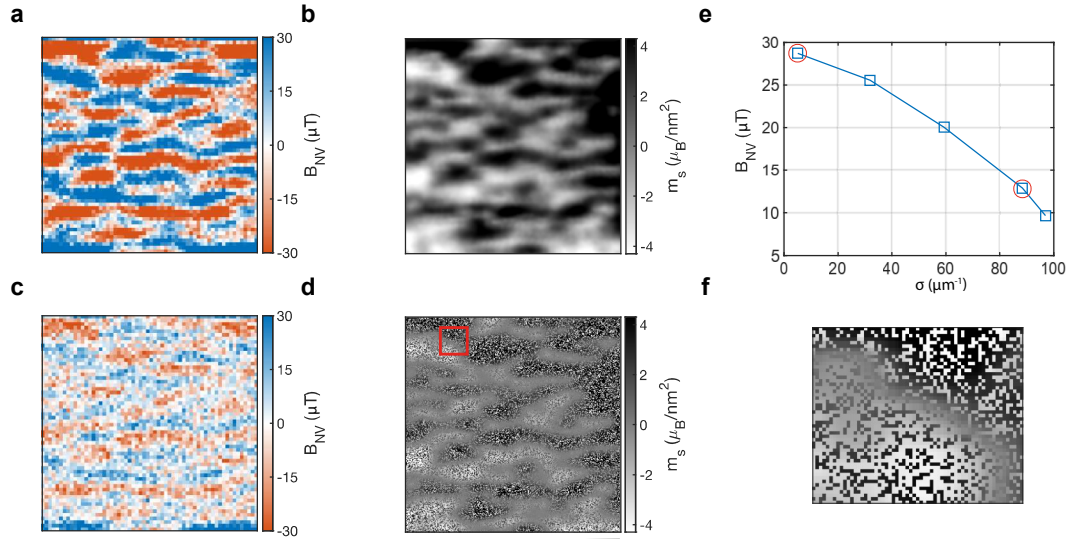


FIGURE 8.4: **Simulations of the stray field produced by a pristine and a fragmented domain pattern.** **a,b**, Simulated pristine domain configuration (panel b) and magnetic stray field (panel a) for a 30-nm-thick CuMnAs film with 75 nm broad domain walls and  $m_s = 4.3 \mu_B/\text{nm}^2$ . **c,d**, Simulated domain configuration (panel d) with finely broken up domains and magnetic stray field (panel c). **e**, The fragmentation leads to a reduction of the magnetic contrast  $B_{\text{rms}}$  with increasing domain wall density  $\sigma$ , whereas the overall shape of the stray field pattern is partially conserved. Red circles indicate the domain wall density and magnetic contrast in panel a and c. **f**, Magnification of red rectangular in panel d highlighting the finely broken up domains. Scale bar, 400 nm. See Appendix D.7 for details.

fragmented domains present a similar morphology but a different magnetic contrast, in agreement with the experiment, see Appendix D.7.1 for details. Alternative explanations to the reduction in magnetic contrast, such as heat-induced suppression of the magnetisation  $M_s$  or a change in sensor-to-sample distance  $z$  can be safely excluded, as the relaxation occurs on a much longer time scale compared to thermal effects and no drifts in the scanning setup are observed.

The decrease of  $B_{\text{rms}}$  can be qualitatively understood by noting that  $B_{\text{NV}}$  at a height  $z$  above the surface is most affected by changes of the magnetisation that



occur on the same length scale as  $z$ . Much larger and homogeneous structures generate stray fields only in the vicinity of the domain walls, whereas stray field lines of more localised structures are confined to the close proximity of the surface. In the context of domain imaging, this means that finely broken-up domains are too small to be resolved by the NV sensor. In the simulation, we introduce fragmentation by flipping islands at random positions in the magnetisation pattern. We find, that in order to observe the reduction in magnetic contrast by about 70 % as evidenced in Fig. 8.3e, the size of the islands needs to be smaller than  $6 \times 6$  nm. Here we assume sharp domain walls which were recently found in CuMnAs [187]. At this point, the question arises of how to characterise the fragmented domain state, i.e. as a domain pattern with very small domains or a glassy state with uncorrelated islands in the magnetisation pattern. Both are below the spatial resolution limit of the NV sensor and cannot be distinguished by our technique.

Comparing the reduction in  $B_{\text{rms}}$  to the results of our numerical simulations (Fig. 8.4e), we estimate that the current pulsing leads to an increase in domain wall density by a factor 10.

## 8.6 Correlation between domain fragmentation and resistive readout signal

To gain further insight into the relationship between magnetic domains and electrical resistance, we performed a series of repetitive excitation measurements for only one current polarity as a function of pulse amplitude. Figure 8.5a plots the transverse resistance  $R_{xy}$  as a function of time of a 50-nm-thick CuMnAs device while the current density is stepped up from 1.36 to 1.54 A cm<sup>-2</sup>. The measurements are performed in the lower corner of the cross, where the impact of the current is highest (see Fig. 8.2). At each current density step, we record a stray field map using the scheme of Fig. 8.3 and compute  $B_{\text{rms}}$ . As expected, the resistance signal increases with increasing current density. In addition, we observe that repeated pulsing at one set value of  $J$  leads to a further gradual increase of  $R_{xy}$ . Figure 8.5b shows that the increase in resistance is accompanied by a similar reduction in  $B_{\text{rms}}$ , clearly showing the correlation between the two effects. The correlation persists after the pulsing stops and the system slowly evolves towards the relaxed state (hours 38-60).

This series of measurements demonstrate that the reduction in  $B_{\text{rms}}$  does not depend on either the direction or polarity of the current, since it occurs for both orthogonal (Fig. 8.3) and unidirectional pulses (Fig. 8.5). Further experiments involving bipolar pulses show that the fragmentation occurs in combination with domain switching, as fragmented and relaxed images also show evidence of 180° reorientation of the Néel vector in certain areas of the scans (see Appendix D.9).

## 8.7 Domain wall resistance and electrical model

We estimate the influence of antiferromagnetic domain walls on the electrical resistance by considering a bar-shaped resistor following Ref. [188]. A domain wall, highlighted in grey in Fig. 8.6a, of width  $\Delta_{\text{DW}}$  and resistivity  $\rho_{\text{DW}}$  is inserted into the bar perpendicular to the current flow. We neglect the domain wall resistivity of a current flowing parallel to the domain wall which is, in ferromagnets, reported to be roughly six times smaller than the domain wall resistivity of a current crossing the domain wall perpendicularly [189]. The domain wall interface extends over the cross section  $w \cdot t$ . The resistance  $R$ , due to the domain wall resistivity is then given

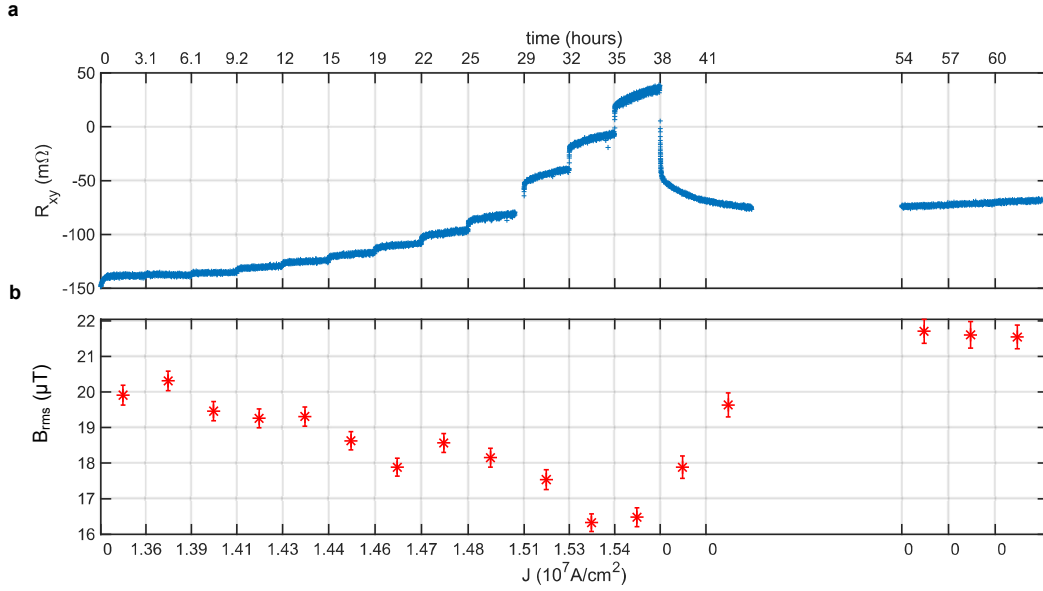


FIGURE 8.5: **Correlation between fragmentation and electrical resistance.** **a**, Change of the transverse resistance  $R_{xy}$  and **b**, Stray field amplitude  $B_{rms}$  versus current density  $J$  (bottom axis) and time (top axis) of the 50 nm-thick CuMnAs film.  $R_{xy}$  is plotted for every pixel in chronological order.  $B_{rms}$  is computed from stray field scans recorded at each  $J$  value in 3-hour intervals (vertical lines). The measurements are performed using the same scheme as in Fig. 8.3a, but only  $P1^+$  pulses are applied. The scan area is the same as in Fig. 8.2b,c. The NV sensor parameters are ( $z = 97 \pm 2$  nm,  $\phi_{NV} = 96^\circ \pm 3^\circ$ ,  $\theta_{NV} = 55^\circ$ ).

by

$$R = \rho_{DW} \cdot \frac{\Delta_{DW} \cdot N}{w \cdot t}, \quad (8.1)$$

where  $N$  is of number of domain walls inserted into the bar resistor. We express  $N$  via the domain wall density  $\sigma$ , i.e. the number of domain walls per unit length:

$$\sigma = \frac{N}{L}. \quad (8.2)$$

Combining Eqs. (8.1, 8.2) and setting  $L = w$ , we obtain a change in resistance

$$\Delta R = \rho_{DW} \Delta_{DW} \frac{\Delta \sigma}{t}, \quad (8.3)$$

where  $\Delta \sigma$  is the change in domain wall density due to fragmentation. We electrically model the CuMnAs device as a lumped network of 8 resistors, see Fig. 8.6b. The inner resistors  $R_i$  model the dominant resistance of the film. The outer resistors  $R_o$  represent the corners of the cross, some of which are fragmented during a write pulse. We assume that fragmentation only occurs in the areas modeled by the outer resistors, and that the inner area is unaffected. Consequently, a write pulse increases the outer resistance to  $R_o + \Delta R$ . The asymmetry introduced by this resistivity change gives rise to a transversal voltage (across leads 2 and 4) when a probe current is applied (through leads 1 and 3). The principle governing the appearance of the transversal voltage is effectively the presence of an unbalanced bridge circuit formed

by the outer 4 resistors.

We choose  $R_i = 250 \Omega$  and  $R_o = 88 \Omega$ . Not shown in Fig. 8.6b is the lead resistance, which we determined to be  $50 \Omega$ , based on the geometry of the leads and the bond pads. We choose these values such that, first, the current is mostly flowing around the corners, and, second, that the predicted resistance between two opposite leads matches the measured value ( $175 \Omega$  vs  $180 \Omega$ ). The transverse resistance is given by

$$R_t = \frac{2 \cdot R_i^2 \cdot \Delta R}{(2R_i + R_o) \cdot (\Delta R + R_i + R_o)} \quad (8.4)$$

Using the transverse resistance found in the experiment ( $R_t = 0.2 \Omega$ ), we estimate the change of resistance due to fragmentation  $\Delta R = 0.554 \Omega$ . This corresponds to a change in domain wall density from  $\sigma = 2.61 \mu\text{m}^{-1}$  to  $\sigma = 42.81 \mu\text{m}^{-1}$  according to our simulation, see Appendix D.8. Inserting the numbers in Eq. (8.3) we estimate a domain wall resistivity times domain wall width of  $\rho_{\text{DW}}\Delta_{\text{DW}} = 693 \mu\Omega\mu\text{m}^2$ .

We compare this value to the elemental antiferromagnet Cr with domain walls extending over several nanometers and the ferromagnet FePd [189, 190]. The domain wall resistivity in Cr is given by  $\rho_{\text{DW}} = 5 \mu\Omega\text{cm}$ . We obtain  $\rho_{\text{DW}}\Delta_{\text{DW}} = 50 - 250 \mu\Omega\mu\text{m}^2$  for a domain wall width ranging between  $\Delta_{\text{DW}} = 5 - 10 \text{ nm}$ . The domain wall resistivity in FePd is  $\rho_{\text{DW}} = 1.435 \mu\Omega\text{cm}$  for a domain wall width of  $8 \text{ nm}$ . The  $\rho_{\text{DW}}\Delta_{\text{DW}}$  product is hence about 1.4 – 2.8 times larger for elemental Cr and 6 times larger for FePd compared to the value we extract from our experiment.

Note that this analysis is rather crude, and these numbers should be taken with a grain of salt. We made some rough assumptions along the way, for instance on the size and geometry of the fragmented regions, neither of which are known. Nevertheless, it proves that fragmentation of the domain structure is a reasonable explanation for the appearance of a transverse voltage.

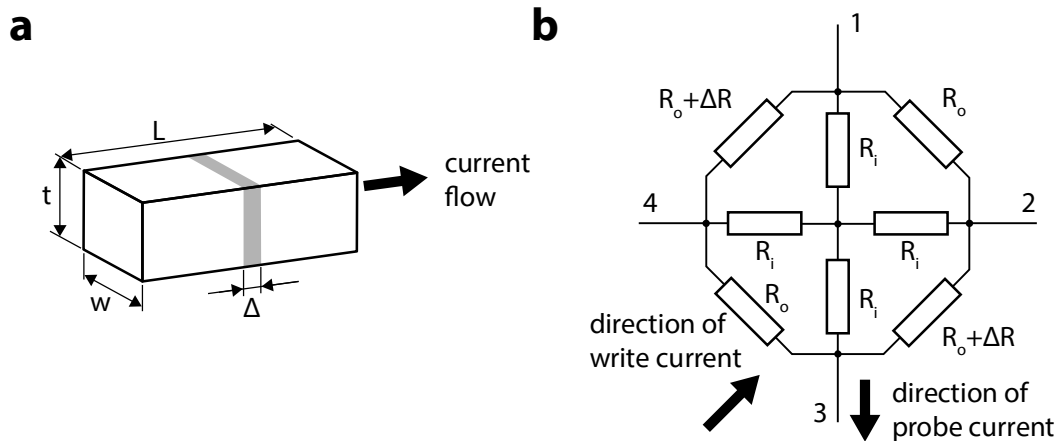


FIGURE 8.6: **Domain wall resistance, domain wall density and electrical model.** **a**, Bar resistor. A domain wall of width  $\Delta$ , shaded in grey, is inserted into the bar resistor. The current is flowing perpendicular through the domain wall. **b**, Electrical model the CuMnAs device as a lumped network of 8 resistors. The inner resistors  $R_i$  model the dominant resistance of the film. The outer resistors  $R_o$  represent the corners of the cross, that are fragmented during a write pulse. A write pulse increases the outer resistance to  $R_o + \Delta R$ .

## 8.8 Discussion and outlook

The fragmentation of the domain pattern in CuMnAs by electrical pulses and the subsequent recovery is distinct from the reorientation of the Néel vector in the antiferromagnetic domains demonstrated in the past. The fragmentation of the domains, as measured by the vanishing stray field contrast, increases with the number of current pulses and current density. Regions of highly fragmented domains are distributed non-uniformly throughout the sample, following the inhomogeneous current density distribution evidenced by Oersted field maps (see Appendix D.6). Fragmentation occurs for different pulsing strategies, namely for orthogonal pulses, reversed-polarity pulses, and unidirectional pulses, and in samples of different thicknesses (30 nm or 50 nm). We surmise it is a general effect likely governed by current-induced heating. The high current density heats the device past the Néel temperature, thereby altering the magnetic structure as the device cools down again (see Appendix D.11). However, we do not expect the temperature to be the case to reduce the magnetic stray field as the relaxation occurs on a much longer time scale compared to thermal effects. The degree of domain fragmentation correlates with the increase of the resistive readout signal up to high amplitudes that are well above the earlier identified AMR signals due to the reorientation of the Néel vector in the antiferromagnetic domains. The domain fragmentation thus provides a plausible explanation for the recently observed unipolar high-resistive switching signals in CuMnAs and their relaxation[8].

However, several points remain open for discussion. First, the influence of the fragmented state on the electrical resistance might be explained by the formation of a dense network of antiferromagnetic domain walls. In FMs, the influence of domain walls on the electrical resistivity is well documented [191–193]. For example, the striped domain phase of a Co film with a density of approximately  $0.005 \text{ nm}^{-1}$  domain walls perpendicular to the current flow causes a 5% increase of the resistivity compared to the uniform magnetic state [194]. In CuMnAs, the relative change of the resistivity can be possibly explained by the very high density of domain walls attainable in AFMs as detailed in Section 8.7. Although the large density of domain walls is striking, little is known about the influence of domain walls on the electrical transport in AFMs in general [153, 195]. Our findings might stimulate more work in this direction.

Second, it is unclear at this stage whether the magnetic fragmentation is accompanied by a modification of the crystalline structure of the AFM and perhaps driven by it. In the absence of grains in epitaxial films, the question arises why fragmentation does happen, i.e. where should the domain walls be pinned on to make the small-sized domains stable. At this stage, it is also not clear if the fragmentation is described by a glassy antiferromagnetic phase, i.e. disorder. Surface-sensitive photoemission, electron, and atomic force microscopy as well as bulk-sensitive transmission electron microscopy do not show structural changes in CuMnAs for pulsing conditions at which the highly reproducible resistive switching signals are observed, provided that they stay safely below the device breakdown threshold [196].

Third, the mechanism driving defragmentation is still unknown and might be related to the slow return to equilibrium. Also, the memory effect of the antiferromagnetic domain pattern is quite striking in itself. The samples that have undergone domain fragmentation relax to a stray field pattern that is very similar in intensity and spatial features to that of the domain configuration prior to pulsing. In general, only small scan areas show evidence of permanent switching, which we

attribute to  $90^\circ$  and  $180^\circ$  reorientation of the antiferromagnetic moments by current-induced torques, consistent with earlier XMLD-PEEM studies[181]. The memory of the domain pattern might point to a significant role of static defects in the film which could assist the magnetic effect as domain wall nucleation and pinning sites (an extensive characterization of defects in the epitaxial single-crystal films of CuMnAs is discussed elsewhere [196]). While still not fully understood microscopically, the possibility to switch between two distinct antiferromagnetic phases while retaining a memory of the pristine state demonstrates a new type of memristor in which information is encoded in the magnetic structure rather than in the crystal structure.

In conclusion, NSDM measurements revealed the complexity of the excited antiferromagnetic texture after current injection, showed a correlation between domain fragmentation and large resistive switching signals, and demonstrated a novel memristive effect. A full understanding of the mechanisms behind domain fragmentation, relaxation, and memory of the pristine domain configuration will require simultaneous investigation of the magnetic state and crystal structure on a local scale with bulk sensitivity and covering a broad range of time scales.



# Conclusions and Outlook

## 9.1 Summary of the main results

In this thesis, we develop novel scanning probe techniques to extract information about the spin structure in ferri- and antiferromagnets by recording the magnetic stray field emanating from the particular specimen. All major experiments are carried out on a home-built nanoscale diamond magnetometry microscope which we construct within the scope of this work.

### Nanoscale scanning diamond magnetometer

We build a nanoscale scanning diamond magnetometer with a spatial resolution of 50 nm and sensitivity of  $< 1 \mu\text{T}/\sqrt{\text{Hz}}$ . Long term drift can be reduced to 50 nm per 24 h. The design of the setup allows for easy replacement of devices and implementation of refined sensing protocols. The high sensitivity, spatial-resolution, and stable performance of the NSDM lead to a series of publications.

### Structure of domain walls and magnetic surface properties in the ferrimagnetic insulator TmIG

We analyse the internal structure of domain walls and surface magnetisation in ferrimagnetic TmIG. To resolve the domain wall, we combine NSDM with quantitative image reconstruction and analysis. We are able to resolve both the domain wall width and chirality, as well as the surface magnetisation with high sensitivity of TmIG and TmIG/Pt. The main results are:

- The domain walls of TmIG exhibit left-hand Néel chirality, changing to an intermediate Bloch-Néel character upon Pt deposition with a domain wall width  $\Delta_{\text{DW}} \approx 20 \text{ nm}$ .
- The results indicate the presence of a finite interfacial DMI, which makes it possible to stabilise chiral spin textures in centrosymmetric magnetic insulators such as spin spirals and skyrmions. Combined with the low current threshold for DW flow and the large DW mobility, this makes TmIG an ideal contender for spintronic applications.

## Co-existence of Bloch and Néel walls in a collinear antiferromagnet

Based on the insights and methods developed for the aforementioned TmIG study, we refine our techniques and apply them to the antiferromagnetic insulator  $\text{Cr}_2\text{O}_3$ . This is the first experimental observation of the structure of a domain wall in a pure, intrinsic antiferromagnet. Our findings are:

- The intrinsic domain wall structure is Bloch-like. Our experimental observation is significant because the theory does not predict any preference for Bloch or Néel walls. We suggest that the preference for Bloch walls is due to a non-vanishing magnetisation of the domain walls.
- The domain walls can become chiral (Néel-like) if sufficient in-plane magnetic anisotropy is present. This finding is important for potential use in antiferromagnetic spintronics.
- By correlating our magnetic measurements with SHG, we confirm that  $\text{Cr}_2\text{O}_3$  always has a defined surface polarity. Although indirect experimental evidence has been reported (Refs. [37, 170]), our measurements provide unambiguous proof for this hypothesis.

Because our work touches both fundamental aspects of antiferromagnetism and ferrimagnetism as well as perspectives for applications, we believe that results will attract significant interest in several fields of physics, especially in the ferroic materials and spintronic communities. In addition, our work also provides new methodology and concepts relevant to the quantum sensing and imaging communities.

## Current-induced fragmentation of antiferromagnetic domains

The work presented in Chapter 8 addresses the questions raised in the introduction about the mechanisms and type of switching as well as the amplitude of the magnetoresistive readout signal in antiferromagnets. Here, we combine for the first time NSDM with electrical pulsing and resistance measurements to shed light on the nature of the excited antiferromagnetic texture after current injection in CuMnAs.

- By mapping the very weak magnetic stray field emanating from the surface of CuMnAs, we show that the large resistive changes induced by unipolar current pulses are correlated with a nanoscale fragmentation of the antiferromagnetic domains.
- Images of the magnetic stray field acquired at different times reveal that the fragmented domain pattern maintains a memory of the pristine state towards which it relaxes.
- The fragmentation of the domains in CuMnAs by electrical pulses and their subsequent recovery are distinct effects from the reorientation of the Néel vector in the antiferromagnetic domains observed in previous studies. Whereas the reorientation of the Néel vector is attributed to the directional action of the spin-orbit torques, domain fragmentation is independent of the current direction, occurs on a length scale of about  $< 10$  nm, and has a clear current threshold beyond the typical range of currents investigated in the past.
- Fragmentation is a much more dramatic effect compared to domain reorientation, as it leads to the formation of a glassy antiferromagnetic phase with a different magnetic texture and dynamics compared to the pristine state of the antiferromagnet.



- We find that the degree of fragmentation correlates with the increase of the resistive readout signal up to amplitudes that are well above the earlier identified magnetoresistance signals, thus providing an explanation for the recently observed unipolar high-resistive switching signals in CuMnAs and their relaxation.
- Besides these observations, we show that NV magnetometry can be successfully applied to map the domain structure of in-plane antiferromagnets and demonstrate the possibility to perform repetitive NV measurements of current-induced excitations.

Our measurements shed light on the microscopic mechanisms leading to the electrical switching of metallic antiferromagnets, demonstrate a novel memristive effect, and point out directions for future research in the field of antiferromagnetic spintronics and NV microscopy.

## 9.2 Outlook

NSDM emerged as a competitive imaging technique with remarkable progress on antiferromagnets [35–37, 77, 162], multiferroics [34] and helimagnets [32]. However, challenges persist in the reconstruction of the spin texture from the magnetic stray field, which is key for understanding the properties of the aforementioned magnetic ordering. Although the non-bijective relation between the magnetisation and magnetic stray field prohibits a unique solution of the reconstruction, more refined concepts and methodology could be found to mitigate this problem.

Looking ahead, we foresee investigating spatiotemporal dynamics using NSDM. Thus far, NSDM has been applied only on static or quasi-static fields, however, sensing protocols to detect time-varying magnetic fields using NV centres already exist [105, 197–199]. Following the results presented in this thesis, time-resolved NSDM would allow for characterising the domain wall dynamics and verifying a change of the domain wall structure during motion due to field like torques as proposed by Shiino *et al.* [17]. The domain wall velocity in antiferromagnets is supposed to be orders of magnitude larger compared to ferromagnets, reaching the range of  $10 - 100 \text{ km s}^{-1}$  [200]. Assuming a domain wall velocity of  $10 \text{ km s}^{-1}$ , achieving a spatial resolution of 50 nm requires a time resolution of 5 ps. Time-resolved magnetometry with NV centres has been demonstrated with a resolution of 10 ns [105]. Technical innovations (increasing microwave drive power and integrating the waveguide on-sample) are expected to bring this down to the order of 1 ns, but are not trivial. Picosecond timescales are out of reach at this time, however, would open a wealth of applications in spintronics.

More specific research directions for the three systems presented in this thesis are listed below.

### TmIG

The presence of interfacial DMI interaction in magnetic garnets reduces upon Pt deposition. What remains open is the mechanism that leads to interfacial DMI, which has not been treated theoretically yet. If done so, optimisation of devices could be possible.

### **Cr<sub>2</sub>O<sub>3</sub>**

We expect that our methods and insights generated in our study on Cr<sub>2</sub>O<sub>3</sub> can be readily extended to other antiferromagnets, including bulk crystals and thin films. Related to our work on ferrimagnetic insulators and the novel physics of antiferromagnetic domain wall motion [13, 200–202], one could imagine a similar study on Cr<sub>2</sub>O<sub>3</sub>/Pt bilayer thin films. Future work may also include correlative imaging of antiferromagnetic and ferroelectric domain walls, so as to investigate the coupling between different types of order in multiferroic materials.

### **CuMnAs**

Our study shows that the large resistive changes are correlated with a nanoscale fragmentation of domains induced by the writing current pulses and associated heat. There is something fundamental and nontrivial in this effect, as shown by the relaxation and memory effects evidenced by our measurements. Outstanding questions, which might trigger research in those directions, are the definition of the fragmented state itself and the electrical transport in antiferromagnets in general [153, 195]. For example, Maniv *et al.* [203] recently proposed that the antiferromagnetic switching is driven by the collective dynamics of a coexisting spin glass. Our findings open a new path to optimise the readout signal of antiferromagnetic memories, suggesting the possibility of magnetic phase-change data storage.

## Calibration of the NV sensor

We employ diamond probes from QZabre LLC, <https://qzabre.com/>). The sensor vector orientation ( $\theta_{\text{NV}}$ ,  $\phi_{\text{NV}}$ ) and the sample-to-sensor distance  $z$  are calibrated before the measurement.

### A.1 Estimation of the spin vector orientation in the sensor

Since our probes are fabricated from  $\{100\}$ -cut diamond and mounted with a  $\{100\}$  surface parallel to the sample surface, the possible vector orientations are  $\theta_{\text{NV}} = 55^\circ$  and  $\phi_{\text{NV}} \in \{0^\circ, 90^\circ, 180^\circ, 270^\circ\}$ . To determine  $\phi_{\text{NV}}$ , we apply a magnetic bias field to the scanning sensor using a permanent magnet. We then move the relative position of the magnet and track the change of the magnetic resonance lines. By comparing the observed resonance frequencies to those predicted by an analytic model of the magnet's field, we can extract a best estimate for  $\phi_{\text{NV}}$  using a least squares minimization.

### A.2 Estimation of the sample-to-sensor distance $z$

The sample-to-sensor distance  $z$  is inferred by scanning the probe over a magnetic calibration sample (see Fig. A.1a). The calibration sample was a 1- $\mu\text{m}$ -wide and 7 nm thick perpendicularly magnetized Pt/Co/ $\text{AlO}_x$  stripe. For a stripe aligned with the  $y$ -direction, the magnetic stray field emanating from the stripe is given by

$$\begin{aligned} B_x &= \frac{\mu_0 M_s t}{2\pi} \left[ \frac{z}{z^2 + (x - x_0)^2} - \frac{z}{z^2 + (x - x_1)^2} \right] \\ B_y &= 0 \\ B_z &= -\frac{\mu_0 M_s t}{2\pi} \left[ \frac{x - x_1}{z^2 + (x - x_1)^2} - \frac{x - x_0}{z^2 + (x - x_0)^2} \right], \end{aligned} \quad (\text{A.1})$$

where  $x_0$ ,  $x_1$  denote the edge positions of the stripe,  $M_s$  the magnetisation of the Pt/Co/ $\text{AlO}_x$  film, and  $t$  the film thickness. By fitting this model to the experimental line scan we can extract values for the stand-off distance  $z$  and  $M_s t$  (see Fig. A.1b). Further, fit parameters are the edge positions and the azimuth angle  $\phi_{\text{NV}}$ . The latter can be independently determined using a permanent magnet, as described above. To improve statistics and estimate the error, we fit several line scans across the stripe using the same starting parameters and extract the mean value and standard error.

To compensate for the fact that we have not included the height profile of the stripe as well as the DMI, we deliberately over-estimated the error in the stand-off distance to be larger than the fit errors.

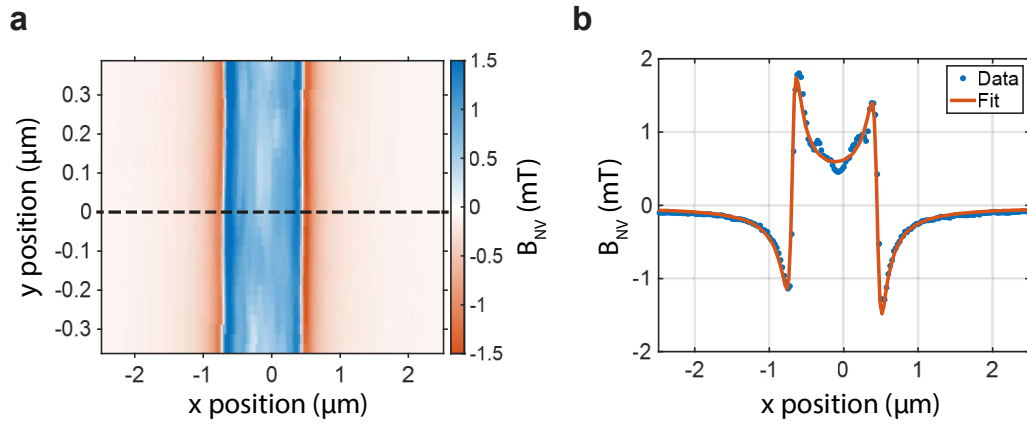


FIGURE A.1: **Calibration of the sample-to-sensor distance  $z$ .** **a**, Magnetic field map of a Pt/Co/AlO<sub>x</sub> stripe with out-of-plane magnetisation. **b**, Line scans across a 1  $\mu\text{m}$  wide and 7 nm thick Pt/Co/AlO<sub>x</sub> stripe, see dashed line in a. We fit the data to Eq. (A.1) with the fit parameters stand-off distance  $z$ , surface magnetisation  $M_{st}$  and edge position of the stripe  $x_0, x_1$ .

# High-speed domain wall racetracks in a magnetic insulator

## B.1 Nanoscale scanning diamond magnetometry measurement - details

Spatially resolved scans of the magnetic stray field produced by a domain wall, in TmIG (see Fig. 6.2a) were acquired on the NSDM microscope introduced in Chapter 4 using monolithic diamond probe tip with a single NV centre implanted at the apex (QZabre LLC). Experiments were carried out in an ambient environment and at zero magnetic bias field with 532 nm laser light. The laser power employed in our measurements was kept below 145  $\mu\text{W}$  and 10  $\mu\text{W}$  for the sample presented in Fig. 6.2 and the TmIG (8.5 nm) reference sample, respectively. No influence of the illumination power on the domain wall structure or position was noticed over time. To convert the spin resonance frequencies to units of magnetic field, we fitted the ODMR spectrum to a double Lorentzian and extracted the frequency difference  $\Delta f$  between the resonance peaks. The detected field  $B_{\text{NV}}$  is then given by  $B_{\text{NV}} = |\frac{\Delta f}{2\gamma_e}|$ , where  $\gamma_e = 28 \text{ GHz T}^{-1}$  is the electron gyromagnetic ratio, see Eq. 3.4 and Section 3.2. To re-establish the relative sign of  $B_{\text{NV}}$ , we inverted ( $B_{\text{NV}} \rightarrow -B_{\text{NV}}$ ) the image on one side of the domain wall (Fig. 6.2b).  $\theta_{\text{NV}}$  and  $\phi_{\text{NV}}$  were calibrated by a series of ODMR measurements and confirmed by line scans, see Appendix A. For the experiments presented in Fig. 6.2,  $\theta_{\text{NV}} = (55 \pm 2)^\circ$  and  $\phi_{\text{NV}} = (83 \pm 3)^\circ$ .

## B.2 Reconstruction of the surface magnetisation

By assuming that the magnetisation is predominantly out-of-plane, we reconstructed the surface magnetisation from the magnetic field map  $B_{\text{NV}}(X, Y)$  using Eq. 5.21

$$M_z = \frac{KB_{\text{NV}}\zeta}{\eta_{\text{FM}}(ik_X e_X + ik_Y e_Y + Ke_Z)}. \quad (\text{B.1})$$

Here, we added low-pass filter  $\zeta$  (cutoff  $\lambda = z$ ) that suppressed high spatial frequencies in the image [204]. Independently of the thickness of the film, Eq. B.1 yields the surface magnetisation of the film in units of magnetic moment/area, i.e., it provides the value of  $M_z t$ . The resultant  $M_z(X, Y)t$  surface map is plotted in Fig. 6.2c. Note that while the magnetic domains of TmIG and TmIG/Pt are well reproduced, the

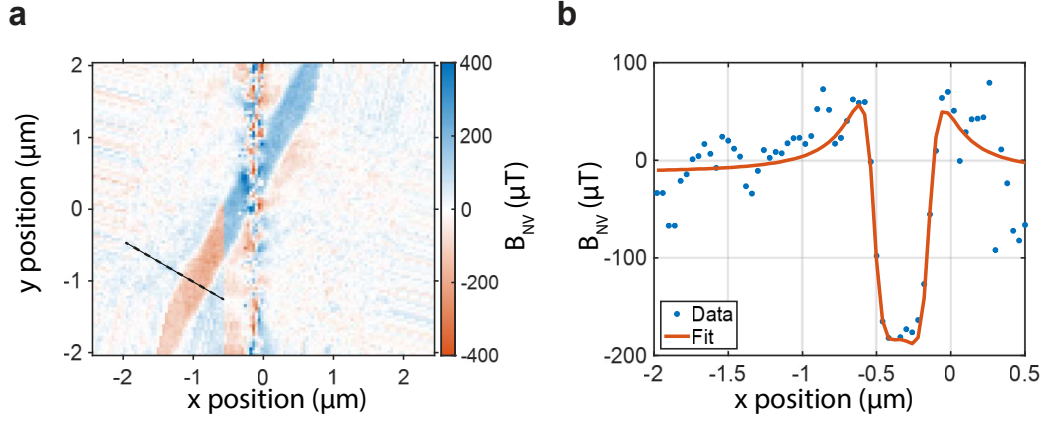


FIGURE B.1: **In situ calibration of the NV stand-off distance on TmIG/Pt.** **a**, Differential stray field image. The plotted image was obtained by subtracting two original images (Fig. 6.2b) that were shifted relative to each other by 800 nm along the Pt edge. **b**, Representative line cut of the differential image along the dashed line indicated in **a**, together with the fit according to Eq. (A.1).

reconstruction slightly overestimates  $M_z$  near the domain wall due to the left Néel character of the domain wall.

### B.3 Determination of the sample-to-sensor distance $z$

The sample-to-sensor distance  $z$  is inferred in situ from the change in the stray field  $B_{NV}$  at the TmIG/Pt edge (see Fig. 6.2b) due to the different magnetic response of TmIG relative to TmIG/Pt (see Fig. 6.2c), which we mainly attribute to a proximity induced polarization of the Pt layer (see second dataset taken in a reference TmIG film). The change in magnetisation gives rise to a stray field that is added to the field produced by the domain wall. In order to disentangle both fields we use a differential approach by shifting the images along the  $y$ -axis and subtracting them from each other, see Fig. B.1. In this way we cancel the domain wall stray field and end up with a stray field showing only two Pt edges. The magnetic stray field emanating from the Pt edges, with the image orientated such that they are aligned with the  $y$ -direction, can be described analytically as shown in Appendix. A. By fitting this model to the experimental line scan we can extract a value for the stand-off distance  $z$  and surface magnetisation  $M_{s,Pt}$ . Further fit parameters are the edge positions and the azimuth angle of the NV vector orientation. To improve statistics and estimate the error, we fit several line scans across the stripe using the same starting parameters and extract the mean value and standard error. For the image shown in Fig. 6.2b and Fig. B.1, we obtain  $z = 104 \pm 3.3$  nm. Further sample-to-sensor distance measurements on a separate calibration sample (Pt/Co/ $\text{AlO}_x$ ) before and after the domain wall measurement are in good agreement with this value. To compensate for the fact that we have not included the height profile of the stripe as well as the DMI, we deliberately over-estimated the error in the sample-to-sensor distance to be larger than the fit errors and set it to 5 nm.

## B.4 Fits of the domain wall magnetisation profile

We fit several line scans of the domain wall in TmIG and TmIG/Pt using the same starting fit parameters as described in Section 6.3. The resulting fit parameters  $p_i$  are averaged, with weights  $w$  according to their variance. The sum is taken over all line scans corresponding to the selected region. The nominal value of the parameters are calculated as  $\bar{p}_i = \sum_{k=1}^N w \cdot p_{i,k}$ , where  $k$  indicates the number of the scan. The standard deviation of each parameter is then  $\sigma_i = \sqrt{\sum_{k=1}^N (w \cdot p_{i,k}^2 - \bar{p}_i^2)} + \left(\delta z \frac{\partial \bar{p}_i}{\partial z}\right)$ . The last term describes the uncertainty due to the error of the sample-to-sensor distance  $\delta d$ . Since the fitting algorithm assumes the stand-off distance to be fixed, it is not included in the fitting results directly. We estimate  $\frac{\partial \bar{p}_i}{\partial z}$  via finite differences by repeating the fitting procedure with the sample-to-sensor distance equal to the error boundaries  $z^\pm = \bar{z} \pm \delta z$  with  $\bar{z} = 104$  nm.

## B.5 Reference TmIG film

We recorded a second dataset with a different scanning probe ( $d = 66 \pm 6$  nm) on an unprocessed TmIG film of thickness 8.5 nm, see Fig. B.2. Note, that the sample-to-sensor distance  $z$  was estimated on a Pt/Co/AlO<sub>x</sub> calibration stripe, see Appendix A. Analysis of this second dataset yielded a chiral angle of  $\psi = (180 \pm 0)^\circ$ , which corresponds to a pure left-handed chiral Néel domain wall structure, a domain wall width of  $\Delta_{DW} = (20 \pm 4)$  nm, and an out-of-plane surface magnetisation  $M_z t = (48.9 \pm 3.2) \mu_B/\text{nm}^2$ , which corresponds to  $M_Z = (53 \pm 4) \text{ kA m}^{-1}$ . These values are consistent with the ones presented in Fig. 6.2 for TmIG(8.3 nm), supporting the finding of a stronger DMI in an all-oxide structure without the presence of a metallic heavy metal layer.

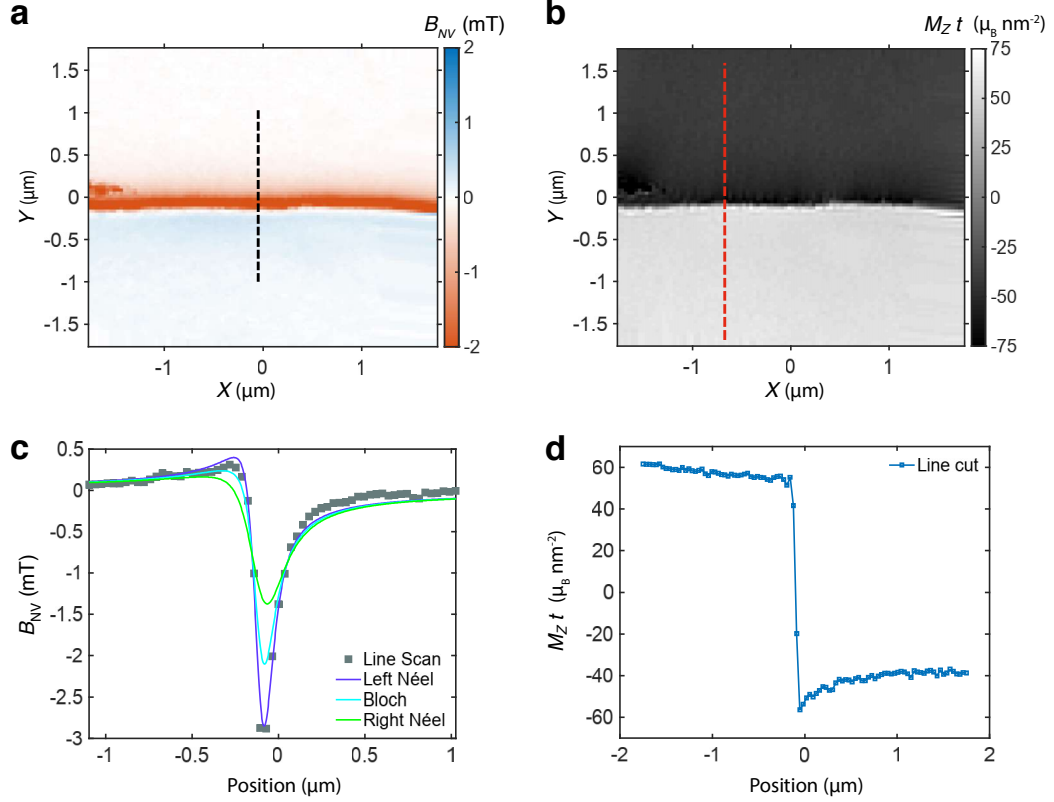


FIGURE B.2: **Domain wall structure and surface magnetisation in the reference sample TmIG.** **a**, Stray field map  $B_{NV}(X, Y)$  above a domain wall in the reference sample TmIG measured by NSDM. **b**, Reconstructed out-of-plane magnetic surface map  $M_Z(X, Y)t$  from the data shown in **a**. For reconstruction details see appendix B.2. **c**, Line scan of  $B_{NV}$  along the dashed lines indicated in **a** (square dots). The solid lines are calculated  $B_{NV}$  profiles using Eq. (6.1) assuming pure Bloch ( $\psi = 90^\circ$ , cyan), left-handed Néel ( $\psi = 180^\circ$ , violet), and right-handed Néel ( $\psi = 0^\circ$ , green) domain wall structures for comparison with the measured stray field profiles similar to Fig. 6.2. **d**, Line cut of  $M_Z(X, Y)t$  along the dashed line shown in **b**. Details of the fit results are given in the text.





# Co-existence of Bloch and Néel walls in a collinear antiferromagnet

## C.1 Materials and Methods

### C.1.1 Sample preparation

We study  $\text{Cr}_2\text{O}_3$  domain walls on three bulk single crystals. Samples A and B (Refs. [49, 71, 163]) are grown by the Verneuil method and oriented using a single-crystal X-ray diffractometer. The samples are cut perpendicular to the  $z$ -axis or (001) orientation. Subsequently, the samples are thinned down to  $70\ \mu\text{m}$ . Both samples are lapped and polished, each of them following a different process. Sample A is lapped using SiC powder with  $3\ \mu\text{m}$  grain size on a cast-iron-lapping plate. Subsequently, the sample is polished following a two-step process. In the first step, the lapped surface is polished with a soft metal plate using diamond powder with  $1\ \mu\text{m}$  grain size. In the second step, a refining polishing step follows using a polyurethane polishing plate together with colloidal silicate. Here, scratches from previous mechanical treatments are removed. The sample surface is polished until it reveals a root-mean-square (rms) roughness below  $1\ \text{nm}$ . Sample B is lapped using  $\text{Al}_2\text{O}_3$  powder and  $\text{H}_2\text{O}$  solution. Next, the lapped surface is diamond polished until it reveals a surface with a rms roughness below  $3\ \text{nm}$ . Sample C (Ref. [49]) is a flux-grown (001)  $\text{Cr}_2\text{O}_3$  platelet of  $30\ \mu\text{m}$  thickness. The flat as-grown surface presents a rms roughness below  $0.5\ \text{nm}$ . SHG images of all crystals are shown in Figs. C.1 and C.2. We create antiferromagnetic domains by cooling samples through the transition temperature  $T_N$ . For samples A and B, domains are induced by magnetoelectric poling [175]. In sample C, different domain patterns spontaneously form when the sample is cooled through  $T_N$ .

### C.1.2 Second harmonic generation measurements

SHG microscopy exploits an interference contrast of frequency-doubled optical photons in domains of opposite magnetic polarisation to reveal the domain pattern [71]. A magnetic contribution to the frequency-doubled light wave coupling linearly to the antiferromagnetic order parameter  $\pm L$  interferes with a frequency-doubled crystallographic background contribution which identifies the two antiferromagnetic domain states by their different brightness [70]. A transmission SHG setup is used to acquire the SHG images, in which a Coherent Elite Duo laser system is employed,

which emits 120 fs pulses at a repetition rate of 1 kHz. An optical parametric amplifier tunes the wavelength to excite the bulk  $\text{Cr}_2\text{O}_3$  samples with a photon energy of 1.033 eV and a pulsed energy of  $80 \mu\text{J}$ . The crystals are excited in transmission and at normal incidence by an unfocused circularly-polarised laser beam. Right-handed circularly-polarised light denotes the clockwise rotation of the electric-field vector of light with respect to its propagation direction. The opposite follows for left-handed circular polarisation. A camera lens is used to collect the SHG signal. Optical filters are added to select the SHG spectral wavelength, suppressing the fundamental beam and higher-harmonic contributions. SHG light is detected at room temperature with a Jobin-Yvon, back-illuminated, deep-depletion digital camera with a near-infrared detector chip of  $1024 \times 256$  pixels. The camera is cooled with liquid nitrogen to reduce thermal noise.

### C.1.3 Nanoscale scanning diamond magnetometry measurements - details

Nanoscale scanning diamond magnetometry measurements are carried out on the setup introduced in Chapter 4 using 520 nm laser light. Laser illumination is kept below  $90 \mu\text{W}$  to avoid laser-induced heating of the sample. Four different diamond probes (QZabre LLC) of  $\sim 22\%$  CW ODMR contrast at a measurement count rate of  $\sim 200$  kC/s are used. The sensitivity of these probes (as determined from the average least-squares variance of the center frequency) is  $1.7 \mu\text{T}$  for an integration time of 6.4 seconds per pixel. All scans are performed on the  $\text{Cr}_2\text{O}_3$  surface pointing towards the camera in the SHG experiment.

We use both continuous and pulsed ODMR protocols [205, 206] introduced in section 3.3 and section 3.4, respectively, on either transition ( $m_s = 0$  to  $m_s = \pm 1$ ) of the NV center. A small external bias field of  $\sim 4$  mT is applied to split the spin resonances; this small bias field is not expected to influence the  $\text{Cr}_2\text{O}_3$  physics. To convert the measured spin resonance frequency  $\nu$  to units of magnetic field, we compute

$$B_{\text{NV}} = \frac{\nu_0 - \nu}{28.02 \text{ MHz/mT}} \quad (\text{C.1})$$

where  $\nu_0$  is the mean frequency taken over the entire scan, which is approximately the frequency far from the sample surface. The sensor vector orientation is predetermined for each tip using an external field sweep (see Appendix A). The sample-to-sensor distance  $z$  between NV center and the sample surface is measured by independent calibration scans over a magnetised Pt/Co/ $\text{AlO}_x$  stripe before and after the  $\text{Cr}_2\text{O}_3$  scans (see Appendix A). For our probes,  $(\theta_{\text{NV}}, \phi_{\text{NV}}, z)$  is  $(55^\circ, 270^\circ, 73 \pm 7 \text{ nm})$  for tip A,  $(55^\circ, 180^\circ, 64 \pm 4 \text{ nm})$  for tip B,  $(55^\circ, 176^\circ, 65 \pm 3 \text{ nm})$  for tip C and  $(55^\circ, 176^\circ, 68 \pm 8 \text{ nm})$  for tip D.

## C.2 Data analysis

### C.2.1 Effective surface magnetisation $\sigma_z^0$

Antiferromagnetic order in the form of vertically alternating layers of oppositely polarised ions leads to an effective surface layer magnetisation on the top and bottom surfaces of the crystal, in analogy to the bound surface charge appearing for a polarised dielectric [170, 207, 208]. To calculate the surface magnetisation, we assign

the alternating layers of opposite polarisation to two oppositely magnetised volumes, each with magnetisation  $M_s = nm/V$ , vertically shifted with respect to each other by  $s$ . Here,  $n$  is the number of ions per unit cell and polarisation direction,  $m$  is the magnetic moment per ion, and  $V$  is the volume of the unit cell. Within the bulk, the magnetisation of the two volumes is exactly compensated, except in two thin layers of thickness  $s$  at the top and bottom of the body. Thus, the bulk antiferromagnetic order appears like a magnetised surface layer at the top and bottom of the crystal, with an effective layer magnetisation of

$$\sigma_z^0 = dM_s = \frac{nms}{V}. \quad (\text{C.2})$$

For thick crystals, a local magnetic probe only detects the stray field of the top layer.

$\text{Cr}_2\text{O}_3$  has a hexagonal unit cell with a lattice constant of  $a_{\text{hex}} = 4.96 \text{ \AA}$ , corresponding to a side length of  $a/\sqrt{3} = 2.86 \text{ \AA}$ , a height of  $c = 13.6 \text{ \AA}$ , a hexagonal surface area of  $A = \frac{3\sqrt{3}}{2}a^2 = 21.3 \text{ \AA}^2$ , and a volume of  $V = Ac = 290 \text{ \AA}^3$  (Refs. [49, 170]). The hexagonal unit cell is constructed from six vertically stacked  $\text{O}^{2-}$  planes. Each  $\text{O}^{2-}$  plane has two nearest  $\text{Cr}^{3+}$  ions of opposite magnetic polarisation located  $0.941 \text{ \AA}$  above or below the plane, respectively, therefore  $s = 1.88 \text{ \AA}$  (see Fig. 7.1 and Ref. [49]). Accounting for the 12  $\text{Cr}^{3+}$  ions per unit cell,  $n = 6$  for each orientation. Assuming a moment of  $m = 2.8 \mu_{\text{B}}$  per  $\text{Cr}^{3+}$  ion [209], we calculate a surface magnetisation of

$$\sigma_z^0 = \frac{6 \times 2.8 \mu_{\text{B}} \times 0.188 \text{ nm}}{0.290 \text{ nm}^3} = 10.9 \mu_{\text{B}}/\text{nm}^2. \quad (\text{C.3})$$

This is slightly less than what one would expect from one monolayer of  $\text{Cr}^{3+}$  ions, which would have a magnetisation of  $m/A = 12.1 \mu_{\text{B}}/\text{nm}^2$ .

### C.2.2 Reconstruction of the surface magnetisation $\sigma_z$

Under the assumption that the magnetisation is fully out-of-plane ( $sM_x = \sigma_x = \sigma_y = 0$ ), we can reconstruct the surface magnetisation  $sM_z = \sigma_z$  from the stray field  $B_{\text{NV}}$ . We start with Eq. (5.21) and use the definition of the surface magnetisation detailed in the previous subsection and Subsection 5.1.4

$$\sigma_z = sM_z = s \frac{KB_{\text{NV}}}{\eta_{\text{AFM}}(ik_x e_x + ik_y e_y + Ke_z)} \quad (\text{C.4})$$

Using Eq. (5.13) for a thick AFM film  $z \ll d$ , the expression simplifies to

$$\sigma_z = \frac{2\zeta B_{\text{NV}}}{\mu_0 e^{-Kz}(ik_x e_x + ik_y e_y + Ke_z)} \quad (\text{C.5})$$

In the last step, we have introduced a suitable window function  $\zeta = \zeta(k)$  (here a Hann function) that provides a high-frequency cutoff. Although our  $\text{Cr}_2\text{O}_3$  films do have an in-plane component in the vicinity of the domain wall, the reconstructed  $\sigma_z$  still accurately reproduces the domain pattern and surface magnetisation  $\sigma_z^0$ .

### C.2.3 Magnetic field from surface roughness

Surface roughness leads to tiny stray fields at topographic steps, as sketched in Fig. 7.1b. The magnetic field produced at a step of height  $h$  corresponds to the differential field of two magnetized layers located at  $z$  and  $z + h$ . According to Eq. (5.18)

with Eq. (5.12), the  $B_z$  field of the step is given by

$$B_z = \frac{1}{2}\mu_0 K s M_z \left[ e^{-Kz} - e^{-K(z+h)} \right] = \frac{1}{2}\mu_0 K \sigma_z e^{-Kz} \left[ 1 - e^{-Kh} \right], \quad (\text{C.6})$$

which transforms for  $Kh \ll 1$  to

$$B_z = \frac{1}{2}\mu_0 e^{-Kz} Kh (K\sigma_z). \quad (\text{C.7})$$

For a simple order-of-magnitude estimate of the stray field, we look at the Fourier component of  $\sigma_z$  that produces the strongest  $B_z$ . This occurs for  $K = 2/z$ . For this Fourier component, the amplitude of  $B_z$  is

$$B_z = \frac{\mu_0 h 2 e^{-2} M_s}{z^2} \approx \frac{0.2707 \mu_0 h M_s}{z^2} \quad (\text{C.8})$$

For our  $\text{Cr}_2\text{O}_3$  crystals, where  $M_s \approx 2 \mu_B/\text{nm}^2$ , and using  $z = 68 \text{ nm}$ , we find  $B_z/h \approx 1.4 \mu\text{T}/\text{nm}$ . For an rms surface roughness of  $3 \text{ nm-rms}$  we therefore expect stray field fluctuations of  $\sim 5 \mu\text{T}/\text{nm}$ , in good agreement with the experimental  $7 \mu\text{T-rms}$  (Fig. 7.2d).

## C.2.4 Fitting of line scans

We model the domain wall as presented in Eq. (7.1) in Chapter 7. The stray field is then computed via Eq. (5.4). The resulting model features 7 parameters: the effective surface magnetisation  $\sigma_z^0$ , the position of the domain wall  $x_0$ , its width parameter  $\Delta_{\text{DW}}$  and twist angle  $\chi$ , and the sensor geometry  $(z, \theta_{\text{NV}}, \phi_{\text{NV}})$ . Since  $z, \theta_{\text{NV}}, \phi_{\text{NV}}$  have been determined separately at this point, they are left fixed in the following least-squares optimisation, leaving only  $\sigma_z, x_0, \Delta_{\text{DW}}$  and  $\chi$  as free parameters.

The initial value of  $\sigma_z^0$  is determined by estimating the surface magnetisation using the two complementary methods (step height, integration of  $B_x$ ) described below. The initial value for width and chirality are set to  $\Delta_{\text{DW}} = 40 \text{ nm}$  and  $\chi = 90^\circ$ . We checked that other starting values did not significantly alter the fit results. The fitting procedure is repeated for each individual line scan.

## C.2.5 Complementary methods for estimating $\sigma_z^0$

We use two complementary methods for estimating the  $\text{Cr}_2\text{O}_3$  surface magnetisation  $\sigma_z^0$  from a stray field scans across domain walls:

*Step height in reconstructed  $\sigma_z$  map:* We reconstruct the surface magnetisation  $\sigma_z$  using Eq. (C.5). The step height at the domain wall is  $2\sigma_z^0$ .

*Integration of  $B_x$ :* As detailed in Section 5.2.3, the magnetisation across a domain wall can be estimated irrespective of the sample-to-sensor distance  $z$ , domain wall profile and chirality. We assume a domain wall extending along the  $y$  direction. We compute the  $B_x(x)$  component of the stray field from  $B_{\text{NV}}(x)$ , using the known orientation of the sensor  $(\theta_{\text{NV}}, \phi_{\text{NV}})$  and Eq. (5.35). According to Eq. (5.29), the surface magnetisation  $\sigma_z^0$  is given by the integral over  $B_x(x)$

$$\int_{-\infty}^{\infty} dx B(x) = \mu_0 M_z s = \mu_0 \sigma_z^0. \quad (\text{C.9})$$

### C.2.6 Complementary method for estimating $\Delta_{\text{DW}}$ and $\chi$

For a fixed pair  $(\chi, \Delta_{\text{DW}})$ , we only fit  $x_0$  to the data and record the residual sum of squares (RSS). The surface magnetisation is determined for each line scan by the previously introduced three complementary methods. The RSS is a measure of the likelihood. Indeed, assuming Gaussian errors, the log-likelihood is given by

$$\ln \mathcal{L} = \ln \left( \frac{1}{2\pi\sigma^2} \right) \frac{n}{2} - \frac{1}{2\sigma^2} \text{RSS} \quad (\text{C.10})$$

Here,  $\sigma$  is the standard deviation describing the error of a single data point, and  $n$  is the number of data points. We can compare the relative likelihood of two models 1 and 2 (*i.e.* two pairs of  $\Delta_{\text{DW}}$  and  $\chi$ ) by estimating  $\sigma_i^2 = \text{RSS}_i/n$ ,  $i \in \{1, 2\}$ , giving

$$\ln \mathcal{L}_1 - \ln \mathcal{L}_2 = -\frac{n}{2} \ln \frac{\text{RSS}_1}{\text{RSS}_2} \quad (\text{C.11})$$

We choose model 2 as the best model (*i.e.* the least squares solution), so that Eq. (C.11) is normalised to 0. To consider the data from all scans, we sum the RSS of each line and scan and set  $n$  to be the total number of data points.

## C.3 Supplementary Figures

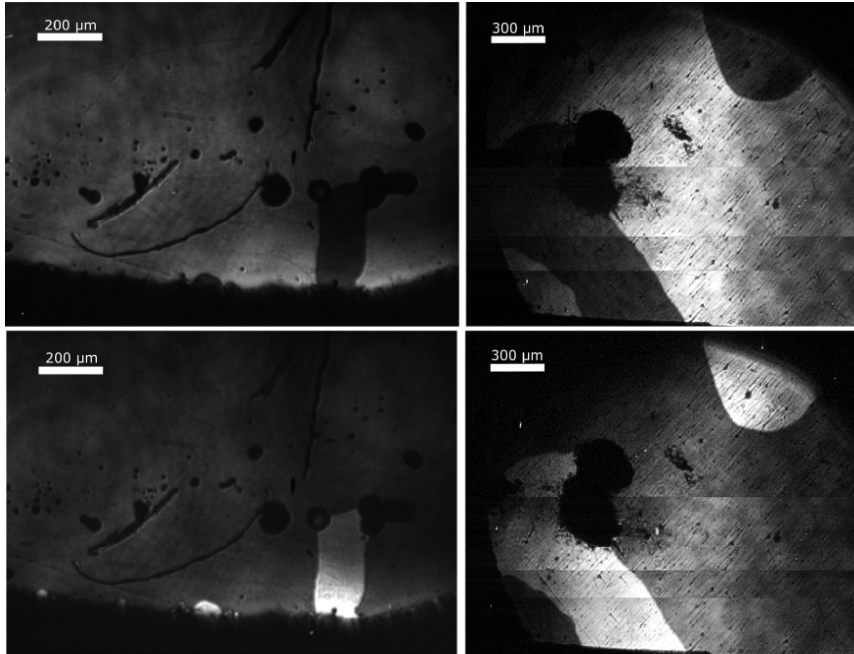


FIGURE C.1: SHG microscopy images of sample A (left panels) and sample B (right panels). Upper panels used left-handed circular polarisation, lower panels used right-handed circular polarisation.

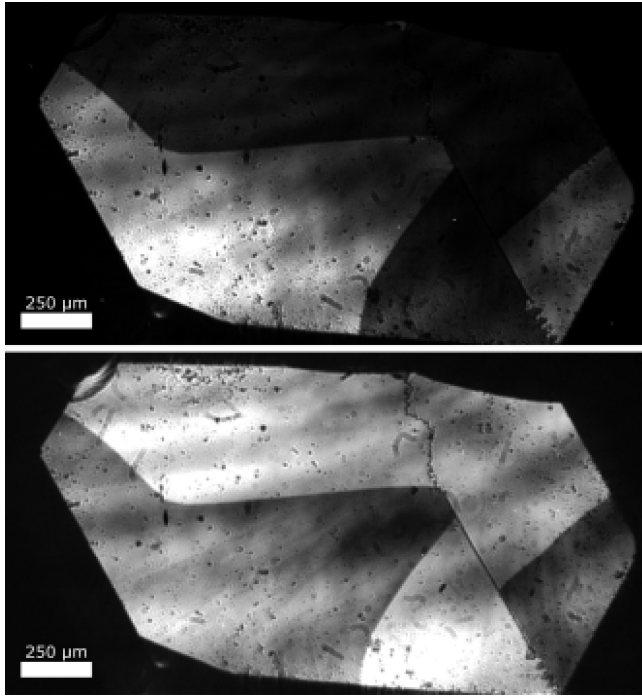


FIGURE C.2: **SHG microscopy images of sample C.** Upper panel used left-handed circular polarisation, lower panel used right-handed circular polarisation.

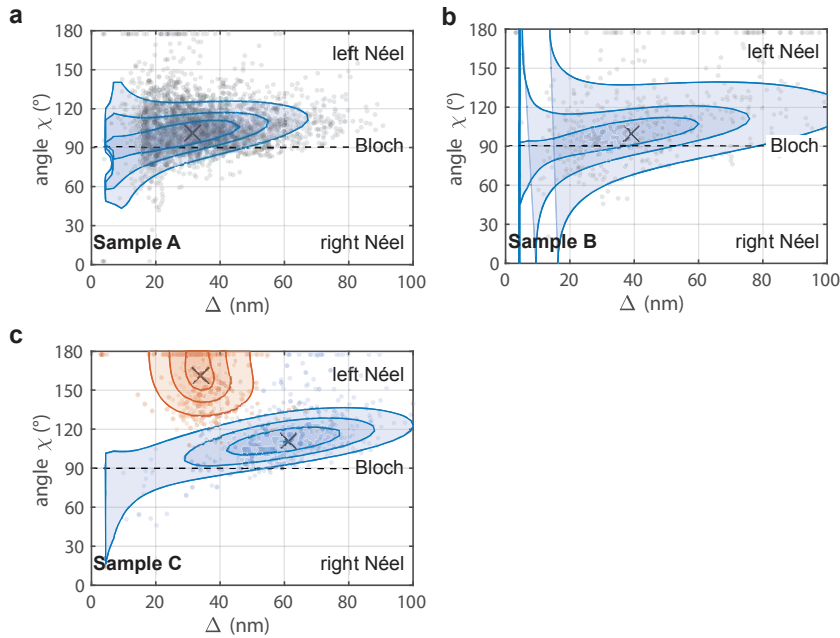


FIGURE C.3: **Maximum likelihood estimates for domain wall width  $\Delta_{DW}$  and twist angle  $\chi$ , as explained in the Appendix C.2.6.** Gray dots are fit results from individual line scans. Colored contours are maximum likelihood isolines containing 75%, 50%, and 25% of data-points. The most likely  $(\chi, \Delta_{DW})$  pair is indicated by a central cross. For sample C, datasets with  $\alpha > 9^\circ$  (blue) and  $\alpha < 9^\circ$  (red) are analysed separately.



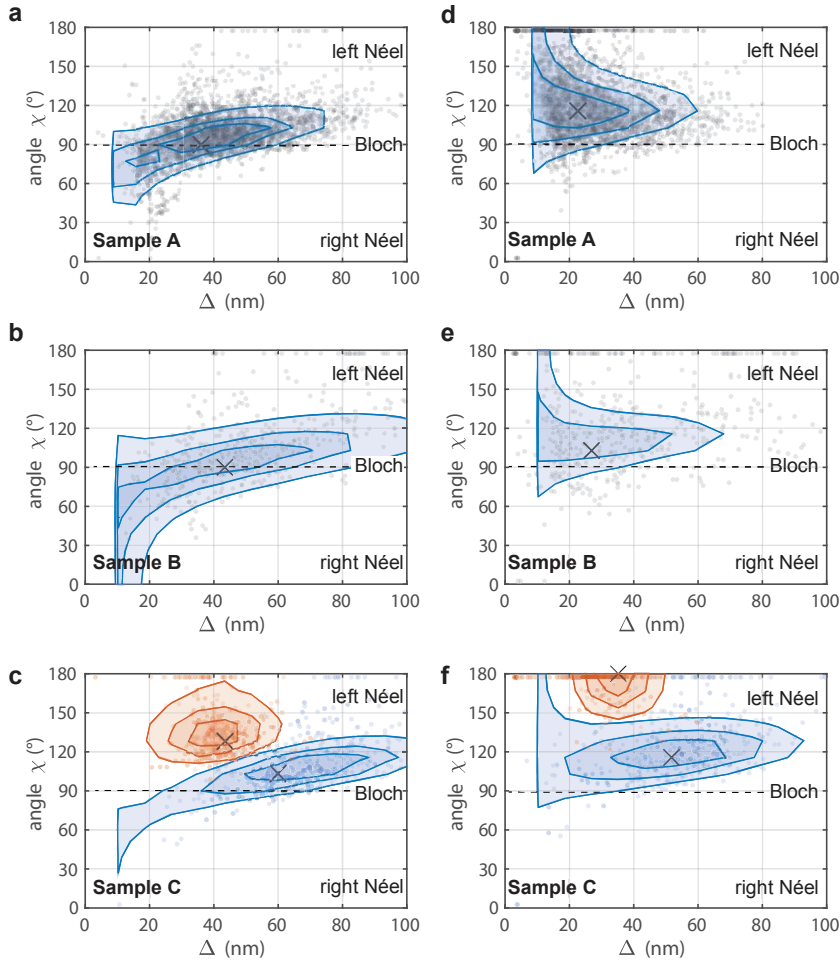


FIGURE C.4: **Maximum likelihood estimates for domain wall width  $\Delta_{DW}$  and twist angle  $\chi$  for upper and lower bound sample-to-sensor distances  $z \pm 10$  nm, where  $z$  is the calibrated sample-to-sensor distance. a-c, Maximum likelihood estimates for the lower bound  $z - 10$  nm. d-f, Maximum likelihood estimates for the upper bound  $z + 10$  nm. Data points, contours and central cross are as with Fig. C.3. We note that the our observation – the presence of Bloch-like walls in samples A and B, and mixed Bloch and Néel walls in sample C – is valid within the uncertainty of the sample-sensor distance. The  $z \pm 10$  nm bounds are a conservative estimate, as all probes showed a calibration error of  $\leq 8$  nm (see Appendix C.1.3).**





# Current-induced fragmentation of antiferromagnetic domains

## D.1 Samples

Tetragonal CuMnAs films were grown by molecular beam epitaxy at 210°C on GaP(001) substrates [196]. The films were protected by a 3-nm-thick Al capping layer to prevent oxidation of CuMnAs. The samples were patterned into four-arm cross-shaped devices using electron beam lithography and wet chemical etching.

## D.2 Nanoscale diamond magnetometry measurement - details

To investigate the domain pattern of CuMnAs, we use scanning NV magnetometry to image the local magnetic stray field  $B_{\text{NV}}(x, y)$  emanating from the domain walls, between adjacent domains. The scans are carried out on the NSDM microscope introduced in chapter 4 in ambient conditions using 532 nm laser light. The microscope employs monolithic diamond probe tips with single NV centres implanted at the apex (QZabre LLC, <https://qzabre.com/>). We apply a small magnetic bias field (2-4 mT) to obtain a sign-sensitive measurement of the magnetic stray field. By knowing the sign of the bias field the sign of the magnetic stray field can be deduced, see Section 5.3.1.  $\theta_{\text{NV}}$  and  $\phi_{\text{NV}}$  are the polar and azimuth angle of the NV spin symmetry axis in the laboratory frame of reference (see inset to Fig. 8.1b). The  $\theta_{\text{NV}}, \phi_{\text{NV}}$  angles and sample-to-sensor distance are calibrated beforehand as detailed in Appendix A. The magnetic stray field patterns shown in Figs. 8.1-8.2 have been low-pass filtered with a Gaussian filter ( $\sigma = 24\text{nm}$ ) to better highlight the morphology.

We quantify the amplitude of the magnetic stray field pattern by taking the root mean square of  $B_{\text{NV}}(x, y)$  over the entire magnetic field map

$$B_{\text{rms}} = \sqrt{\frac{1}{n} \sum_{i=1}^n (B_{\text{NV}}^i)^2}, \quad (\text{D.1})$$

where the index  $i$  enumerates the pixels. The uncertainty of  $B_{\text{rms}}$  is estimated via jackknife resampling[210]. For this, we repeatedly compute the RMS value, each time leaving out one single point from the dataset. The uncertainty can then be

inferred from the spread of these values. Let  $x_i$  be the RMS value when omitting the  $i$ -th data point, and let  $x$  be their mean. The estimated uncertainty of the RMS of the complete dataset is

$$\Delta B_{\text{rms}} = \sqrt{\frac{n-1}{n} \sum_{i=1}^n (x_i - x)^2}. \quad (\text{D.2})$$

### D.3 Surface magnetisation in CuMnAs

As detailed in Section 5.1.4, the surface magnetisation of each sublayer is given by

$$m_s = sM_s = \frac{snm}{V}. \quad (\text{D.3})$$

For tetragonal CuMnAs,  $s = c/3 = 0.21$  nm,  $n = 1$ ,  $m \approx 3.6 \mu_B$  (Ref. [211]),  $V = a^2c = 0.091$  nm<sup>3</sup>,  $a = b = 0.31$  nm, and  $c = 0.63$  nm, resulting in  $M_s = 3.62 \times 10^5$  A m<sup>-1</sup> and  $m_s = 8.2 \mu_B/\text{nm}^2$ .

### D.4 Reconstruction of the domain pattern

In the Subsection 5.2.2 we have introduced a recipe to give a best estimate for the in-plane magnetisation assuming that (i) the vector length is constant,  $|\vec{M}_{\parallel}(x, y)| = M_s$ , and (ii) that the antiferromagnet is uniaxial with a single domain orientation (e.g.,  $\pm x$ ). Both assumptions are expected to be valid for  $t < 50$  nm films in tetragonal CuMnAs. In Fig. D.1 we show the error variance  $\epsilon$  depending on  $M_s$  and  $\alpha$  for Fig. 8.1c using steps 1-7. We find a most likely orientation of  $\alpha = 82^\circ$ , that is, the uniaxial direction is approximately along  $\pm y$ . The most likely magnetisation is  $m_s = 4.3 \mu_B/\text{nm}^2$ . This value of  $m_s$  is less than half the value calculated in Appendix D.3 for an ideal CuMnAs film. Such a discrepancy is expected when considering that the domain wall width is actually finite, which results in a smaller magnetic stray field compared to the zero width walls assumed in our model. The bandpass filtering used in the reconstruction, as well as surface effects, can also lead to a reduction in  $m_s$ . Additionally, according to Section 7.4.3 and Ref. [76] the surface magnetization reduces towards the Néel point (485 K) approximately by  $m_s(T) = m_s(0)[1 - (T/T_N)]^{0.35}$ , which gives  $m_s(295 \text{ K}) = 5.9 \mu_B/\text{nm}^2$ . Finely broken-up domains, which are too small to be resolved by the NV sensor can also reduce the stray field resulting in an underestimated  $m_s$ .

### D.5 Ferromagnetic defects

### D.6 Measurement of the current density distribution

We measure the current density distribution in the microdevices following Ref. [33]. We modulate the current at 2.5 kHz with a square wave centred on 0 mA. The magnetic field is recorded synchronously with the modulation. The current-induced Oersted field given by

$$B_{\text{Oersted}}(x, y) = \frac{B_{\text{NV}}^+(x, y) - B_{\text{NV}}^-(x, y)}{2}, \quad (\text{D.4})$$

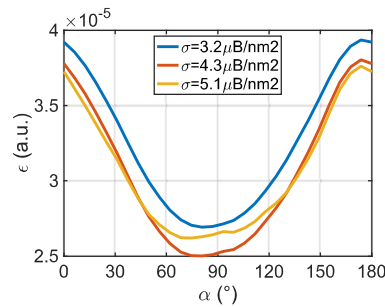


FIGURE D.1: **Error variance for reconstruction of domain pattern in Fig. 1d.** Error variance  $\epsilon$  for different  $m_s$  depending on angle  $\alpha$  between the uniaxial anisotropy axis and the  $x$ -axis. The most likely values are  $m_s = 4.3 \mu_B/\text{nm}^2$  and  $\alpha = 82^\circ$ .

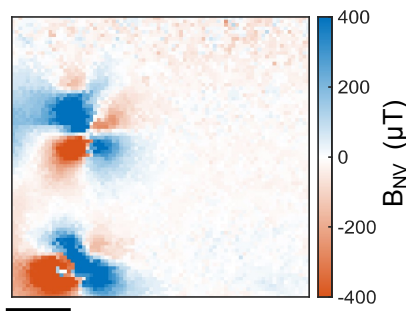


FIGURE D.2: **Magnetic field of on CuMnAs ( $t = 30 \text{ nm}$ ) showing ferromagnetic patches.** The stray field amplitude of the ferromagnetic patches is of order  $\sim 1 \text{ mT}$ , roughly 10 times larger compared to the stray field emanating from the antiferromagnetic domain pattern. Sensor parameters are ( $z = 65 \pm 8 \text{ nm}$ ,  $\phi_{\text{NV}} = 280 \pm 5^\circ$ ,  $\theta_{\text{NV}} = 55^\circ$ ). Scale bar, 400 nm.

where  $B_{\text{NV}}^+$  and  $B_{\text{NV}}^-$  denote the field measured with either current polarity. This differential measurement scheme naturally suppresses any static signals (residual fields, electric or thermal drifts).

Assuming that the current density is homogeneous throughout the film thickness, we can reconstruct the two-dimensional current density  $\vec{J}(x, y) = (J_x, J_y)$  by inverting Biot and Savart's law, following the procedure described in Ref. [33].

## D.7 Simulation of fragmentation

In this section, we estimate the domain wall density of the pristine and fragmented state shown in Figs 8.3 and D.4 by reconstructing the magnetisation patterns from the magnetic stray field maps.

### D.7.1 Simulation of the domain pattern using image to image translation

The reconstruction of the magnetisation pattern from a magnetic stray is generally ambiguous, see Section 5.2. In order to find one possible solution or best match of the magnetisation pattern we use conditional adversarial networks applying the

method and code provided in Ref. [186]. Conditional adversarial networks are commonly used for image to image translation. Examples include the transformation of sketches to photos and black white images to colour photos. These networks not only learn the mapping from the input to the output image but also learn a loss function to train the image to image translation enabling a generic approach to many problems which otherwise require tailored loss formulation. The network trains a generator  $G$  to map a source input image  $x$  to a target output image  $y$ :  $G : x \rightarrow y$ , where  $x, y$  are matrices of dimension  $3 \times 256 \times 256$ , with the three layers of the matrix corresponding to the RGB colours of the images. The training set consists of image pairs, for example, the sketch of the shoe and a photo of the corresponding shoe. Adapting the methods of an image to image translation using conditional adversarial networks, we replace the RGB colours with the three-vector components of the magnetic field  $\vec{B}$  and the magnetisation  $\vec{M}$ . The network is trained on pairs of images of the magnetic stray field  $\vec{B}$  and corresponding magnetisation pattern  $\vec{M}_{\text{true}}$  which we generate beforehand, see below. We verify the training progress by calculating the loss function  $L_1 = \sum_{i=1}^n |\vec{M}_{\text{true}} - \vec{M}_{\text{pred}}|$ , where  $i$  runs over all entries in the matrices and  $\vec{M}_{\text{true}}, \vec{M}_{\text{pred}}$  is the ground truth and predicted output image, respectively, see Fig. D.3. Note, that the training progress is monitored by an independent data set not included in the training data set.

In Figure D.3 we illustrate the workflow of the reconstruction of the magnetisation pattern. In a last step, we cross check the performance of the network by calculating the magnetic stray field  $\vec{B}_{\text{calc}}$  from the magnetisation pattern  $\vec{M}_{\text{pred}} = G(\vec{B})$  using Eq. (5.4) and compare it to the input image  $\vec{B}$ . Naturally, using the approach described above, the reconstruction of the magnetisation pattern from the magnetic stray field crucially depends on the underlying model of the training set, which we describe in Section D.7.2. Compared to the reconstruction method introduced in Subsection 5.2.2 which assumes sharp domain walls and an uniaxial anisotropy, the reconstruction technique described above can be easily applied to domain pattern with a finite domain wall width and even more complicated models without an uniaxial anisotropy. At this point we emphasise again that the reconstruction depends on the underlying model of the training data set, i.e. domain wall width, uniaxial anisotropy, etc., and only provides a possible solution that does not need to be unambiguous.

### D.7.2 Generation of the domain pattern and corresponding magnetic stray field

We create a domain pattern consisting of domain walls with a finite width by generating a 2D array of normally distributed random numbers. We then spectrally limit the pattern by applying a Gaussian smoothing. The reduction in detail depends on the standard deviation entering the Gaussian distribution. Taking the sign of the 2D array results in a domain pattern. In our model, we include domain walls with a finite domain wall width  $\Delta_{\text{DW}}$ . We assume that the reorientation of the Néel vector between adjacent domains follows a hyperbolic tangent profile [141]. The hyperbolic tangent profile is inserted by convolving the domain pattern with the function  $1/\cosh(x/\Delta_{\text{DW}})$ . Further, we constrain the magnetic moments to rotate in-plane between adjacent domains, i.e. we only consider Néel type domain walls [13]. We do not impose a preferred chirality of the Néel type domain wall. The domain wall width has been measured by XMLD-PEEM and is 75 nm and 90 nm for 30 nm and 50 nm thick CuMnAs samples, respectively [212]. We simulate fragmentation for

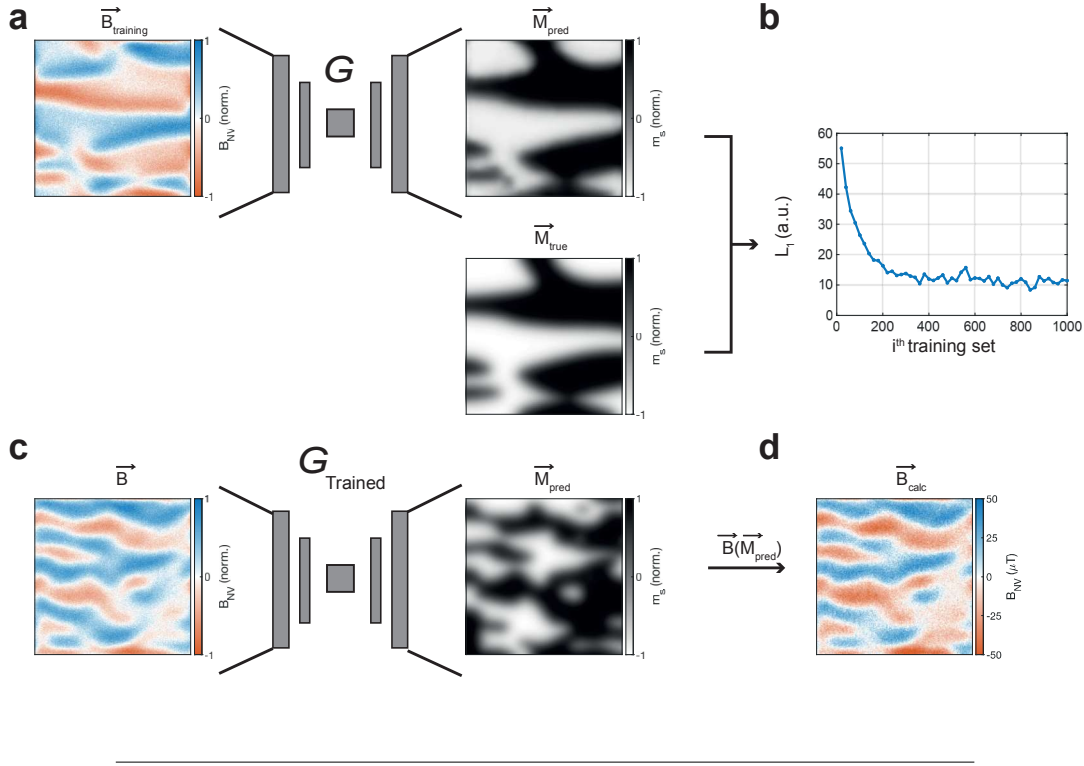


FIGURE D.3: **Reconstruction of the domain pattern using image to image translation.** **a**, The conditional adversarial network  $G$  is trained by pairs of magnetic stray field maps ( $\vec{B}_{\text{training}}$ ) and corresponding magnetisation map ( $\vec{M}_{\text{true}}$ ). **b**, The loss function  $L_1 = \sum_{i=1}^n |\vec{M}_{\text{true}} - \vec{M}_{\text{pred}}|$  monitors the training progress. **c**, The trained network  $G_{\text{trained}}$  estimates the magnetisation pattern  $\vec{M}_{\text{pred}}$  from the magnetic stray field map  $\vec{B}$ . **d**, We cross-check the performance of the network by calculating the magnetic stray field map  $\vec{B}_{\text{calc}}$  from the predicted magnetisation pattern  $\vec{M}_{\text{pred}}$  using Eq. (5.4). Note that we show here only the projection of the magnetic stray field map  $\vec{B}$  onto the NV centre's symmetry axis  $B_{\text{NV}}$  and the  $y$ -component  $m_s$  of the magnetisation pattern  $\vec{M}$ .

thin samples where we assume an uniaxial domain pattern, *i.e.*, the magnetic moments inside the domains can only align along the  $y$ -axis. We train the network, described in Appendix D.7.1, on 1800 pairs of normalised magnetic fields and magnetisation pattern. We scale the magnetisation to match the magnetic contrast and find  $m_s = 4.3$  and  $5.1 \mu_B/\text{nm}^2$  for 30 and 50 nm, respectively. As discussed in the Appendix D.4, deviations from the theoretical value of  $m_s = 5.9 \mu_B/\text{nm}^2$  are due to details in the magnetisation pattern which are below the spatial resolution limit or statistical errors, such as an underestimated sample-sensor distance. We add  $8 \mu\text{T}$  of Gaussian noise to the simulated  $B_{\text{rms}}$  to account for the measurement uncertainty of the NV magnetometer.

### D.7.3 Introduction of fragmentation and domain wall density

We introduce fragmentation by inverting islands of magnetic moments at random positions in the domain pattern. We vary both, the size and the number of islands and compare the magnetic contrast to the experimental data. To preserve the morphology of the pristine pattern in the fragmented one, the maximum size of the islands must be kept below a certain value which depends also on the number of

islands. For instance, for the simulation presented in Fig. 8.4c,d, the maximum size of the islands is  $5 \times 5$  nm. The size of the islands for 50 nm thick CuMnAs and the data presented in Fig. D.4 can reach up to  $30 \times 30$  nm. At this point, we only give an upper bound for the size of the islands. Larger islands combined with the huge number of islands required to explain the reduction of  $B_{\text{rms}}$  would lead to a clustering of islands visible in the magnetic stray field map. Finally, we gauge the domain wall density by counting the number of domain walls crossing a large number of paths parallel to the current flow in a given area and normalising it to that area.

Comments to the simulation: As the magnetisation pattern is not unique and depends on the underlying model, i.e. domain wall width,  $m_s$  and the type of fragmentation, for instance, the size of the islands, the values for the domain wall densities have to be treated with caution.

## D.8 Current induced fragmentation on 50 nm thick CuMnAs

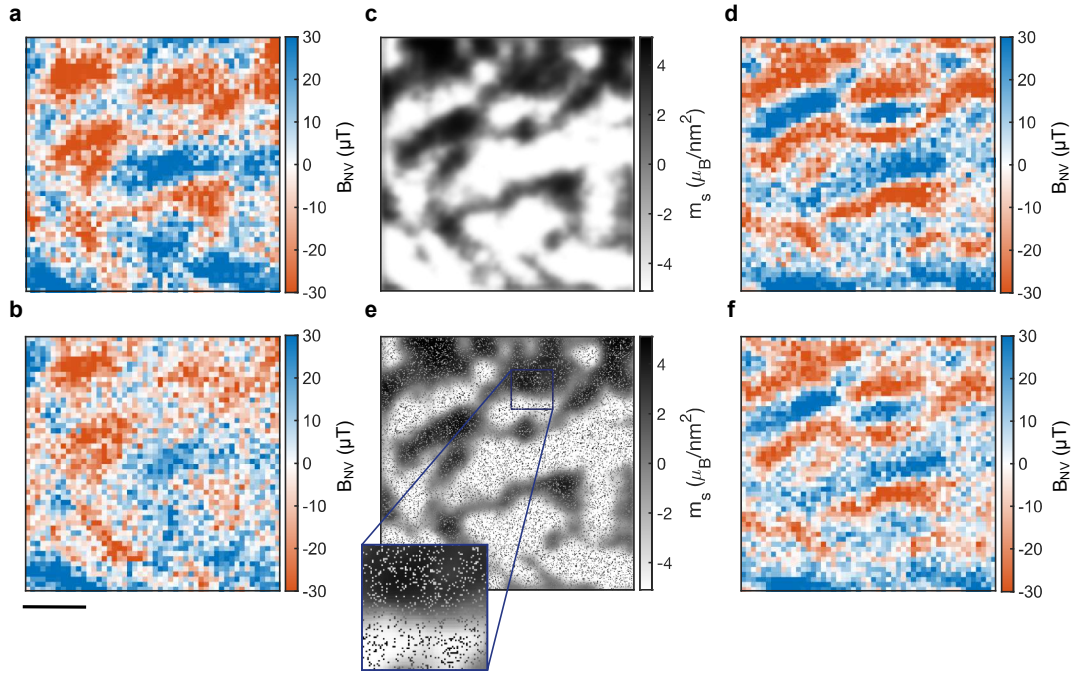


FIGURE D.4: **Current induced fragmentation in the magnetic texture.** **a,b** Magnetic stray field images of a 50-nm thick CuMnAs sample. The scans correspond to the pristine, fragmented state in Fig. 8.5, respectively. **c,d** Simulation of the domain pattern and resulting magnetic stray field map (d), showing best resemblance with the experimental data in a and amplitude  $B_{\text{rms}}$ . The domain wall width  $\Delta_{\text{DW}}$  is set to 90 nm. Details on the simulation are given in the Appendix D.7. **e,f** Same as c,d upon introducing fragmentation. For that, we flip islands of size  $5 \text{ nm} \times 5 \text{ nm}$  in the magnetic texture and increase the number of islands until the  $B_{\text{rms}}$  in b is reached. The magnification highlights the disorder. Scale bar is 500  $\mu\text{m}$ .



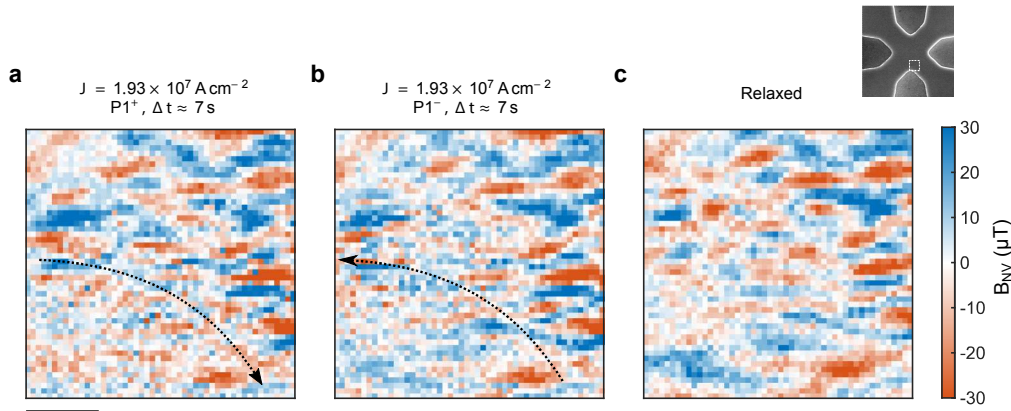


FIGURE D.5: **Non-uniform fragmentation and polarity switching.** **a,b** Magnetic stray field images of a 30-nm thick CuMnAs sample. The scans are located in the lower corner of the cross, see inset. For each pixel  $(i, j)$ , the magnetic stray field is measured after applying a pulse  $P1^+$  (panel a) and after applying an opposite-polarity pulse ( $P1^-$ , panel b) of amplitude  $J = 1.93 \times 10^7 \text{ Acm}^{-2}$ . The duration of a pulse is  $100 \mu\text{s}$ . The stray field measurement starts immediately after a pulse and is integrated over 7s. The sequence is repeated for each pixel in the image. Black arrows illustrate the current flow. **c** Magnetic stray field image recorded 1 h after the last pulse. The NV sensor parameters are ( $z = 52 \pm 11 \text{ nm}$ ,  $\phi_{\text{NV}} = 88 \pm 5^\circ$ ,  $\theta_{\text{NV}} = 55$ ). Scale bar, 400nm.

## D.9 Coexistence of non-uniform fragmentation and $180^\circ$ Néel vector switching

Fig. D.5 shows a second dataset acquired using the repetitive re-excitation scheme introduced in Fig. 8.3. The three images consist of  $50 \times 50$  pixels and are recorded after  $P1^+$  pulses (Fig. D.5a),  $P1^-$  pulses (Fig. D.5b), and in the relaxed state one hour after the last pulse (Fig. D.5c). The average current density was  $J = 1.93 \times 10^7 \text{ Acm}^{-2}$ .

We observe a striking reduction of the intensity of the magnetic stray field in the bottom left corner with the highest pulsing current density. On the other hand, the upper and right sides of the image receive lower current densities, and the magnetic contrast increases showing the non-uniformity of fragmentation. To highlight that the domain fragmentation is a transient effect, we show in Fig. D.5c the stray field map in the relaxed state, acquired 1 h after the last writing pulse. We observe that the stray field amplitude increases, especially in the bottom left corner. We also note that some regions of the bottom-left corner of images in Figs. D.5a,b show an opposite sign for the opposite pulsing polarities. This observation indicates that the domain fragmentation can coexist with a  $180^\circ$  Néel vector reorientation in the domains in the studied 30-nm-thick uniaxial film.

## D.10 Stray field amplitude from atomic steps

Atomic steps in the topography of the magnetic thin film generate a stray field. The CuMnAs film, as grown, is known to always terminate in a complete magnetic unit cell [196]. The surface never cleaves in between the Mn planes. This crucially reduces the stray field from steps, as the antiferromagnetic pairing is preserved, and no uncompensated spins are found on the surface.

We estimate the strength of this stray field by following the calculations in Ref. [36] and Subsection C.2.3. In the following, we exclusively look at the  $z$ -component of the produced stray field. According to Eq. (5.4) with Eq. (5.12), the stray field from a single antiferromagnetic film assuming  $M_z = 0$  is given by

$$B_{z,af} = i \frac{1}{2} \mu_0 K s (1 - e^{-Kt}) e^{-Kz} M_k, \quad (\text{D.5})$$

with  $M_k = \vec{K} \cdot \vec{M} / K$ . The stray field of a step  $h$  corresponds to the differential field of two layers [36], one located at  $z$  and of thickness  $t$ , the other located at  $z + h$  and of thickness  $t - h$ , see Fig. D.6. Evaluating this difference, to first order, yields

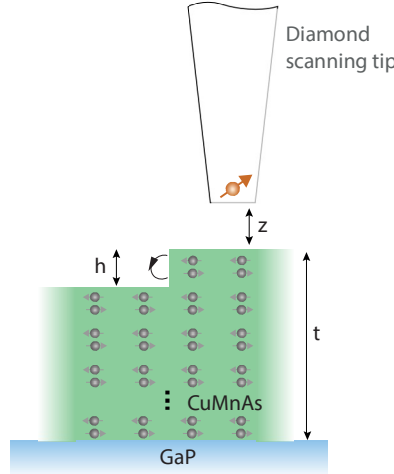


FIGURE D.6: **Model of the CuMnAs surface steps.** The surface terminates with complete magnetic unit cells. Weak magnetic fields, shown as black arrow, are expected at topographic steps. The diamond tip is scanned at constant height  $z$  over the sample surface.

$$B_{z,step} = i \frac{1}{2} \mu_0 K s K h e^{-Kz} M_k = i \frac{1}{2} \mu_0 K^2 s h e^{-Kz} M_k. \quad (\text{D.6})$$

As expected, we see that the thickness of the film does not enter this expression. In order to gauge the order of magnitude of this field, we maximise the expression with respect to  $K$ . This corresponds to finding the Fourier component that produces the greatest stray field at the location of the sensor. This maximum is reached for  $K = 2/z$ , corresponding to a real-space length scale of  $\pi/K \approx 100\text{nm}$ . This is in the same order of magnitude as the actual size of atomically flat islands on our samples, which was found to be  $\sim 200\text{nm}$  by atomic force microscopy (Figure 2 in Ref. [196]). Consequently, the NV center is well sensitive to the stray fields from atomic steps.



Inserting the above expression for  $K$  and  $z = 60\text{nm}$ , we find

$$|B_{z,\text{step}}| \sim \frac{\mu_0 h s M_s}{19 \times 10^3 \text{nm}^2} = 3 \mu\text{T}. \quad (\text{D.7})$$

In the last step, we used  $h = 0.64\text{nm}$  (see Ref. [196]) and  $s = 0.21\text{nm}$ . The value holds for a single atomic step. The stray field increases linearly with increasing surface roughness. As our CuMnAs samples are largely atomically flat, this effect is weak compared to the measured values of  $B_{\text{NV}}$  (typically 20 to 60  $\mu\text{T}$ ), and we conclude that the stray field contributed by the surface roughness is negligible.

## D.11 Temperature evolution in the cross-device during a typical writing pulse

The simulation and resistance measurement have been performed by Z. Kašpar and K. Olejník.

We combine 2-point resistance measurement and COMSOL Multiphysics<sup>®</sup> modelling to estimate the temperature increase during a typical writing pulse of amplitude  $1.5 \times 10^7 \text{A/cm}^2$ . In Figure D.7a, we first measure the temperature dependency of the resistivity. In Figure D.7b, we record the time evolution of the 2-point resistance (black) during a 100  $\mu\text{s}$  pulse and compare it to COMSOL simulation (red). The COMSOL simulation includes full 3D model of the CuMnAs cross structure on top of a 350  $\mu\text{m}$  thick GaP substrate. In the simulation we used the experimental temperature dependency of resistivity, shown in Fig. D.7a, and the following thermal parameters: GaP heat capacity  $430 \text{J kg}^{-1} \text{K}^{-1}$ , GaP heat conductivity  $75 \text{W m}^{-1} \text{K}^{-1}$ , CuMnAs heat capacity  $300 \text{J kg}^{-1} \text{K}^{-1}$ , CuMnAs heat conductivity  $7.3 \text{W m}^{-1} \text{K}^{-1}$ . We note that the values for CuMnAs are only estimated, nevertheless simulations are not sensitive to these parameters since the thermal dynamics in time scales above microseconds are completely dominated by heat transport in the substrate [213]. From the good agreement between the experimentally measured 2-point resistance during the writing pulse (black) and the result of COMSOL model (red) we can extract reasonably precise values of temperature in the device. In Figure D.7c, the time evolution of the temperature, obtained from the COMSOL simulation, is shown. As is apparent from the 2D temperature map in Fig. D.7d, the temperature varies across the sample and heats over the Néel point ( $T_{\text{N}} \approx 485 \text{K}$ ) mainly at the corners.

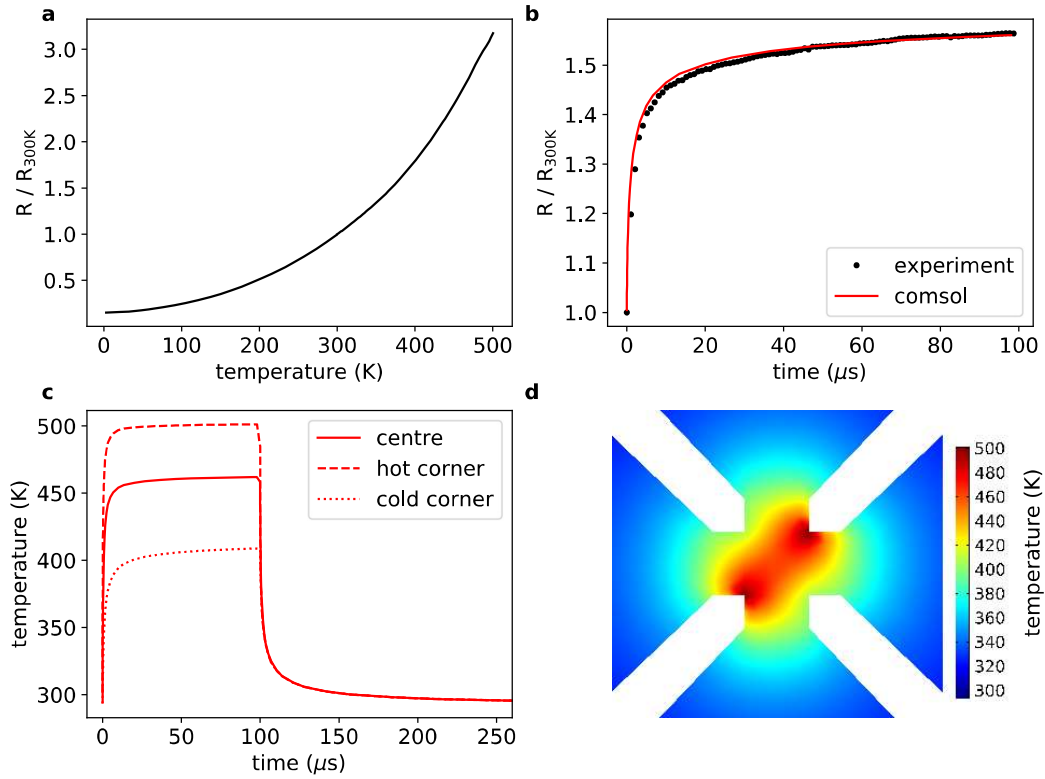


FIGURE D.7: **Analysis of the temperature evolution in the cross-device during a typical writing pulse.** **a**, Dependence of the resistivity on the base temperature normalised to the resistivity at 300 K. **b**, Experimentally measured 2-point resistance of the  $10\ \mu\text{m}$  cross structure ( $50\ \text{nm}$  CuMnAs film grown on GaP substrate) during a  $100\ \mu\text{s}$  writing pulse with current density  $1.5 \times 10^7\ \text{A}/\text{cm}^2$  (black) compared to the COMSOL simulation (red), for details see text. **c**, Time evolution of the temperature during the writing pulse obtained by the COMSOL simulation with the plotted curves corresponding to the corner of the cross with the highest current density, to the centre of the cross, and to the corner with the lowest current density during the pulse. **d**, COMSOL simulation of the temperature reached at the end of the writing pulse plotted as a 2D map across the device structure.

# Bibliography

- [1] T. Jungwirth et al. “Antiferromagnetic spintronics”. In: *Nature nanotechnology* 11.3 (2016), pp. 231–241.
- [2] L. Néel. “Magnetism and the local molecular field. Vol”. In: *Nobel Lectures, vol. Physics 1970* (1963), pp. 318–341.
- [3] B. Hudec et al. “3D resistive RAM cell design for high-density storage class memory review”. In: *Science China Information Sciences* 59.6 (2016), p. 061403.
- [4] C. Chappert, A. Fert, and F. N. Van Dau. “The emergence of spin electronics in data storage”. In: *Nanoscience And Technology: A Collection of Reviews from Nature Journals*. World Scientific, 2010, pp. 147–157.
- [5] B. Dieny et al. “Opportunities and challenges for spintronics in the microelectronics industry”. In: *Nature Electronics* 3.8 (2020), pp. 446–459.
- [6] T. Jungwirth et al. “The multiple directions of antiferromagnetic spintronics”. In: *Nature Physics* 14.3 (2018), pp. 200–203.
- [7] P. Wadley et al. “Electrical switching of an antiferromagnet”. In: *Science* 351.6273 (2016), pp. 587–590.
- [8] Z. Kašpar et al. “Quenching of an antiferromagnet into high resistivity states using electrical or ultrashort optical pulses”. In: *Nature Electronics* (2020), pp. 1–8.
- [9] A. Churikova et al. “Non-magnetic origin of spin Hall magnetoresistance-like signals in Pt films and epitaxial NiO/Pt bilayers”. In: *Applied Physics Letters* 116.2 (2020), p. 022410.
- [10] C. Chiang et al. “Absence of evidence of electrical switching of the antiferromagnetic Néel vector”. In: *Physical Review Letters* 123.22 (2019), p. 227203.
- [11] T. Matalla-Wagner et al. “Resistive contribution in electrical-switching experiments with antiferromagnets”. In: *Physical Review Research* 2.3 (2020), p. 033077.
- [12] P. Zhang et al. “Quantitative Study on Current-Induced Effect in an Antiferromagnet Insulator/Pt Bilayer Film”. In: *Physical Review Letters* 123.24 (2019), p. 247206.
- [13] P. Wadley et al. “Current polarity-dependent manipulation of antiferromagnetic domains”. In: *Nature nanotechnology* 13.5 (2018), pp. 362–365.
- [14] J. Godinho et al. “Electrically induced and detected Néel vector reversal in a collinear antiferromagnet”. In: *Nature communications* 9.1 (2018), pp. 1–8.
- [15] M. Meinert, D. Graulich, and T. Matalla-Wagner. “Electrical switching of antiferromagnetic Mn<sub>2</sub>Au and the role of thermal activation”. In: *Physical Review Applied* 9.6 (2018), p. 064040.
- [16] S.-W. Cheong et al. “Seeing is believing: visualization of antiferromagnetic domains”. In: *npj Quantum Materials* 5.1 (2020), pp. 1–10.

- [17] T. Shiino et al. "Antiferromagnetic domain wall motion driven by spin-orbit torques". In: *Physical review letters* 117.8 (2016), p. 087203.
- [18] M. Bode et al. "Atomic spin structure of antiferromagnetic domain walls". In: *Nature materials* 5.6 (2006), pp. 477–481.
- [19] N. B. Weber et al. "Magnetostrictive Domain Walls in Antiferromagnetic NiO". In: *Phys. Rev. Lett.* 91 (23 2003), p. 237205.
- [20] R Ravlić et al. "Correlation of dislocation and domain structure of Cr(001) investigated by spin-polarized scanning tunneling microscopy". In: *Physical Review B* 67.17 (2003), p. 174411.
- [21] C. L. Degen, F Reinhard, and P. Cappellaro. "Quantum sensing". In: *Reviews of modern physics* 89.3 (2017), p. 035002.
- [22] C. L. Degen. "Scanning magnetic field microscope with a diamond single-spin sensor". In: *Appl. Phys. Lett.* 92, 243111 (2008), p. 243111.
- [23] G. Balasubramanian et al. "Nanoscale imaging magnetometry with diamond spins under ambient conditions". In: *Nature* 455, 648 (2008), p. 648.
- [24] J. Taylor et al. "High-sensitivity diamond magnetometer with nanoscale resolution". In: *Nature Physics* 4.10 (2008), pp. 810–816.
- [25] J. P. Tetienne et al. "The nature of domain walls in ultrathin ferromagnets revealed by scanning nanomagnetometry". In: *Nat. Commun.* 6 (2015), p. 6733.
- [26] M. Pelliccione et al. "Scanned probe imaging of nanoscale magnetism at cryogenic temperatures with a single-spin quantum sensor". In: *Nature nanotechnology* 11.8 (2016), pp. 700–705.
- [27] L. Thiel et al. "Quantitative nanoscale vortex imaging using a cryogenic quantum magnetometer". In: *Nature nanotechnology* 11.8 (2016), pp. 677–681.
- [28] D. Schmid-Lorch et al. "Relaxometry and dephasing imaging of superparamagnetic magnetite nanoparticles using a single qubit". In: *Nano letters* 15.8 (2015), pp. 4942–4947.
- [29] A. Hrabec et al. "Current-induced skyrmion generation and dynamics in symmetric bilayers". In: *Nature communications* 8.1 (2017), pp. 1–6.
- [30] Y Dovzhenko et al. "Magnetostatic twists in room-temperature skyrmions explored by nitrogen-vacancy center spin texture reconstruction". In: *Nature communications* 9.1 (2018), pp. 1–7.
- [31] T. Van der Sar et al. "Nanometre-scale probing of spin waves using single electron spins". In: *Nature communications* 6.1 (2015), pp. 1–8.
- [32] A. Dussaux et al. "Local dynamics of topological magnetic defects in the itinerant helimagnet FeGe". In: *Nature Communications* 7 (2016), p. 12430.
- [33] K Chang et al. "Nanoscale imaging of current density with a single-spin magnetometer". In: *Nano letters* 17.4 (2017), pp. 2367–2373.
- [34] I. Gross et al. "Real-space imaging of non-collinear antiferromagnetic order with a single-spin magnetometer". In: *Nature* 549.7671 (2017), pp. 252–256.
- [35] M. Wörnle et al. "Current-induced fragmentation of antiferromagnetic domains". In: *arXiv preprint arXiv:1912.05287* (2019).
- [36] M. S. Wörnle et al. "Coexistence of Bloch and Néel walls in a collinear antiferromagnet". In: *Phys. Rev. B* 103 (9 2021), p. 094426.

- [37] P. Appel et al. "Nanomagnetism of magnetoelectric granular thin-film anti-ferromagnets". In: *Nano letters* 19.3 (2019), pp. 1682–1687.
- [38] T. Kosub et al. "Purely antiferromagnetic magnetoelectric random access memory". In: *Nature communications* 8.1 (2017), pp. 1–7.
- [39] S. Vélez et al. "High-speed domain wall racetracks in a magnetic insulator". In: *Nature communications* 10.1 (2019), pp. 1–8.
- [40] S. Blundell. *Magnetism in condensed matter*. 2003.
- [41] J. M. Coey. *Magnetism and magnetic materials*. Cambridge university press, 2010.
- [42] A. Hubert and R. Schäfer. *Magnetic domains: the analysis of magnetic microstructures*. Springer Science & Business Media, 2008.
- [43] I. Dzyaloshinsky. "A thermodynamic theory of weak ferromagnetism of anti-ferromagnetics". In: *Journal of Physics and Chemistry of Solids* 4.4 (1958), pp. 241–255. ISSN: 0022-3697.
- [44] T. Moriya. "Anisotropic Superexchange Interaction and Weak Ferromagnetism". In: *Phys. Rev.* 120.1 (Oct. 1960), pp. 91–.
- [45] A. Crépieux and C. Lacroix. "Dzyaloshinsky–Moriya interactions induced by symmetry breaking at a surface". In: *Journal of magnetism and magnetic materials* 182.3 (1998), pp. 341–349.
- [46] A. Fert. "Magnetic and Transport Properties of Metallic Multilayers". In: *Metallic Multilayers*. Vol. 59. Materials Science Forum. Trans Tech Publications Ltd, Jan. 1991, pp. 439–480.
- [47] A. Bogdanov and U. Rößler. "Chiral symmetry breaking in magnetic thin films and multilayers". In: *Physical review letters* 87.3 (2001), p. 037203.
- [48] S. Velez et al. "High-speed domain wall racetracks in a magnetic insulator". In: *arXiv:1902.05639* (2019).
- [49] M. Fiebig. "Nichtlineare Spektroskopie und Topografie an antiferromagnetischen Domänen". In: *PhD Thesis* (1996).
- [50] M. Fiebig, T. Lottermoser, and R. V. Pisarev. "Spin-rotation phenomena and magnetic phase diagrams of hexagonal  $\text{RMnO}_3$ ". In: *Journal of applied physics* 93.10 (2003), pp. 8194–8196.
- [51] J. Stöhr and H. C. Siegmann. "Magnetism". In: *Solid-State Sciences*. Springer, Berlin, Heidelberg 5 (2006).
- [52] H. Gomonay and V. M. Loktev. "Magnetostriction and magnetoelastic domains in antiferromagnets". In: *Journal of Physics: Condensed Matter* 14.15 (2002), p. 3959.
- [53] H. V. Gomonay and V. M. Loktev. "Shape-induced phenomena in finite-size antiferromagnets". In: *Physical Review B* 75.17 (2007), p. 174439.
- [54] N. Weber et al. "Magnetostrictive domain walls in antiferromagnetic  $\text{NiO}$ ". In: *Physical review letters* 91.23 (2003), p. 237205.
- [55] A. Malozemoff and J. Slonczewski. *Magnetic Domain Walls in Bubble Materials: Advances in Materials and Device Research*. Vol. 1. Academic press, 2016.
- [56] E. Gyorgy and F. Hagedorn. "Analysis of Domain-Wall Motion in Canted Antiferromagnets". In: *Journal of Applied Physics* 39.1 (1968), pp. 88–90.

- [57] N Papanicolaou. "Antiferromagnetic domain walls". In: *Physical Review B* 51.21 (1995), p. 15062.
- [58] C. Mitsumata and A. Sakuma. "Generalized model of antiferromagnetic domain wall". In: *IEEE transactions on magnetics* 47.10 (2011), pp. 3501–3504.
- [59] E. G. Tveten et al. "Intrinsic magnetization of antiferromagnetic textures". In: *Physical Review B* 93.10 (2016), p. 104408.
- [60] O. V. Pylypovskyi et al. "Unidirectional tilt of domain walls in equilibrium in biaxial stripes with Dzyaloshinskii–Moriya interaction". In: *Journal of Physics D: Applied Physics* 53.39 (2020), p. 395003.
- [61] M. Heide, G Bihlmayer, and S. Blügel. "Dzyaloshinskii-Moriya interaction accounting for the orientation of magnetic domains in ultrathin films: Fe/W (110)". In: *Physical Review B* 78.14 (2008), p. 140403.
- [62] E. A. Turov et al. *Symmetry and physical properties of antiferromagnets*. Moscow: FIZMATLIT, 2001. 560 pp.
- [63] A. I. Akhiezer, V. G. Bar'yakhtar, and S. V. Peletminskii. *Spin waves*. Ed. by G. Höhler. Amsterdam: North-Holland, 1968.
- [64] Z. Chen et al. "Landau-Lifshitz-Bloch equation for domain wall motion in antiferromagnets". In: *Physical Review B* 99.21 (2019), p. 214436.
- [65] E. G. Tveten et al. "Intrinsic magnetization of antiferromagnetic textures". In: *Physical Review B* 93.10 (2016), p. 104408.
- [66] H. Yuan et al. "Classification of magnetic forces acting on an antiferromagnetic domain wall". In: *Physical Review B* 97.21 (2018), p. 214434.
- [67] M. Bode et al. "Chiral magnetic order at surfaces driven by inversion asymmetry". In: *Nature* 447.7141 (2007), pp. 190–193.
- [68] W. H. Meiklejohn and C. P. Bean. "New magnetic anisotropy". In: *Physical Review* 105.3 (1957), p. 904.
- [69] W. Roth. "Neutron and optical studies of domains in NiO". In: *Journal of Applied Physics* 31.11 (1960), pp. 2000–2011.
- [70] M. Fiebig et al. "Second Harmonic Generation and Magnetic-Dipole-Electric-Dipole Interference in Antiferromagnetic Cr<sub>2</sub>O<sub>3</sub>". In: *Phys. Rev. Lett.* 73 (15 1994), pp. 2127–2130.
- [71] M. Fiebig et al. "Domain topography of antiferromagnetic Cr<sub>2</sub>O<sub>3</sub> by second-harmonic generation". In: *Applied Physics Letters* 66.21 (1995), pp. 2906–2908.
- [72] M. Fiebig et al. "Observation of coupled magnetic and electric domains". In: *Nature* 419.6909 (2002), pp. 818–820.
- [73] M Bode et al. "Atomic spin structure of antiferromagnetic domain walls". In: *Nature materials* 5.6 (2006), pp. 477–481.
- [74] P. Schoenherr et al. "Magnetoelectric Force Microscopy on Antiferromagnetic 180 Domains in Cr<sub>2</sub>O<sub>3</sub>". In: *Materials* 10.9 (2017), p. 1051.
- [75] Y. Geng et al. "Direct visualization of magnetoelectric domains". In: *Nature materials* 13.2 (2014), pp. 163–167.
- [76] P. Appel et al. "Nanomagnetism of Magnetoelectric Granular Thin-Film Antiferromagnets". In: *Nano Letters* 19.3 (2019), pp. 1682–1687.
- [77] N. Hedrich et al. "Nanoscale mechanics of antiferromagnetic domain walls". In: *submitted* ().

- [78] I. Gross et al. "Real-space imaging of non-collinear antiferromagnetic order with a single-spin magnetometer". In: *Nature* 549.7671 (2017), pp. 252–256.
- [79] L. Lorenzelli. "Development of a Scanning Nitrogen-Vacancy Center Magnetometer for Variable Temperature Experiments". PhD thesis. ETH Zurich, 2021.
- [80] R. Johnson et al. "X-ray imaging and multiferroic coupling of cycloidal magnetic domains in ferroelectric monodomain BiFeO<sub>3</sub>". In: *Physical review letters* 110.21 (2013), p. 217206.
- [81] M. G. Kim et al. "Imaging antiferromagnetic antiphase domain boundaries using magnetic Bragg diffraction phase contrast". In: *Nature communications* 9.1 (2018), pp. 1–7.
- [82] W. Thomson. "XIX. On the electro-dynamic qualities of metals: Effects of magnetization on the electric conductivity of nickel and of iron". In: *Proceedings of the Royal Society of London* 8 (1857), pp. 546–550.
- [83] X. Marti et al. "Room-temperature antiferromagnetic memory resistor". In: *Nature materials* 13.4 (2014), pp. 367–374.
- [84] T. McGuire and R. Potter. "Anisotropic magnetoresistance in ferromagnetic 3d alloys". In: *IEEE Transactions on Magnetics* 11.4 (1975), pp. 1018–1038.
- [85] M. e. a. Wang. "Spin flop and crystalline anisotropic magnetoresistance in CuMnAs". In: *arXiv1911.12381* (2019).
- [86] K. Olejník et al. "Antiferromagnetic CuMnAs multi-level memory cell with microelectronic compatibility". In: *Nature Communications* 8 (2017), p. 15434. ISSN: 20411723.
- [87] J. Godinho et al. "Electrically induced and detected Néel vector reversal in a collinear antiferromagnet". In: *Nature Communications* 9 (2018), p. 4686. ISSN: 2041-1723. arXiv: [1806.02795](https://arxiv.org/abs/1806.02795).
- [88] A. Manchon and S. Zhang. "Theory of spin torque due to spin-orbit coupling". In: *Physical Review B* 79.9 (2009), p. 094422.
- [89] J. C. Slonczewski et al. "Current-driven excitation of magnetic multilayers". In: *Journal of Magnetism and Magnetic Materials* 159.1 (1996), p. L1.
- [90] L. Berger. "Emission of spin waves by a magnetic multilayer traversed by a current". In: *Physical Review B* 54.13 (1996), p. 9353.
- [91] A. Manchon et al. "Current-induced spin-orbit torques in ferromagnetic and antiferromagnetic systems". In: *Reviews of Modern Physics* 91 (2018), p. 035004. arXiv: [1801.09636](https://arxiv.org/abs/1801.09636).
- [92] A. Manchon and S. Zhang. "Theory of nonequilibrium intrinsic spin torque in a single nanomagnet". In: *Physical Review B* 78.21 (2008), p. 212405.
- [93] J. Železný et al. "Relativistic Néel-order fields induced by electrical current in antiferromagnets". In: *Physical review letters* 113.15 (2014), p. 157201.
- [94] S. Y. Bodnar et al. "Writing and reading antiferromagnetic Mn<sub>2</sub>Au by Néel spin-orbit torques and large anisotropic magnetoresistance". In: *Nature communications* 9.1 (2018), pp. 1–7.
- [95] I. Aharonovich et al. "Diamond-based single-photon emitters". In: *Reports on progress in Physics* 74.7 (2011), p. 076501.
- [96] R. Shirhagl et al. "Nitrogen-vacancy center in diamond: Nanoscale sensors for physics and biology". In: *Annu. Rev. Phys. Chem* 65 (2014), pp. 83–105.



- [97] A. Gruber et al. "Scanning confocal optical microscopy and magnetic resonance on single defect centers". In: *Science* 276.5321 (1997), pp. 2012–2014.
- [98] L. Childress et al. "Coherent dynamics of coupled electron and nuclear spin qubits in diamond". In: *Science* 314.5797 (2006), pp. 281–285.
- [99] A. S. Barnard. "Diamond standard in diagnostics: nanodiamond biolabels make their mark". In: *Analyst* 134.9 (2009), pp. 1751–1764.
- [100] F. Dolde et al. "Electric-field sensing using single diamond spins". In: *Nature Physics* 7.6 (2011), pp. 459–463.
- [101] M. W. Doherty et al. "The nitrogen-vacancy colour centre in diamond". In: *Physics Reports* 528.1 (2013), pp. 1–45.
- [102] L. Rondin et al. "Magnetometry with nitrogen-vacancy defects in diamond". In: *Reports on progress in physics* 77.5 (2014), p. 056503.
- [103] A. Dréau et al. "Avoiding power broadening in optically detected magnetic resonance of single NV defects for enhanced dc magnetic field sensitivity". In: *Phys. Rev. B* 84 (19 2011), p. 195204.
- [104] A. Gali, M. Fyta, and E. Kaxiras. "Ab initio supercell calculations on nitrogen-vacancy center in diamond: Electronic structure and hyperfine tensors". In: *Physical Review B* 77.15 (2008), p. 155206.
- [105] J. Zopes. "Three-dimensional localization spectroscopy of individual nuclear spins in diamond". PhD thesis. ETH Zurich, 2019.
- [106] F. Jelezko and J. Wrachtrup. "Single defect centres in diamond: A review". In: *physica status solidi (a)* 203.13 (2006), pp. 3207–3225.
- [107] E. Van Oort and M. Glasbeek. "Electric-field-induced modulation of spin echoes of NV centers in diamond". In: *Chemical Physics Letters* 168.6 (1990), pp. 529–532.
- [108] C. Degen. "Scanning magnetic field microscope with a diamond single-spin sensor". In: *Applied Physics Letters* 92.24 (2008), p. 243111.
- [109] G. Balasubramanian et al. "Nanoscale imaging magnetometry with diamond spins under ambient conditions". In: *Nature* 455.7213 (2008), pp. 648–651.
- [110] J. R. Maze et al. "Nanoscale magnetic sensing with an individual electronic spin in diamond". In: *Nature* 455.7213 (2008), pp. 644–647.
- [111] V. M. Acosta et al. "Temperature dependence of the nitrogen-vacancy magnetic resonance in diamond". In: *Physical review letters* 104.7 (2010), p. 070801.
- [112] D. M. Toyli et al. "Fluorescence thermometry enhanced by the quantum coherence of single spins in diamond". In: *Proceedings of the National Academy of Sciences* 110.21 (2013), pp. 8417–8421.
- [113] G. Kucsko et al. "Nanometre-scale thermometry in a living cell". In: *Nature* 500.7460 (2013), pp. 54–58.
- [114] M. W. Doherty et al. "Electronic properties and metrology applications of the diamond NV- center under pressure". In: *Physical review letters* 112.4 (2014), p. 047601.
- [115] S Felton et al. "Hyperfine interaction in the ground state of the negatively charged nitrogen vacancy center in diamond". In: *Physical Review B* 79.7 (2009), p. 075203.

- [116] C. P. Slichter. *Principles of magnetic resonance*. Vol. 1. Springer Science & Business Media, 2013.
- [117] C. L. Degen. Private Communication. 2020.
- [118] N. Vitanov et al. “Power broadening revisited: theory and experiment”. In: *Optics communications* 199.1-4 (2001), pp. 117–126.
- [119] “QZabre LLC, <https://qzabre.com>”. In: (retrieved on 2019-07-18) ().
- [120] N. V. Hauff. “Development of a Nanoscale Electron Spin Resonance Platform Based on a Diamond Chip”. MA thesis. Heidelberg University, 2018.
- [121] F. Casola, T. van der Sar, and A. Yacoby. “Probing condensed matter physics with magnetometry based on nitrogen-vacancy centres in diamond”. In: *Nature Reviews Materials* 3.1 (2018), pp. 1–13.
- [122] A. Zvezdin. *Modern magneto-optics and magneto-optical materials*.
- [123] I. A. Beardsley. “Reconstruction of the magnetization in a thin film by a combination of Lorentz microscopy and external field measurements”. In: *IEEE Transactions on Magnetics* 25 (1989), p. 671.
- [124] I. Beardsley. “Reconstruction of the magnetization in a thin film by a combination of Lorentz microscopy and external field measurements”. In: *IEEE transactions on magnetics* 25.1 (1989), pp. 671–677.
- [125] N. A. Spaldin. “Analogy between the magnetic dipole moment at the surface of a magnetoelectric and the electric charge at the surface of a ferroelectric”. In: *arXiv preprint arXiv:2011.14351* (2020).
- [126] A. Brataas, A. D. Kent, and H. Ohno. “Current-induced torques in magnetic materials”. In: *Nature materials* 11.5 (2012), pp. 372–381.
- [127] K. Garello et al. “Symmetry and magnitude of spin-orbit torques in ferromagnetic heterostructures”. In: *Nature nanotechnology* 8.8 (2013), pp. 587–593.
- [128] I. M. Miron et al. “Fast current-induced domain-wall motion controlled by the Rashba effect”. In: *Nature materials* 10.6 (2011), pp. 419–423.
- [129] M. Baumgartner et al. “Spatially and time-resolved magnetization dynamics driven by spin-orbit torques”. In: *Nature nanotechnology* 12.10 (2017), p. 980.
- [130] I. M. Miron et al. “Perpendicular switching of a single ferromagnetic layer induced by in-plane current injection”. In: *Nature* 476.7359 (2011), pp. 189–193.
- [131] A. Thiaville et al. “Dynamics of Dzyaloshinskii domain walls in ultrathin magnetic films”. In: *EPL (Europhysics Letters)* 100.5 (2012), p. 57002.
- [132] S. Emori et al. “Current-driven dynamics of chiral ferromagnetic domain walls”. In: *Nature materials* 12.7 (2013), pp. 611–616.
- [133] J. Torrejon, E. Martinez, and M. Hayashi. “Tunable inertia of chiral magnetic domain walls”. In: *Nature communications* 7.1 (2016), pp. 1–7.
- [134] Y. Kajiwara et al. “Transmission of electrical signals by spin-wave interconversion in a magnetic insulator”. In: *Nature* 464.7286 (2010), pp. 262–266.
- [135] L. Cornelissen et al. “Long-distance transport of magnon spin information in a magnetic insulator at room temperature”. In: *Nature Physics* 11.12 (2015), pp. 1022–1026.
- [136] S. T. Goennenwein et al. “Non-local magnetoresistance in YIG/Pt nanostructures”. In: *Applied Physics Letters* 107.17 (2015), p. 172405.

- [137] M. Collet et al. "Generation of coherent spin-wave modes in yttrium iron garnet microdiscs by spin-orbit torque". In: *Nature communications* 7.1 (2016), pp. 1–8.
- [138] C. O. Avci et al. "Current-induced switching in a magnetic insulator". In: *Nature materials* 16.3 (2017), pp. 309–314.
- [139] C. O. Avci et al. "Fast switching and signature of efficient domain wall motion driven by spin-orbit torques in a perpendicular anisotropy magnetic insulator/Pt bilayer". In: *Applied Physics Letters* 111.7 (2017), p. 072406.
- [140] Q. Shao et al. "Role of dimensional crossover on spin-orbit torque efficiency in magnetic insulator thin films". In: *Nature communications* 9.1 (2018), pp. 1–7.
- [141] A. Malozemoff and J. Slonczewski. *Magnetic Domain Walls in Bubble Materials: Advances in Materials and Device Research*. Vol. 1. Academic press, 2016.
- [142] A. Paoletti et al. *Physics of Magnetic Garnets: Proceedings of the International School of Physics 'Enrico Fermi', Course LXX, Varenna on Lake Como, Villa Monastero, 27th June-9th July 1977*. Elsevier Science & Technology, 1978.
- [143] V. Bokov et al. "Relation between relaxation losses in domain-wall motion and ferromagnetic resonance in garnet films". In: *Physics of the Solid State* 40.8 (1998), pp. 1377–1382.
- [144] L. Caretta et al. "Fast current-driven domain walls and small skyrmions in a compensated ferrimagnet". In: *Nature nanotechnology* 13.12 (2018), pp. 1154–1160.
- [145] S.-H. Yang, K.-S. Ryu, and S. Parkin. "Domain-wall velocities of up to 750 m s<sup>-1</sup> driven by exchange-coupling torque in synthetic antiferromagnets". In: *Nature nanotechnology* 10.3 (2015), pp. 221–226.
- [146] K.-S. Ryu et al. "Chiral spin torque at magnetic domain walls". In: *Nature nanotechnology* 8.7 (2013), pp. 527–533.
- [147] S. A. Siddiqui et al. "Current-induced domain wall motion in a compensated ferrimagnet". In: *Physical review letters* 121.5 (2018), p. 057701.
- [148] A. Manchon et al. "Current-induced spin-orbit torques in ferromagnetic and antiferromagnetic systems". In: *Reviews of Modern Physics* 91.3 (2019), p. 035004.
- [149] S.-G. Je et al. "Asymmetric magnetic domain-wall motion by the Dzyaloshinskii-Moriya interaction". In: *Physical Review B* 88.21 (2013), p. 214401.
- [150] I. Gross et al. "Direct measurement of interfacial Dzyaloshinskii-Moriya interaction in X|CoFeB|MgO heterostructures with a scanning NV magnetometer (X= Ta, TaN, and W)". In: *Physical Review B* 94.6 (2016), p. 064413.
- [151] O. Shpyrko et al. "Direct measurement of antiferromagnetic domain fluctuations". In: *Nature* 447.7140 (2007), pp. 68–71.
- [152] F. Radu and H. Zabel. "Exchange bias effect of ferro-/antiferromagnetic heterostructures". In: *Magnetic heterostructures*. Springer, 2008, pp. 97–184.
- [153] R. Jaramillo et al. "Microscopic and Macroscopic Signatures of Antiferromagnetic Domain Walls". In: *Phys. Rev. Lett.* 98 (11 2007), p. 117206.
- [154] K. M. D. Hals, Y. Tserkovnyak, and A. Brataas. "Phenomenology of Current-Induced Dynamics in Antiferromagnets". In: *Phys. Rev. Lett.* 106 (10 2011), p. 107206.

- [155] O. Gomonay, T. Jungwirth, and J. Sinova. "High Antiferromagnetic Domain Wall Velocity Induced by Néel Spin-Orbit Torques". In: *Phys. Rev. Lett.* 117 (1 2016), p. 017202.
- [156] L. Baldrati et al. "Mechanism of Néel Order Switching in Antiferromagnetic Thin Films Revealed by Magnetotransport and Direct Imaging". In: *Phys. Rev. Lett.* 123 (17 2019), p. 177201.
- [157] T. Jungwirth et al. "Antiferromagnetic spintronics". In: *Nature Nanotechnology* 11.3 (2016), pp. 231–241.
- [158] V. Baltz et al. "Antiferromagnetic spintronics". In: *Rev. Mod. Phys.* 90 (1 2018), p. 015005.
- [159] A. Hubert and R. Schäfer. *Magnetic Domains: The Analysis of Magnetic Microstructures*. Springer Berlin Heidelberg, 2008. ISBN: 9783540850540.
- [160] O. Hellwig, A. Berger, and E. E. Fullerton. "Domain walls in antiferromagnetically coupled multilayer films". In: *Phys. Rev. Lett.* 91 (2003), p. 197203.
- [161] Z. Chen et al. "Landau-Lifshitz-Bloch equation for domain wall motion in antiferromagnets". In: *Physical Review B* 99.21 (2019), p. 214436.
- [162] T. Kosub et al. "Purely antiferromagnetic magnetoelectric random access memory". In: *Nature Communications* 8.1 (2017), pp. 1–7.
- [163] M. Fiebig, D. Fröhlich, and H. J. Thiele. "Determination of spin direction in the spin-flop phase of  $\text{Cr}_2\text{O}_3$ ". In: *Phys. Rev. B* 54 (18 1996), R12681–R12684.
- [164] G. T. Rado and V. J. Folen. "Magnetoelectric Effects in Antiferromagnetics". In: *Proceedings of the Seventh Conference on Magnetism and Magnetic Materials*. Ed. by J. A. Osborn. Boston, MA: Springer US, 1962, pp. 1126–1132. ISBN: 978-1-4899-6391-8.
- [165] B. N. Brockhouse. "Antiferromagnetic structure in  $\text{Cr}_2\text{O}_3$ ". In: *The Journal of Chemical Physics* 21.5 (1953), pp. 961–962.
- [166] D. Astrov. "Magnetoelectric effect in chromium oxide". In: *Sov. Phys. JETP* 13.4 (1961), pp. 729–733.
- [167] T. Martin and J. Anderson. "Antiferromagnetic domain switching in  $\text{Cr}_2\text{O}_3$ ". In: *IEEE Transactions on Magnetics* 2.3 (1966), pp. 446–449.
- [168] M. Mostovoy et al. "Temperature-Dependent Magnetoelectric Effect from First Principles". In: *Phys. Rev. Lett.* 105 (8 2010), p. 087202.
- [169] P. Borisov et al. "Magnetoelectric switching of exchange bias". In: *Physical Review Letters* 94.11 (2005), p. 117203.
- [170] X. He et al. "Robust isothermal electric control of exchange bias at room temperature". In: *Nature Materials* 9.7 (2010), 579–585.
- [171] Z. Qiu et al. "Spin colossal magnetoresistance in an antiferromagnetic insulator". In: *Nature materials* 17.7 (2018), pp. 577–580.
- [172] J. Li et al. "Spin current from sub-terahertz-generated antiferromagnetic magnons". In: *Nature* 578.7793 (2020), pp. 70–74.
- [173] Y. Kota and H. Imamura. "Narrowing of antiferromagnetic domain wall in corundum-type  $\text{Cr}_2\text{O}_3$  by lattice strain". In: *Applied Physics Express* 10.1 (2016), p. 013002.
- [174] R. V. Pisarev, M. Fiebig, and D. Fröhlich. "Nonlinear optical spectroscopy of magnetoelectric and piezomagnetic crystals". In: *Ferroelectrics* 204 (1997), pp. 1–21.

- [175] B. B. Krichevtsov, V. V. Pavlov, and R. V. Pisarev. "Nonreciprocal optical effects in antiferromagnetic  $\text{Cr}_2\text{O}_3$  subjected to electric and magnetic fields". In: *Sov. Phys. JETP* 67 (1988), p. 378.
- [176] D. N. Astrov et al. "External quadrupole magnetic field of antiferromagnetic  $\text{Cr}_2\text{O}_3$ ". In: *Journal of Experimental and Theoretical Physics Letters* 63.9 (1996), pp. 745–751. ISSN: 1090-6487.
- [177] S. Mu and K. D. Belashchenko. "Influence of strain and chemical substitution on the magnetic anisotropy of antiferromagnetic  $\text{Cr}_2\text{O}_3$ : An ab-initio study". In: *Phys. Rev. Materials* 3 (3 2019), p. 034405.
- [178] P. Wadley et al. "Electrical switching of an antiferromagnet". In: *Science* 351.6273 (2016), pp. 587–590. ISSN: 10959203. arXiv: [1503.03765](https://arxiv.org/abs/1503.03765).
- [179] S. Y. Bodnar et al. "Writing and reading antiferromagnetic  $\text{Mn}_2\text{Au}$  by Néel spin-orbit torques and large anisotropic magnetoresistance". In: *Nature Communications* 9.1 (2018), p. 348. ISSN: 2041-1723. arXiv: [1706.02482](https://arxiv.org/abs/1706.02482).
- [180] J. Železný et al. "Relativistic Néel-order fields induced by electrical current in antiferromagnets". In: *Physical Review Letters* 113.15 (2014), p. 157201. ISSN: 10797114. arXiv: [1410.8296](https://arxiv.org/abs/1410.8296).
- [181] M. J. Grzybowski et al. "Imaging Current-Induced Switching of Antiferromagnetic Domains in  $\text{CuMnAs}$ ". In: *Physical Review Letters* 118.5 (2017), p. 057701. ISSN: 10797114. arXiv: [1607.08478](https://arxiv.org/abs/1607.08478).
- [182] P. Wadley et al. "Current polarity-dependent manipulation of antiferromagnetic domains". In: *Nature Nanotechnology* 13.5 (2018), pp. 362–365. ISSN: 1748-3387. eprint: [arXiv:1711.05146](https://arxiv.org/abs/1711.05146).
- [183] S. Y. Bodnar et al. "Imaging of current induced Néel vector switching in antiferromagnetic  $\text{Mn}_2\text{Au}$ ". In: *Phys. Rev. B* 99 (2019), p. 140409.
- [184] K. Olejník et al. "Terahertz electrical writing speed in an antiferromagnetic memory". In: *Science Advances* 4.3 (2018), eaar3566. ISSN: 2375-2548. arXiv: [1711.08444](https://arxiv.org/abs/1711.08444).
- [185] P. Wadley et al. "Antiferromagnetic structure in tetragonal  $\text{CuMnAs}$  thin films". In: *Scientific Reports* 5 (2015), p. 17079. ISSN: 20452322.
- [186] P. Isola et al. "Image-to-image translation with conditional adversarial networks". In: *Proceedings of the IEEE conference on computer vision and pattern recognition*. 2017, pp. 1125–1134.
- [187] F. Krizek et al. "Atomically sharp domain walls in an antiferromagnet". In: *arXiv preprint arXiv:2012.00894* (2020).
- [188] J. H. Franken et al. "Tunable resistivity of individual magnetic domain walls". In: *Physical review letters* 108.3 (2012), p. 037205.
- [189] M Viret et al. "Anisotropy of domain wall resistance". In: *Physical review letters* 85.18 (2000), p. 3962.
- [190] R Jaramillo et al. "Microscopic and macroscopic signatures of antiferromagnetic domain walls". In: *Physical review letters* 98.11 (2007), p. 117206.
- [191] L. Berger. "Lowfield magnetoresistance and domain drag in ferromagnets". In: *Journal of Applied Physics* 49.3 (1978), pp. 2156–2161. ISSN: 0021-8979. arXiv: [arXiv:1011.1669v3](https://arxiv.org/abs/1011.1669v3).
- [192] P. M. Levy and S. Zhang. "Resistivity due to domain wall scattering". In: *Physical Review Letters* 79.25 (1997), pp. 5110–5113. ISSN: 10797114.

- [193] H. Tang and M. L. Roukes. "Electrical transport across an individual magnetic domain wall in (Ga,Mn)As microdevices". In: *Physical Review B - Condensed Matter and Materials Physics* 70.20 (2004), p. 205213. ISSN: 01631829.
- [194] P. R. Letters et al. "Giant Magnetoresistive Effects in a Single Element Magnetic Thin Film". In: *Physical Review Letters* 77.8 (1996), pp. 1580–1583.
- [195] R. K. Kummamuru and Y.-A. Soh. "Electrical effects of spin density wave quantization and magnetic domain walls in chromium". In: *Nature* 452.7189 (2008), pp. 859–863. ISSN: 0028-0836.
- [196] F. Krizek et al. "Molecular beam epitaxy of CuMnAs". In: *Physical Review Materials* 4.1 (2020), p. 014409.
- [197] N. Xu et al. "Wavelet-based fast time-resolved magnetic sensing with electronic spins in diamond". In: *Physical Review B* 93.16 (2016), p. 161117.
- [198] A. Cooper et al. "Time-resolved magnetic sensing with electronic spins in diamond". In: *Nature communications* 5.1 (2014), pp. 1–7.
- [199] E. Magesan et al. "Reconstructing the profile of time-varying magnetic fields with quantum sensors". In: *Physical Review A* 88.3 (2013), p. 032107.
- [200] O. Gomonay, T. Jungwirth, and J. Sinova. "High antiferromagnetic domain wall velocity induced by Néel spin-orbit torques". In: *Physical review letters* 117.1 (2016), p. 017202.
- [201] P. Roy, R. Otxoa, and J Wunderlich. "Robust picosecond writing of a layered antiferromagnet by staggered spin-orbit fields". In: *Physical Review B* 94.1 (2016), p. 014439.
- [202] T. Shiino et al. "Antiferromagnetic domain wall motion driven by spin-orbit torques". In: *Physical review letters* 117.8 (2016), p. 087203.
- [203] E. Maniv et al. "Antiferromagnetic Switching Driven by the Collective Dynamics of a Coexisting Spin Glass". In: *arXiv preprint arXiv:2008.02795* (2020).
- [204] B. J. Roth, N. G. Sepulveda, and J. P. Wikswo Jr. "Using a magnetometer to image a two-dimensional current distribution". In: *Journal of applied physics* 65.1 (1989), pp. 361–372.
- [205] A. Dreau et al. "Avoiding power broadening in optically detected magnetic resonance of single NV defects for enhanced dc magnetic field sensitivity". In: *Phys. Rev. B* 84 (2011), p. 195204.
- [206] R. Schirhagl et al. "Nitrogen-vacancy centers in diamond: Nanoscale sensors for physics and biology". In: *Annu. Rev. Phys. Chem.* 65 (2014), p. 83.
- [207] K. D. Belashchenko. "Equilibrium Magnetization at the Boundary of a Magnetoelectric Antiferromagnet". In: *Phys. Rev. Lett.* 105 (14 2010), p. 147204.
- [208] A. Andreev. "Macroscopic magnetic fields of antiferromagnets". In: *Journal of Experimental and Theoretical Physics Letters* 63.9 (1996), pp. 758–762.
- [209] O. Madelung, U. Rössler, and M. S. (ed.) "Chromium sesquioxide (Cr<sub>2</sub>O<sub>3</sub>): magnetic properties". In: *In: Non-Tetrahedrally Bonded Binary Compounds II (Springer, Berlin-Heidelberg, 2000)* ().
- [210] B. Efron and C. Stein. "The jackknife estimate of variance". In: *The Annals of Statistics* (1981), pp. 586–596.
- [211] P. Wadley et al. "Tetragonal phase of epitaxial room-temperature antiferromagnet CuMnAs". In: *Nature Communications* 4 (2013), p. 2322. ISSN: 20411723. arXiv: 1402.3624.

- [212] P. Wadley. Private Communication. 2020.
- [213] C.-Y. You, I. M. Sung, and B.-K. Joe. "Analytic expression for the temperature of the current-heated nanowire for the current-induced domain wall motion". In: *Applied physics letters* 89.22 (2006), p. 222513.

# List of Figures

1.1	Ferromagnetic and antiferromagnetic spintronics. . . . .	2
1.2	Schematic of the nanoscale scanning diamond magnetometer. . . . .	3
2.1	Magnetic ground states and order parameter. . . . .	10
2.2	One-dimensional model for an antiferromagnetic $180^\circ$ domain wall. . . . .	12
2.3	DMI leading to a preference of Néel-type domain walls. . . . .	14
2.4	Various imaging methods of AFM domains. . . . .	15
2.5	Manipulating and probing the Néel vector in CuMnAs. . . . .	17
3.1	Properties of the NV centre . . . . .	21
3.2	Sensing protocols, showing pulse-timing diagrams (Top) and example measurements (bottom) . . . . .	23
3.3	Optimising the magnetic sensitivity for CW ODMR. . . . .	26
3.4	Optimising the magnetic sensitivity for pulsed ODMR. . . . .	27
3.5	Angular dependence of the NV ground energy levels on the magnetic field. . . . .	29
4.1	Key modules of the NSDM instrument. . . . .	32
4.2	Microscope head and sensor. . . . .	33
4.3	Optics module . . . . .	34
4.4	Magneto-optical Kerr microscopy module. . . . .	36
4.5	Readout and control electronics. . . . .	37
5.1	Effective surface magnetisation in AFMs. . . . .	41
5.2	Reconstruction of $M_z$ . . . . .	44
6.1	Device schematic of TmIG . . . . .	51
6.2	Domain wall structure and chirality in TmIG and TmIG/Pt measured by NSDM . . . . .	52
6.3	Spatially-resolved MOKE- dependence of $v_{DW}$ . . . . .	54
6.4	Schematics of the domain wall structure and current-induced domain wall motion in the presence of $H_x$ and DMI. . . . .	55
6.5	SQUID magnetometry of the TmIG samples. . . . .	56
7.1	$\text{Cr}_2\text{O}_3$ crystal structure and experimental arrangement. . . . .	61
7.2	Antiferromagnetic domain pattern in $c$ -oriented $\text{Cr}_2\text{O}_3$ . . . . .	63
7.3	Quantitative measurement of domain-wall structure and surface magnetisation. . . . .	64
7.4	Observation of Bloch and Néel walls. . . . .	66
8.1	Nanoscale scanning diamond magnetometry of CuMnAs. . . . .	71



8.2	Current distribution, electrical resistance, and magnetic stray field maps of the relaxed state after switching. . . . .	73
8.3	Repeated excitation measurements and stray field maps of the excited and relaxed states. . . . .	75
8.4	Simulations of the stray field produced by a pristine and a fragmented domain pattern. . . . .	76
8.5	Correlation between fragmentation and electrical resistance. . . . .	78
8.6	Domain wall resistance, domain wall density and electrical model. . . . .	79
A.1	Calibration of the sample-to-sensor distance $z$ . . . . .	88
B.1	In situ calibration of the NV sample-to-sensor distance on TmIG/Pt . . . . .	90
B.2	Domain wall structure and surface magnetisation in the reference sample TmIG . . . . .	92
C.1	SHG microscopy images of sample A (left panels) and sample B (right panels). . . . .	97
C.2	SHG microscopy images of sample C. . . . .	98
C.3	Maximum likelihood estimates for domain wall width $\Delta_{\text{DW}}$ and twist angle $\chi$ . . . . .	98
C.4	Maximum likelihood estimates for domain wall width $\Delta_{\text{DW}}$ and twist angle $\chi$ for upper and lower bound stand-off distances . . . . .	99
D.1	Error variance for reconstruction of domain pattern in Fig. 8.1d. . . . .	103
D.2	Magnetic field of on CuMnAs ( $t = 30$ nm) showing ferromagnetic patches. . . . .	103
D.3	Reconstruction of the domain pattern using image to image translation. . . . .	105
D.4	Current induced fragmentation in the magnetic texture. . . . .	106
D.5	Non-uniform fragmentation and polarity switching. . . . .	107
D.6	Model of the CuMnAs surface steps. . . . .	108
D.7	Analysis of the temperature evolution in the cross-device during a typical writing pulse. . . . .	110

# List of Tables

3.1 Properties of a typical NV centre. Coupling coefficients and typical sensitivities. . . . .	22
---	----



# Curriculum Vitae

---

## Personal Details

Name: Martin Sebastian Wörnle

Date of birth: March 10<sup>th</sup> 1991

Nationality: German

---

## Education

- 02/2017–03/2021 DOCTOR OF SCIENCES ETH ZÜRICH  
Doctoral thesis: *“Nanoscale Scanning Diamond Magnetometry of Antiferromagnets”*  
Chair for Magnetism and Interface Physics, ETH Zürich  
Supervisor: Prof. Dr. Pietro Gambardella  
Chair for Spin Physics, ETH Zürich  
Supervisor: Prof. Dr. Christian L. Degen
- 08/2016–09/2016 Internship/Scholarship at Åkerman Group (Spintronics), Göteborgs Universitet
- 01/2014–06/2016 MASTER OF SCIENCE, PHYSICS, UNIVERSITÄT REGENSBURG  
Master thesis: *“Current induced switching of perpendicularly magnetized HM/FM-bilayers”*
- 08/2013–01/2014 Master of Science, Physics, Université Montpellier (Exchange Semester)
- 05/2011–07/2013 BACHELOR OF SCIENCE, PHYSICS, UNIVERSITÄT REGENSBURG  
Bachelor thesis: *“Spin Hall effect in Tungsten”*
- 09/2002–04/2011 Chiemgau Gymnasium Traunstein, Deutschland

---

## Working Experience

- 11/2016–02/2017 Internship Horváth & Partners (Consultancy/Big Data Business Analytics)
- 01/2014–06/2016 Department of Physics, Universität Regensburg  
Tutoring and supervision: Physics, Computer courses
- 

## Conferences & Workshops

- [1] Poster presentation. *QSIT - Quantum Science and Technology, General Meeting*. Arosa, Switzerland, (2020).
- [2] Invited talk. *Materials Research Society Fall Meeting (MRS)*. Boston, USA, (2019).
- [3] Invited talk. *SPICE-Workshop Antiferromagnetic Spintronics: from topology to neuromorphic computing*. Mainz, Germany, (2019).
- [4] Invited talk. *Informal meeting on antiferromagnetic memory devices*. Prag, Czech Republic, (2019).
- [5] Poster presentation. *CCMX-NCCR MARVEL Materials Science Day*. Bern, Switzerland, (2018).
- [6] Invited talk. *Workshop on domain imaging in antiferromagnets*. Prag, Czech Republic, (2018).
- [7] Poster presentation. *QSIT - Quantum Science and Technology, General Meeting*. Arosa, Switzerland, (2018).
- [8] Poster presentation. *European School on Magnetism, Summer School*. Cargèse, France, (2017).
- [9] Contributed talk. *QSIT - Quantum Science and Technology, Junior Meeting*. Passugg, Switzerland, (2017).

---

**Journal articles**

- [1] M. S. Wörnle, P. Welter, M. Giraldo, T. Lottermoser, M. Fiebig, P. Gambardella, and C. L. Degen, "Coexistence of bloch and néel walls in a collinear antiferromagnet," *Phys. Rev. B*, vol. 103, p. 094426, Mar 2021.
- [2] Z. Kašpar, M. Surýnek, J. Zubáč, F. Krizek, V. Novák, R. Campion, M. Wörnle, P. Gambardella, X. Marti, P. Němec, *et al.*, "Quenching of an antiferromagnet into high resistivity states using electrical or ultrashort optical pulses," *Nature Electronics*, pp. 1–8, 2020.
- [3] C. Stamm, C. Murer, M. Wörnle, Y. Acremann, R. Gort, S. Däster, A. Reid, D. Higley, S. Wandel, W. Schlotter, *et al.*, "X-ray detection of ultrashort spin current pulses in synthetic antiferromagnets," *Journal of Applied Physics*, vol. 127, no. 22, p. 223902, 2020.
- [4] M. Wörnle, P. Welter, Z. Kašpar, K. Olejník, V. Novák, R. Campion, P. Wadley, T. Jungwirth, C. Degen, and P. Gambardella, "Current-induced fragmentation of antiferromagnetic domains," *arXiv preprint arXiv:1912.05287*, 2019.
- [5] S. Vélez, J. Schaab, M. S. Wörnle, M. Müller, E. Gradauskaite, P. Welter, C. Gutgsell, C. Nistor, C. L. Degen, M. Trassin, *et al.*, "High-speed domain wall racetracks in a magnetic insulator," *Nature communications*, vol. 10, no. 1, pp. 1–8, 2019.
- [6] M. M. Decker, M. S. Wörnle, A. Meisinger, M. Vogel, H. Körner, G. Shi, C. Song, M. Kronseder, and C. H. Back, "Time resolved measurements of the switching trajectory of pt/co elements induced by spin-orbit torques," *Physical review letters*, vol. 118, no. 25, p. 257201, 2017.